# Attosecond Timing Jitter Modelocked Lasers and Ultralow Phase Noise Photonic Microwave Oscillators

ARCHIVES
MASSACHUSETTS INSTITUTE
OF TECHNOLOGY
APR 10 2014
LIBRARIES

by

Duo Li

B.S., Information Engineering, Zhejiang University, 2005
M.S., Optical Engineering, Tsinghua University, 2008

Submitted to the Department of Electrical Engineering and Computer Science
in partial fulfillment of the requirements for the degree of

Doctor of Philosophy in Electrical Engineering and Computer Science

at the

MASSACHUSETTS INSTITUTE OF TECHNOLOGY

February 2014

© 2014 Massachusetts Institute of Technology. All rights reserved.

Author.........................................................................................................................
Department of Electrical Engineering and Computer Science
January 30th, 2014

Certified by...................................................................................................................
Franz X. Kärtner
Professor of Electrical Engineering
Thesis Supervisor

Certified by...................................................................................................................
Erich P. Ippen
Elihu Thomson Professor of Electrical Engineering, Professor of Physics
Thesis Supervisor

Accepted by...................................................................................................................
Leslie A. Kolodziejski
Professor of Electrical Engineering
Chair, Department Committee on Graduate Theses

THIS PAGE INTENTIONALLY LEFT BLANK

# Attosecond Timing Jitter of Modelocked Lasers and Ultralow Phase Noise Photonic Microwave Oscillators

by

Duo Li

Submitted to the Department of Electrical Engineering and Computer Science
on January 30th, 2014 in partial fulfillment of the
requirements for the degree of
Doctor of Philosophy in Electrical Engineering and Computer Science

## Abstract

Photonic microwave oscillator based on optical frequency comb and ultrastable optical reference cavity represents the state-of-the-art solution to generate X-band microwaves of ultralow phase noise. Such high-quality microwave source enables a range of applications in which frequency stability and timing accuracy are essential to performance. Wide use of this technology, however, requires compact system architecture, low-term stability and low energy consumption, which drive the needs to develop high repetition-rate femtosecond lasers alternative to Ti:sapphire technology, and to explore a feasible means to achieve integrated photonic microwave oscillators.

Ultrafast Cr:LiSAF lasers can be directly pumped with low-cost red laser diodes, and the electrical-to-optical conversion efficiency is as high as 10%. High repetition-rate femtosecond Cr:LiSAF lasers are developed with the help of semiconductor saturable absorber technology, efficient dispersion compensation mirror design algorithms, and heat management of the saturable absorber. The 1-GHz Cr:LiSAF oscillator generates 55-fs pulses with 110 pJ pulse energy, which represents almost two orders of magnitude improvement in the output peak power over previous results. Timing jitter of 100-MHz Cr:LiSAF lasers is measured with a single-crystal balanced optical cross-correlator to be ~30 as from 10 kHz to 50 MHz. Pump intensity noise coupled into phase noise through the self-steepening effect proves to be the major noise source.

The most recent advance in silicon photonics and wafer-scale three-dimensional integration technology illuminates a pathway toward on-chip photonic microwave oscillators. Phase noise model of the proposed Erbium Silicon Photonics Integrated OscillatoR (ESPIOR) suggests that it is possible to achieve comparable noise performance with the Ti:sapphire-based system, without the need of carrier-envelope-offset frequency detection. A demonstration using fiber-optic components further indicates that it is practicable to realize optical frequency division and microwave readout in the proposed architecture. With the advancement of heterogeneous electronic-photonic integration, it would pave the way for an ultralow-noise microwave source fully integrated in a hybrid photonic-electronic chip on a silicon substrate.

Thesis Supervisor: Franz X. Kärtner
Title: Professor of Electrical Engineering

Thesis Supervisor: Erich P. Ippen
Title: Elihu Thomson Professor of Electrical Engineering, Professor of Physics

## Acknowledgements

I am honored to have been given the opportunity to conduct my Ph.D. work in the Optics and Quantum Electronics Group at the Massachusetts Institute of Technology. I would like to especially thank Prof. Franz Kärtner for his guidance, patience and support over the years. In writing this thesis, I constantly feel the pivotal role his ideas and encouragement play in directing my training and research toward the fields of the most potential and the broadest impact. I also thank Prof. Erich Ippen for his help and wisdom. Being in the audience of my first public presentation, and serving on my Research Qualifying Examination committee and doctoral thesis committee, Prof. Ippen has witnessed and supported every milestone of my studies in the Department of Electrical Engineering and Computer Science.

I am very lucky and grateful to have Prof. Qing Hu and Prof. Michael Watts on my thesis committee. Having been the teaching assistant to 6.013&6.630, I had many chances to work with and learn from them, as well as Prof. Ippen, to organize and develop course materials. I wanted to thank Prof. Hu for his suggestions on the thesis, and the graduate courses on solid-state physics that I find quite inspiring and practical. Prof. Watts offers me the great opportunity to work in the Electronic-Photonic Heterogeneous Integration (EPHI) project. Without his support and advisory, I could not have done an important part of the thesis work. In addition to research, Prof. Watts is also my academic advisor. I also wanted to thank Prof. Ronald Parker, my former academic advisor, for his guidance through my first few years in the Ph.D. program.

I started the journey of learning ultrafast optics under the supervision of Prof. James Fujimoto in 2008. I sincerely thank him for the support and training. In addition to research and courses, I find his lectures on Ph.D. requirements, mission statement, and the cost of graduate education and running a research group very helpful and important. Moreover, Prof. Alphan Sennaroğlu has offered help and discussion on the work of femtosecond lasers during his visiting to the group. Prof. Leslie Kolodziejski and Dr. Gale Petrich have provided various types of semiconductor saturable absorber samples. I feel honored to have been able to co-author papers with them.

In the past years, I have had the privilege of working with many people in a number of projects and courses, many of which cannot be included in this thesis but constitute an integral part of my training. As grateful as I am to every colleague and friend, I have to refrain myself from listing all of their names and contributions, because retrospection makes me miss the days working and studying with them. That being said, I still wanted to express my appreciation to Dr. Ümit Demirbaş, Dr. Andrew Benedick, Dr. Guoqing Chang, Dr. Michelle Sander, Jing Wang, Hung-Wen Chen, Michael Peng, and Dr. Jinkang Lim, who have offered great help and done much lab work with me.

I thank the funding agencies that have supported my research and living. They include DARPA, NSF, AFOSR, NIH, Thorlabs, the Department of Electrical Engineering and Computer Science, and the China Scholarship Council (CSC).

Last but not the least, I would like to thank Prof. Shulian Zhang, my former advisor at Tsinghua University, for the training and support I have received before coming to the US. I thank my parents and my wife, though words cannot express my gratitude.

## Table of Contents

**Chapter 1 Introduction** ........ **15**

1.1 Low-Noise Microwave Oscillators and Applications ........ 15

1.2 Diode Pumped Femtosecond Cr:Colquiriite Lasers ........ 18

1.3 Optical Frequency Division ........ 19

1.4 Thesis Outline ........ 20

**Chapter 2 High Repetition-Rate Cr:LiSAF Femtosecond Lasers** ........ **23**

2.1 Motivation ........ 23

2.2 Laser Design ........ 25

2.2.1 Laser Diode Pump Unit ........ 25

2.2.2 Laser Cavity Design ........ 30

2.3 Continuous-Wave and Modelocked Lasing Results ........ 33

**Chapter 3 Timing Jitter of Saturable Absorber Modelocked Cr:LiSAF Lasers41**

3.1 Motivation ........ 41

3.2 Quantum-Limited Timing Jitter ........ 42

3.3 Attosecond Timing Jitter Characterization ........ 46

3.3.1 Single-Crystal Balanced Optical Cross-Correlation ........ 46

3.3.2 Phase Noise Measurement ........ 49

3.4 Intensity Noise and Timing Jitter ........ 53

    3.4.1 AM-to-PM Conversion ........ 54
    3.4.2 Relative Intensity Noise ........ 58
    3.4.3 Saturable Absorber and Timing Jitter ........ 61

**Chapter 4 Phase Noise of Erbium Silicon Photonic Integrated Oscillators ........ 69**

  4.1 Motivation ........ 69
  4.2 Erbium Silicon Photonic Integrated Oscillator ........ 72
  4.3 Phase Noise of the Integrated Oscillator ........ 76
    4.3.1 Noise Model in Phase Domain ........ 76
    4.3.2 Stable Continuous-Wave Laser ........ 76
    4.3.3 Optical Frequency Division ........ 82
    4.3.4 Microwave Readout ........ 89
  4.4 Fiber-Optic Demonstration ........ 90
    4.4.1 Stable Continuous-Wave Laser ........ 91
    4.4.2 Optical Frequency Division ........ 92
    4.4.3 Microwave Readout ........ 94

**Chapter 5 Conclusion and Future Work ........ 99**

  5.1 Femtosecond Cr:LiSAF Lasers ........ 99
  5.2 Photonic Microwave Oscillators ........ 100

**Appendix A Balanced Cross-Correlation of $\mathrm{sech}^2$-Shaped Laser Pulses ........ 103**

**Appendix B Schawlow-Townes Linewidth of Single-Frequency Laser ........ 107**

**Appendix C** Phase Locked Loop Analysis Using MATLAB Toolboxes .............. 109

**Bibliography** ..........................................................................................111

## List of Figures

Figure 1.1. Phase noise of three types of microwave oscillators. OFC, optical frequency comb; SLCO, sapphire loaded cavity oscillator; PN, phase noise ........ 16

Figure 2.1. Collimated beam profile of the HL6385DG laser diode. Above, beam cross sections as a function of the distance from the collimating lens. Below, beam radii in x and y directions. ........ 26

Figure 2.2. Output power from the passively cooled HL6385DG laser diode when operating time increases. Forward current is 180mA. ........ 27

Figure 2.3. Output power and TEC load of the HL6385DG laser diode. (a) P-I curves at three temperatures. (b) TEC current as a function of forward current at three temperatures. ........ 29

Figure 2.4. Schematic of the high repetition-rate Cr:LiSAF lasers. LD1-LD6, pump laser diodes; PBS, polarizing beam splitting cube; DM1, DM2, dichronic mirror; L1, L2, input lens; M1-M3, curved mirror; HR, high reflector for continuous-wave lasing; OC, output coupler; SAM, saturable absorber mirror. ........ 30

Figure 2.5. Top view of the 3D SolidWorks model of the designed mechanics. ........ 32

Figure 2.6. Continuous-wave Cr:LiSAF laser cavity. (a) Cavity geometry. Numbers shown are in millimeters. (b) Picture of the experiment setup. Solid yellow line shows optical beam path in the cavity. X-tal, Cr:LiSAF laser crystal. Other symbols bear the same meanings as described in Figure 2.4 ........ 34

Figure 2-7. Optical-to-optical efficiency of the continuous-wave Cr:LiSAF laser (0.5% OC). ........ 35

Figure 2.8. 1-GHz modelocked Cr:LiSAF laser cavity. (a) Cavity geometry. Numbers shown are in millimeters. (b) Picture of the experiment setup. Solid yellow line shows optical beam path in the cavity. Symbols bear the same meanings as described in Figure 2.4. .................. 37

Figure 2.9. Measured modelocking results with 0.25% output coupling and six pump diodes. (a) Slope efficiency. (b) RF spectrum. (c) Optical spectrum. (d) Autocorrelation trace. ....... 38

Figure 2.10. SSB phase noise of 250-MHz, 500-MHz and 1-GHz Cr:LiSAF lasers. ............ 39

Figure 3.1. Quantum-limited SSB phase noise at 100-MHz carrier frequency. (a) Gordon-Haus jitter with HWHM gain bandwidth of ~25 THz. (b) Phase noise only due to direct phase noise from ASE. (c) Phase noise due to shot noise. Other parameters used: $n_{sp}=1$, intracavity power = 6 W, 2g = 0.03, D = -100 $fs^2$ and pulse width = 80 fs. ........................................................ 45

Figure 3.2. Single-crystal balanced optical cross-correlation. (a) Illustration of the working principle. (b) Calculated cross-correlation traces for 100fs pulses and a 400-μm thick type-II BBO crystal, in which the green trace is for the forward pass, red for the backward, and the blue for the difference. DM, dichronic mirror; PD1, PD2, the two photodetectors in a balanced photodetector ........................................................................................................ 47

Figure 3.3. BOC measurement sensitivity. (a) As a function of pulse duration, for a 400-μm thick BBO crystal. (b) As a function of crystal thickness, for 100-fs pulses ......................... 48

Figure 3.4. Schematic of the 100-MHz Cr:LiSAF lasers for phase noise characterization. LD1-LD4, HL6385DG laser diodes; L1, L2, 65-mm focal length aspheric doublet; M1, M2, 75-mm ROC DCM mirrors; PBS, polarizing beam splitting cube; DCM, flat dispersion compensation mirrors; SAM, 850-nm semiconductor saturable absorber; PZT1, short-range piezoelectric transducer; PZT2, long-range piezoelectric transducer; X-tal, Cr:LiSAF crystal; OC, ~2% output coupler. ............................................................................................................ 50

Figure 3.5. Schematic of the phase noise measurement system. PBS, polarizing beam splitting cube; HWP, half-wave plate. ........ 50

Figure 3.6. Schematic of the single-crystal BOC. Inset, balanced cross-correlation signal with a slope of 240 mV/fs. HWP, half-wave plate; SM, silver mirror; PBS, polarizing beam splitting cube; LPF, 800-nm long pass optical filter; DM1, dichronic mirror with 800-nm anti-reflection (AR) and 400-nm high-reflection (HR) coating; L, uncoated lens with 48-mm focal length; BBO, 400-μm type-II cut; DM2, 60-mm ROC dichronic mirror with 800-nm HR and 400-nm AR coatings; DM3, 100-mm ROC dichronic mirror with the same coatings as DM2; PD1, PD2, photodetectors of the balanced detector; SC, servo controller; SA, spectrum analyzer; Osc., oscilloscope. ........ 51

Figure 3.7. SSB phase noise PSD of a single laser at 100-MHz carrier. (a) Measured Cr:LiSAF phase noise (b) A range of quantum-limited phase noise estimation. (c) Balanced detector's noise floor. Inset: integrated timing jitter from 50 MHz (d) Cr:LiSAF (e) Balanced detector's noise floor. ........ 52

Figure 3.8. CMRR measurement setup of the modified balanced detector. FA: fixed attenuator; BS: beam splitter; M1: metallic mirror; VA: variable attenuator ........ 54

Figure 3.9. CMRR measurements of the modified balanced detector. From top to bottom: balanced, 5%, 10% and 15% mismatch. ........ 55

Figure 3.10. Phase noise of two values of phase detection sensitivity. The slight roll-off above 1 MHz is due to the detector frequency response. ........ 56

Figure 3.11. Measured relative intensity noise of (a) HL6385DG laser diode. (b) 100-MHz modelocked Cr:LiSAF laser. ........ 59

Figure 3.12. Mode hopping and RIN of the HL6385DG laser diode. (a) Lasing wavelength as a function of the forward current. (b) RIN PSD of the two forward current settings at 25°C. 60

Figure 3.13. Coupling between RIN and phase noise. (a) Measurement setup. (b) Pump RIN mapped to phase noise (dashed), compared with measured phase noise using BOC (solid, reproduced from curve (a) in Figure 3.7) ........ 61

Figure 3.14. Transfer functions (magnitude) from pump RIN to Cr:LiSAF laser RIN. (a) Measured transfer functions. ML: modelocked, cw: continouse-wave (b) Modeled responses using Equations (3.12) and(3.13) ........ 63

Figure 3.15. AM-to-PM conversion factors. (a) Response of SAMs with 1-ps and 10-ps recovery times (b) Absolute value of S*dt/dS in units of one thousandth pulse width for 1ps and >10 ps recovery time. Modulation depth of 1% is assumed. ........ 65

Figure 3.16. Coupling factors due to self-steepening and timing shift on slow saturable absorber (SA) with recovery time longer than 10 ps and S = 8.2. ........ 66

Figure 4.1. Integrated photonic microwave oscillator architecture. Solid lines are optical paths, and dashed lines are signal paths. ........ 73

Figure 4.2. Frequency domain illustration. AM, amplitude modulation; PM, phase modulation; $G$, electronic gain; PFD, phase frequency detector; Servo, servo controller; VCO, voltage-controlled oscillator; SSB Mod, single-sideband modulator; PDH, Pound Drever Hall; PD, photodetector; $f_r$, fundamental pulse repetition rate; $f_0$, remainder of $f_{CEO}$ divided by $f_r$ ........ 74

Figure 4.3. Phase noise model of the ESPIOR, including five successive steps marked with the numbers (1) to (5). $\tilde{\varphi}_{ring}(s)$, phase noise of the microring. Other symbols represents phase noise of the quantities in Figure 4.2. ........ 76

Figure 4.4. Block diagram of the phase-domain LTI noise model of an OPLL. $k_{\text{PFD}}$, phase frequency detector ........ 80

Figure 4.5. PDH loop parameters and attainable phase noise of the stabilized cw laser. (a) 600-Hz linewidth cw laser, and loop bandwidths of 1 MHz, 10 MHz and 100 MHz. (b) Loop bandwidth 1 MHz, and pre-stabilized cw laser linewidth of 600 Hz, 6 kHz and 60 kHz. .... 81

Figure 4.6. Block diagram of the VCO model for the $n^{\text{th}}$ optical comb line. ........ 83

Figure 4.7. Phase noise of the stabilized $n^{\text{th}}$ optical comb line. Loop bandwidth is 10 MHz. 86

Figure 4.8. Phase noise of the repetition rate. (a) Transfer function from the repetition rate to the comb line. (b) Phase noise of the repetition rate; the optical frequency division ratio is >70 dB. ........ 87

Figure 4.9. Optical frequency division at different gain values. (a) Effective OFD ratio, 192 THz to 20 GHz. (b) Loop instability. Loop is unstable if the instability exceeds unity. ........ 88

Figure 4.10. Phase noise at 1-Hz and 10-kHz for different modulation bandwidths ........ 89

Figure 4.11. Frequency noise and phase noise of the Ethernal SlowLight laser. ........ 91

Figure 4.12. Optical phase locked loop for modelocked laser stabilization. ........ 92

Figure 4.13. Beat signal of $\nu_n$ and $\nu_{\text{cw1}}$. Resolution bandwidth 30 Hz. Center frequency 325 MHz. ........ 93

Figure 4.14. Phase noise of the pulse repetition rate, with and without the proportional gain applied. ........ 94

Figure 4.15. Optical phase locked loops for microwave readout. The PZT loop is not shown. ........ 95

Figure 4.16. Optical beat signals of the OPLLs in microwave readout. (a) The AOFS loop. (b) The SSB phase modulator loop. Both, resolution bandwidths 30 Hz, residual timing jitter 0.2 fs (<100 kHz). ........ 96

Figure 4.17. Extracted microwave signals. (a) RF spectrum. (b) Phase noise at 5-GHz carrier frequency ........ 96

## List of Tables

Table 2.1. Summary of modelocked lasing results. 36

Table 4.1. Parameters of the PDH loop. 78

Table 4.2. Parameters of the cw laser. 79

Table 4.3. Parameters of the modelocked laser. 85

# Chapter 1

# Introduction

## 1.1 Low-Noise Microwave Oscillators and Applications

Precision microwave oscillators are critical to a wide range of applications in which frequency stability and timing accuracy are essential to performance. Often, the timing error $\Delta t$ is represented as the phase error $\Delta\varphi = (2\pi f_c)\Delta t$ at a given carrier frequency $f_c$. Power spectral density (PSD) of the phase error is commonly referred to as the phase noise $S_\varphi(f) = \int_{-\infty}^{+\infty} \langle \Delta\varphi(t)\Delta\varphi(t+\tau)\rangle e^{i(2\pi f)\tau} d\tau$, where $f$ is the offset frequency from the carrier. According to the IEEE standard [1], the phase noise is usually denoted by the single-sideband (SSB) phase noise $\mathcal{L}(f) = \frac{1}{2} S_\varphi(f)$. Phase noise is measured by comparing the test oscillator to a reference oscillator with a phase-sensitive detector. Frequency noise $S_{f_c}(f)$ of the carrier frequency is related to the phase noise by $S_\varphi(f) = f^{-2} S_{f_c}(f)$. The phase noise and frequency noise representations scale with $f_c$. For instance, to convert the phase noise from 100-MHz carrier frequency to 10-GHz, $S_\varphi(f)$ increases by $20 \times \log_{10}(10^{10}/10^{8}) = 40$ dB.

The primary drivers of low-noise microwave oscillators are military, aerospace, metrology and research needs. In these cases, long-term stability, low noise, high energy efficiency and compactness are always desired or required. The application in Doppler RADAR (RAdio Detection And Ranging) systems is a good example to illustrate the need of low-phase noise oscillators. The Doppler frequency shift of a moving target is $f_\mathrm{d} = 2f_\mathrm{t}v_\mathrm{r}/c$ [2], where $f_\mathrm{t}$ is the RADAR frequency, $v_\mathrm{r}$ the radial velocity of the target toward the transceiver, and $c$ the speed of light in air. For a slowly moving target, the frequency shift is quite small compared with the RADAR frequency. For example, a man walking at $v_\mathrm{r} = 1.1$ m/s corresponds to $f_\mathrm{d} = 70$ Hz for an X-band RADAR at 10 GHz. Close-to-carrier phase noise of the transceiver local oscillator thus becomes important, and must be significantly lower than that of the detectable scattered signal. It has been stated that to detect the aforementioned moving object with a 90% probability of detection, the phase noise requirement has to be -130 dBc/Hz at 70-Hz offset frequency [3].

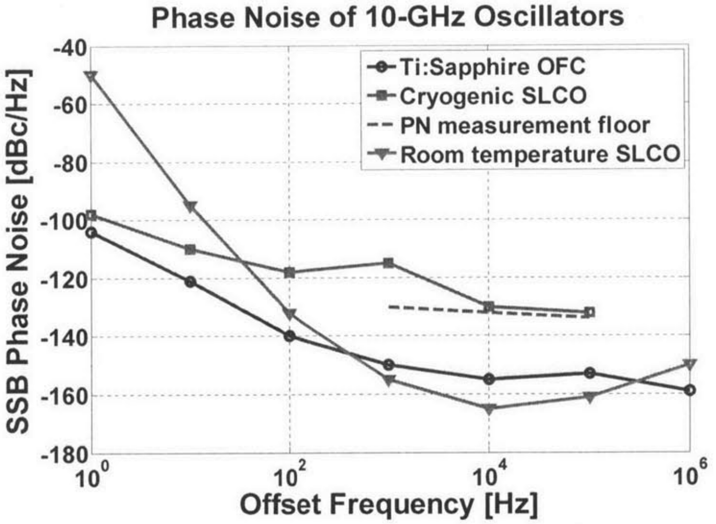

Figure 1.1. Phase noise of three types of microwave oscillators. OFC, optical frequency comb; SLCO, sapphire loaded cavity oscillator; PN, phase noise.

Long-term stability of free-running microwave oscillators is affected by environment perturbations, including mechanical shock and vibration, and thermal fluctuation. Suppression of low-frequency noise therefore becomes necessary, and precision temperature control and careful vibration isolation are critical to system performance. Two types of microwave oscillators that represent the state-of-the-art performance are the Sapphire Loaded Cavity Oscillator (SLCO) [4, 5] and the photonic microwave oscillators based on optical frequency comb (OFC) and ultrastable continuous-wave (cw) laser [6]. Phase noise of these oscillators are reproduced in Figure 1.1. The SLCO employs a high electrical quality-factor (Q-factor) sapphire plate as the dielectric material. The electrical Q-factor determines noise performance, as expressed in Leeson's equation [7]. The sapphire plate has an extremely low loss tangent in the cryogenic environment (temperature $< 4$ K) [8], and a Q-factor of $\sim 10^9$ can be achieved [9]. In contrast, the photonic microwave oscillators utilizes an ultrastable optical cavity, which is engineered to be athermal and immune to mechanical acceleration, as the ultimate frequency reference. Microwave signal is extracted by photodetecting the laser pulse train. Typically, the reference cavity is a rigid Fabry-Pérot optical cavity made of Ultra Low Expansion (ULE) glass, which has a mechanical Q-factor of $6.1 \times 10^4$ [10]. The most advanced optical reference cavity is made of silicon single crystal, which has close-to-zero thermal expansion at 124 K temperature and a mechanical Q-factor $> 10^7$ [11].

Both the SLCO and Ti:sapphire based microwave oscillator are heavy and bulky, although the latter technology enables extremely low phase noise at both low and high offset frequencies and does not need cryogenic cooling. Wide use of this technology out of the laboratory requires implementing femtosecond modelocked lasers, ultrastable reference cavity, and electronics in a compact package, and ultimately on a hybrid photonic-electronic chip of a few $cm^2$ area.

## 1.2 Diode Pumped Femtosecond Cr:Colquiriite Lasers

Femtosecond Cr:Colquiriite lasers are suitable for microwave oscillator applications. Compared with the Ti:sapphire ultrafast lasers, they have the advantages of lower cost, high electrical-to-optical conversion efficiency and compactness [12]. This technology is enabled by direct laser diode pumping and the availability of low-cost and highly efficient red laser diodes at ~650nm. Cr:Colquiriite lasers are also suitable as gain media for ultrashort pulse generation. Although the gain bandwidth is not as broad as that of Ti:sapphire crystals, it does enable femtosecond pulse generation with pulse duration as short as ~10 fs [13]. Moreover, Cr:Colquiriite has a low lasing threshold, which could be below 10 mW. In conjunction with the capability of direct diode pumping and relatively low quantum defect, Cr:Colquiriite enables highly efficient lasing operation compared with Ti:sapphire lasers. The overall electrical-to-optical conversion efficiency of Cr:Colquiriite could reach ~10% [14, 15].

The development of Cr:Colquiriite lasers is an active research field. The efforts have been mainly focused on pulse energy scaling, pulse duration compression and broaden tuning range in cw and modelocked Cr:LiCAF and Cr:LiSAF lasers. In particular, the first Cr:LiCAF laser modelocked by a semiconductor saturable absorber [16, 17] was demonstrated in 2007 [18]. The first single-mode diode pumped Cr:LiCAF was reported in 2008 [14]. In 2009, the first extended cavity Cr:LiCAF laser was constructed [19]. In addition, 105-nm broad tuning range and >100 nJ pulse energy in Cr:LiSAF were achieved using broadband oxidized saturable absorber and cavity dumping technique, respectively [20, 21]. The disadvantage of

Cr:Colquiriite compared with Ti:sapphire include modest gain and inferior thermal and mechanical properties. This suggests the importance of high-quality intracavity optics and careful heat sinking in designing and building Cr:Colquiriite lasers. In particular, the thermal quenching effect hinders increasing average output power of Cr:LiSAF lasers.

Compact Cr:LiSAF lasers have been previously demonstrated. For example, the 400-MHz system has a footprint about the size of letter size paper, and generates 5 mW output power when pumped by a single battery-powered laser diode [22]. The highest repetition rate achieved is 1 GHz [23], and the average output power is 3.2 mW. However, the power level of these lasers is insufficient in many desirable applications, mainly due to the lack of efficient pump diodes at that time, as well as limitations in the saturable absorber design and dispersion compensation.

## 1.3 Optical Frequency Division

The OFC generated by a femtosecond modelocked laser has been proven to be equally spaced with an offset frequency [24], which is described by the comb equation $\nu_n = f_0 + n \cdot f_r$, where $\nu_n$ is frequency of the $n^{\text{th}}$ comb line, and $f_0$ is the remainder of the carrier-envelope-offset (CEO) frequency ($f_{\text{CEO}}$) divided by $f_r$. The OFC links the microwave frequencies $f_0$ and $f_r$, and the optical frequency $\nu_n$. Consequently it has become an agile frequency synthesizer [25].

In photonic microwave oscillators, the OFC is configured as an optical frequency divider that down-converts an optical frequency into microwave domain. When the $n^{\text{th}}$ optical comb line is phase locked to a reference single-frequency $\nu_{\text{ref}}$, the comb spacing is

$f_r = (\nu_n - f_0)/n$ and its frequency noise is $S_r(f) \approx S_n(f)/n^2$, assuming CEO frequency has been sufficiently stabilized. Because the comb index $n$ is quite large, the factor $n^2$ dramatically reduces noise of the microwave frequency $f_r$, which can be extracted from the pulse train by direct photodetection.

Optical frequency division (OFD) is less effective without $f_{\mathrm{CEO}}$ stabilization. Experiments on ytterbium-erbium (Yb-Er) co-doped fiber lasers [26], as well as our experiments on Er-doped fiber lasers and Ti:sapphire lasers, show that it does not necessarily reduce timing jitter within the locking bandwidths with $f_{\mathrm{CEO}}$ free-running, even though cavity length is modulated. This is attributed to frequency comb dynamics [27] and coupling among different modulation mechanisms [28, 29]. The conventional $f_{\mathrm{CEO}}$ stabilization scheme is not yet available on chip, which is a conundrum of realizing integrated photonics microwave oscillators.

## 1.4 Thesis Outline

The rest of this thesis is organized as follows. Chapter 2 describes high repetition-rate femtosecond Cr:LiSAF lasers. Laser systems are developed for stable cw-modelocking operation ranging in fundamental repetition rates from 200 MHz to 1 GHz [30, 31]. The challenges of building a reliable system and solutions to circumvent these difficulties are addressed. Chapter 3 gives analysis and measurement of the phase noise of saturable absorber modelocked Cr:LiSAF lasers [32, 33]. Analytical solutions of intensity noise and timing jitter represented in phase noise are revisited and applied to the Cr:LiSAF lasers. The impact of amplitude modulation to phase modulation (AM-to-PM) coupling on timing jitter is analyzed.

Timing jitter of 100-MHz repetition-rate femtosecond Cr:LiSAF lasers are experimentally measured with a single-crystal balanced optical cross-correlator. Chapter 4 discusses phase noise of the Erbium Silicon Photonic Integrated OscillatoR (ESPIOR). In addition, a demonstration system based on fiber lasers and fiber-optic components is constructed. An 80-dB division ratio from 192 THz to 1 GHz is achieved without an $f-2f$ interferometer and carrier-envelope-phase locking [34]. The impact of CEO frequency noise of a free-running modelocked laser on phase noise of the re-generated microwave is studied. Finally, Chapter 5 summarizes the thesis and discusses future work.

# Chapter 2

# High Repetition-Rate Cr:LiSAF Femtosecond Lasers

## 2.1 Motivation

High repetition-rate femtosecond lasers are indispensable components in the applications that favor large comb spacing. A typical example is wavelength calibration of astrophysical spectrographs, for which an optical frequency comb (known as the "astro-comb") is employed as a frequency reference of excellent accuracy and long-term stability [35, 36]. Comb spacing of more than 10 GHz are usually required so that individual astro-comb lines can be resolved. Another application demanding repetition rates beyond 10 GHz is the implementation of photonic microwave oscillators [6, 37-39], in which the high repetition-rate optical pulse train is photodetected as ultralow-noise microwave signals. Because microwave carrier frequencies in the X-band (8 GHz to 12 GHz) or the K-band (18 GHz to 26.5 GHz) are often demanded in real applications, laser pulse trains of 10 GHz or 20 GHz repetition rates are required. In addition, high repetition-rate modelocked lasers have found promising applications in high-speed optical sampling and photonic analog-to-digital conversion (PADC) [40, 41], optical imaging [42], and high-speed optical communication [43]. In PADC, laser pulse repetition rate essentially limits sampling rate. In the imaging application, high pulse repetition rate leads to increasing excitation efficiency of fluorophores.

It is challenging to build femtosecond lasers of tens of GHz fundamental repetition rate. One common scheme instead is to use an external optical mode filter, which rejects unwanted comb lines from a relatively low repetition-rate pulse train and therefore increases comb line spacing. Cascaded Fabry-Pérot cavities [44, 45] and cascaded Mach-Zehnder interferometers [46, 47] are the two types of repetition-rate multipliers typically utilized to increase comb spacing from < 1 GHz to beyond 10 GHz. These mode filters, however, have limited side-mode suppression ratio. The residual side-modes can be re-amplified in the nonlinear optical processes [48], for example frequency doubling and spectrum broadening, which are necessary in many applications. Moreover, multiple filtering stages add system complexity. Studies have shown that the radial-velocity calibration error of astrophysical spectrographs significantly depends on the sequence of successive amplification and mode filter stages [49], and phase noise of photonically generated microwaves is extremely sensitive to path length variation of the Mach-Zehnder interferometers [50]. Consequently, it is beneficial to build femtosecond lasers of GHz fundamental repetition rate because the large mode spacing directly reduces the number of side modes within the filter transmission bandwidth. When less filtering stages are needed, the reduced system complexity improves stability and robustness.

Fundamentally modelocked femtosecond solid-state lasers with GHz pulse repetition rates are rarely reported mainly because of the technical difficulties of miniature opto-mechanical system design, heat management and effective dispersion compensation with few intracavity components. It is even more challenging when practical applications put stringent requirements on pulse energy and peak power directly from the GHz oscillators. Kerr lens modelocked Ti:sapphire lasers operating at 1 GHz [51, 52], 2 GHz [53, 54], 5 GHz [55], and 10 GHz [56, 57] repetition rates have been reported in the past years. However, Ti:sapphire lasers usually require a frequency-doubled neodymium pump laser, which makes the overall system bulky and expensive, in addition to having a low electrical-to-optical conversion efficiency.

Directly diode-pumped solid-state lasers modelocked by semiconductor saturable absorbers are promising alternatives due to their compactness and low cost. Although repetition rates as high as 160 GHz and 100 GHz have been demonstrated in diode-pumped Nd:$YVO_4$ [58] and Er:Yb:glass [59] lasers, respectively, both fundamentally modelocked with semiconductor saturable absorbers, these systems provide only picosecond pulses with limited peak power and spectral bandwidth. The highest repetition rate achieved in modelocked Cr:LiSAF is 1 GHz in 2001 [23], though the average output power is only 3.2 mW (~20-W peak power), insufficient in many desirable applications. The low peak power (~20 W) is due to the lack of efficient pump diodes at that time, as well as limitations in the SBR design and dispersion compensation. Since the initial introduction of GHz Cr:LiSAF lasers, several enabling technologies have emerged. This motivates research on high repetition rate Cr:LiSAF lasers that produce ultrashort pulses with high peak power and pulse energy.

## 2.2 Laser Design

### 2.2.1 Laser Diode Pump Unit

One of the absorption bands of Cr:LiSAF centers around 650 nm with a broad bandwidth of ~100 nm [60]. This feature enables direct laser diode pumping with low-cost and widely available AlGaAs or AlGaInP laser diodes of single transverse mode. Two types of commercial off-the-shelf products were available at the time when high power tapered lasers at 650 nm [61] were unavailable. The HL6545MG and HL6385DG (Opnext) are AlGaInP laser diodes with a multi-quantum well structure, originally developed as light sources primarily for recordable-DVD and laser display. Beam divergence angles parallel and perpendicular to the junction are 10° and 17°, respectively. A customized cylindrical microlens (Blue Sky Research) shapes the beam profile to circular beam with $M^2 < 1.1$ [12]. In addition, an $f = 7.5$ mm achromatic doublet lens (AC050-008-A, Thorlabs) is used to collimate the beam.

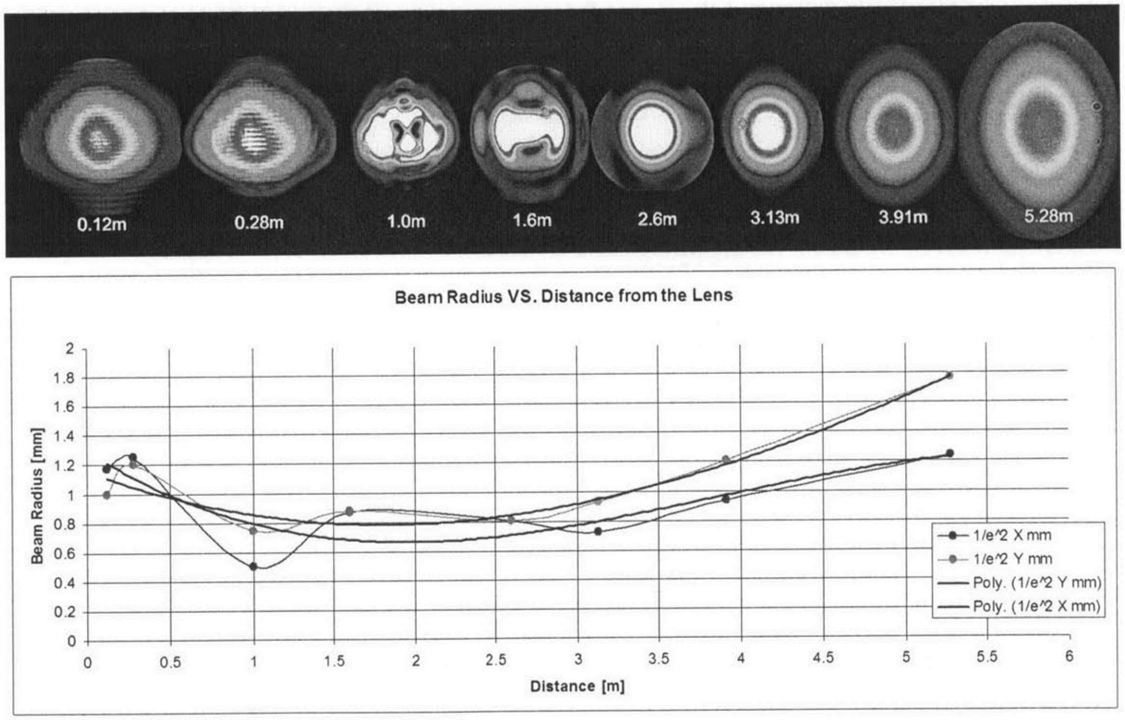

Figure 2.1. Collimated beam profile of the HL6385DG laser diode. Above, beam cross sections as a function of the distance from the collimating lens. Below, beam radii in x and y directions.

Figure 2.1 shows the collimated beam profile at different positions after the collimating lens, and the corresponding beam radii in x and y directions[1]. Although the beam profiles deviate from Gaussian profile, we have not observed any adverse effect on lasing performance of Cr:LiSAF lasers.

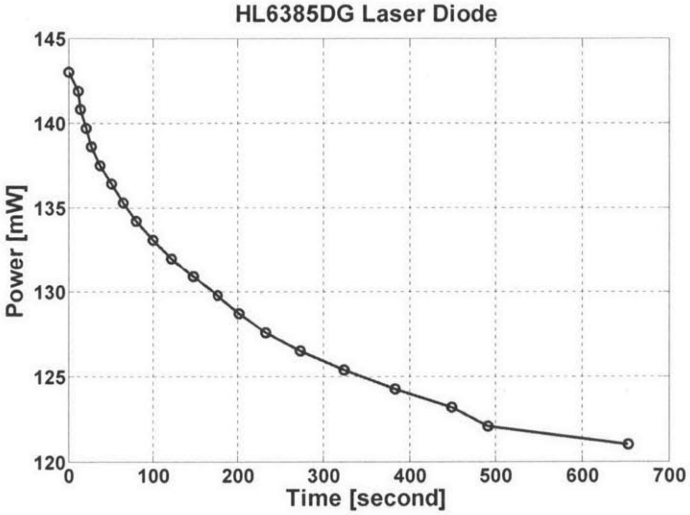

Figure 2.2. Output power from the passively cooled HL6385DG laser diode when operating time increases. Forward current is 180mA.

At 25 °C without active cooling, the HL6545MG outputs 130 mW at 660 nm when driven by 180 mA, and the HL6385DG outputs 150 mW at 642 nm when drive by 280 mA. Our observation shows that passive heat sinking (mounting laser diodes on a 224-M from Arroyo Instruments) is insufficient to keep the HL6385DG running at its standard rating at 25 °C. Figure 2.2 shows that the output power drops by ~15% since the laser diode was turned on for ~10 minutes[2]. It is therefore necessary to stabilize the case temperature. Moreover, it is possible to drive the laser diodes above their room temperature ratings with the help of water or thermoelectric cooling. Figure 2.3 shows the output power and TEC current of the HL6283DG when its case temperature is stabilized at three temperatures[3]. Our experiments prove that the 150-mW HL6385DG can generate more than 200 mW at 20 °C when driven by 350 mA and actively cooled by a thermoelectric cooler (TEC) in contact with the laser diode case. Under this setting, no damage or performance deterioration has been observed.

---

[1] The figure is provided through the courtesy of Jing Wang.

[2] Measured by Jing Wang.

It is feasible to combine the beam of four laser diodes through a combination of polarization coupling and wavelength multiplexing. Because the wavelengths of HL6545MG and HL6385DG only differ by ~20 nm, coupling loss due to the not-so-sharp transmission edge of a dichromic mirror is usually higher than the loss from a polarizing beam splitting cube. In this light, two 150-mW laser diodes are polarization combined, and two 130-mW laser diodes are wavelength multiplexed using a dichronic mirror in each polarization. Previous measurements showed that Cr:Colquiriite crystals absorb TM-polarized pump power > 15% more than TE-polarized pump power [12]. When mounted in the temperature-controlled laser mount 224-M from Arroyo Instruments, output from the laser diode is TE polarized. A half-wave plate or re-wiring of the laser diode pins can effectively rotate the default polarization to TM. It turns out that up to three diodes in each pump unit already provide sufficient pump power in our experiments. The pump unit including two HL6385DG and one HL6545MG provides 430 mW average power without active cooling; when cooled by TEC, it produces > 600 mW average power.

Both forward current and case temperature change lasing longitudinal modes and the operating wavelength of the laser diode, and may cause mode hopping and significant high-frequency intensity noise. This is further discussed in Chapter 3, where laser noise is a major concern.

---

[3] Measured by Jing Wang.

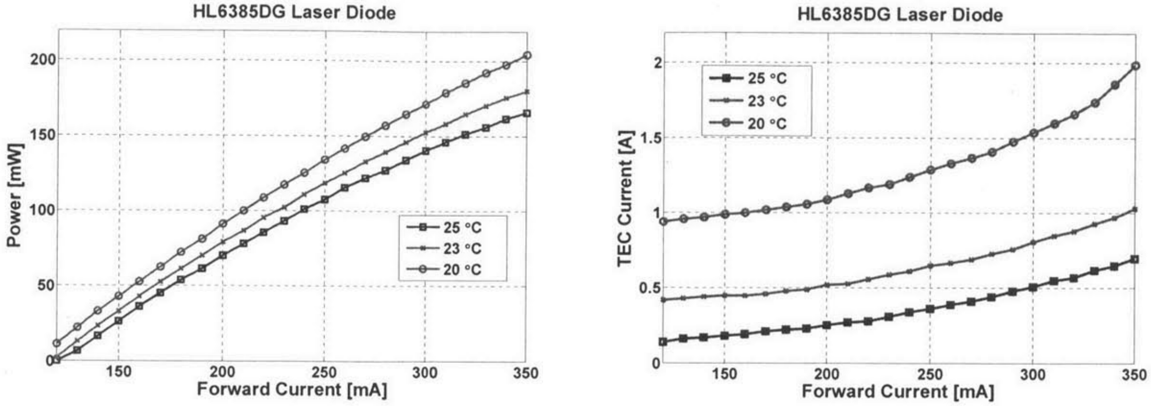

(a) (b)

Figure 2.3. Output power and TEC load of the HL6385DG laser diode. (a) P-I curves at three temperatures. (b) TEC current as a function of forward current at three temperatures.

Both HL6545MG and HL6385DG operate at ~2.5 V voltage with an electrical-to-optical efficiency of ~30% and ~20%, respectively. The pump unit can be driven by miniature constant current sources, for example the LDDP400 or FL593 from Wavelength Electronics. The current sources can then be powered by a low-resistance lead-acid battery, such as the Power-Sonic PS-6100-F1. Our experiments show that a single 12-Ah battery pack is sufficient to run the pump unit for several hours. When the laser diodes are temperature controlled, the TEC may consume a significant amount of power. However, a mini temperature controller such as the WTC3293-14001 from Wavelength Electronics can replace the commonly used bench top instrument, while it is still possible to be powered with a dedicated lead-acid battery. Such a compact and efficient pump unit gives Cr:LiSAF lasers a clear advantage over Ti:sapphire systems in terms of portability, as the frequency-doubled neodymium pump laser fundamentally limits energy efficiency and footprint of high repetition-rate Ti:sapphire laser systems, even though the oscillator cavity itself is compact. Additionally, cost per watt of our pump unit is only a fraction of the price of a commercial frequency-doubled neodymium pump.

### 2.2.2 Laser Cavity Design

In terms of cavity design, high repetition-rate Cr:LiSAF lasers share many similarities with the standard 100-MHz diode-pumped Cr:Colquiriite lasers [12]. However, a number of problems arise as cavity length shrinks to increase the repetition rate. For instance, suppressing Q-switched modelocking is more challenging at high repetition rates due to the reduced intracavity pulse energy. Stable operation requires the saturable absorber to have relatively low saturation flux and modulation depth. In addition, active cooling of the SBR is necessary, especially when low output coupling is used to increase the intracavity power.

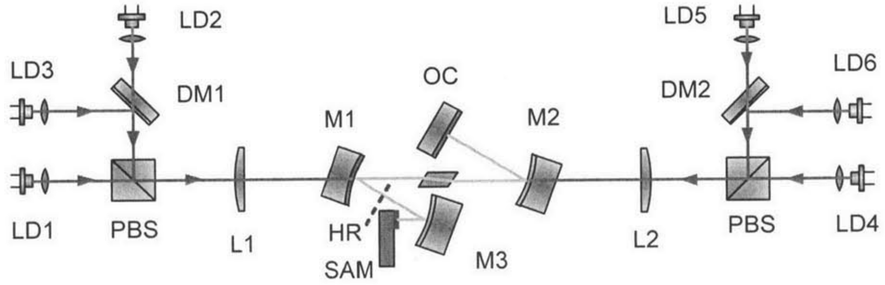

Figure 2.4. Schematic of the high repetition-rate Cr:LiSAF lasers. LD1-LD6, pump laser diodes; PBS, polarizing beam splitting cube; DM1, DM2, dichronic mirror; L1, L2, input lens; M1-M3, curved mirror; HR, high reflector for continuous-wave lasing; OC, output coupler; SAM, saturable absorber mirror.

The high repetition-rate Cr:LiSAF laser, shown schematically in Figure 2.4, consists of a standard z-shape astigmatically compensated cavity. The gain medium is a 6-mm long, 1.5-mm thick, 1.5% Cr-doped, Brewster-cut Cr:LiSAF crystal. Six single-mode laser diodes (LD1-LD6) are symmetrically pumping both sides of the crystal in order to balance the thermal load. It is measured that the crystal absorbs 84% of TE-polarized pump power, and 97% of TM-polarized. Because the absorption power difference is only ~23 mW for a single 660-nm laser diode, we did not choose to rotate its polarization to TM. On one side, TE-polarized LD2 (at 640 nm, HL6385DG) and LD3 (at 660 nm, HL6545MG) are wavelength multiplexed by a dichronic mirror (DM1), and then combined with TM-polarized LD1 (at 640 nm, HL6385DG) by using a polarizing beam splitting cube (PBS). The other side has an identical pumping configuration. The 640 nm diodes are cooled to 20 °C by a TEC, whereas no active cooling is applied to the 660 nm diodes. The Cr:LiSAF crystal absorbs approximately 900 mW of the 1W incident pump power.

In order to reduce cavity length, radius of curvature (ROC) of the pump mirrors (M1 and M2) are changed to 50 mm from 75 mm. The 75-mm ROC is typically used in 100-MHz Cr:Colquiriite lasers [12]. These pump mirrors (from Layertec) have high reflectivity at the lasing wavelength range (775-1000 nm) and a low reflectivity at the pump wavelengths (620-680 nm). The astigmatism compensation angle is ~13° for the Cr:LiSAF crystal in use. M2 and M3 are specially-designed dispersion compensation mirrors. In continuous-wave lasing, a high reflector (HR) (from Layertec) is placed in one arm. In modelocked lasing, the HR is replaced by a folding mirror (M3 in the figure) to image the saturable absorber mirror (SAM) to the original HR plane. Changing the ROC and position of the folding mirror also allows varying the beam spot size on the SAM. We have used M3 mirror with ROCs of 100 mm, 25 mm and 10 mm to achieve spot radii from ~20 μm to 60 μm, according to the calculations of ABCD matrices [62]. The corresponding beam waists inside the Cr:LiSAF crystal are from ~30 μm to 70 μm. Output couplers with 0.25% or 0.5% transmission are used to maintain high intra-cavity power levels.

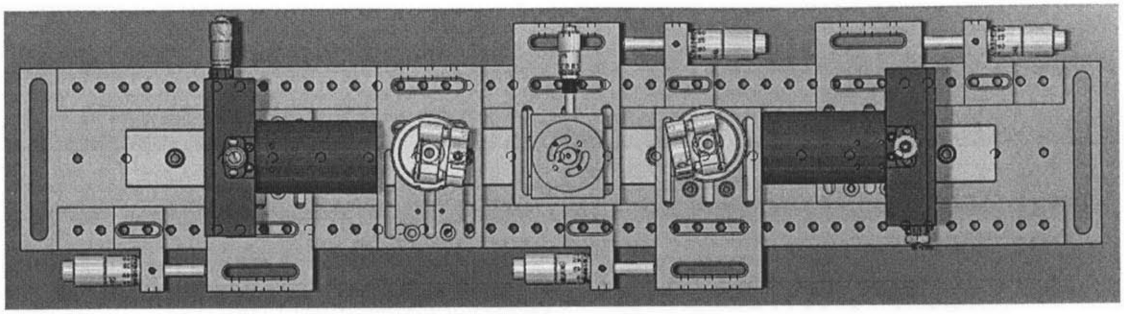

Figure 2.5. Top view of the 3D SolidWorks model of the designed mechanics.

A modular opto-mechanical system is designed to facilitate laser cavity alignment as we alter cavity length to build lasers with various repetition rates. The mechanics shown in Figure 2.5 holds the input lenses, pump mirror and laser crystal holder on a single base plate with a stainless steel linear motion rolling guide and slide units (LWLF series, IKO). Each slide unit carries an adapter plate designed to mount commercial off-the-shelf translation lens mounts, pedestal pillar posts and translation stages. Spring-loaded micrometer drives ensure precision adjustment of the spacing between the mounted components. The design also decouples the adjustments of astigmatism compensation angle, Brewster angle, and optical axis shift after the laser crystal. The copper crystal holder can be adapted for water cooling or TEC cooling. In general, the design are suited to the requirement of most four-mirror and three-mirror solid-state laser cavities.

Self-starting and stable modelocking is enabled by the SAM. Suppressing Q-switched modelocking instabilities is more challenging at high repetition rates due to the reduced intracavity pulse energy [63]. Therefore, stable operation requires the SAM to have relatively low saturation flux and modulation depth. In our experiments, the SAM has twenty-five pairs of $Al_{0.95}Ga_{0.05}As/Al_{0.17}Ga_{0.83}As$ quarter-wave layers as the Bragg stack, a 25 nm-thick GaAs layer serving as the saturable absorber and one $SiO_2$-$TiO_2$ pair serving as a high-reflection (HR) coating on the surface. The design is identical to that in reference [64], except for the additional top HR coating which reduces the modulation depth from ~2% to ~0.7%. The HR coating also reduces the overall absorption and thermal load, thus lowering the risk of thermal damage.

Femtosecond pulses at GHz repetition rate are generated when both the spot-size on the SAM and the cavity dispersion are optimized. To compensate for the intracavity positive group delay dispersion (GDD), and to support ~50-fs pulses over a wide range of center wavelengths for Cr:LiSAF, the dispersion compensating mirrors are designed to produce approximately -80±10 $fs^2$ GDD per bounce over 150 nm of bandwidth (800-950 nm). In addition, these mirrors also cancel the third order dispersion of the Cr:LiSAF crystal. This customized design is enabled by an efficient analytical computation method that calculates and optimizes dispersion (to any order) of multilayer coating with high accuracy [65, 66]. Because the mirror designed for Cr:LiSAF lasers requires less bandwidth than for Ti:sapphire lasers, higher GDD compensation can be achieved with minimal unwanted oscillations in dispersion. When two of these mirrors are used (four bounces in total), the overall round-trip GDD of the cavity is estimated to be approximately -60 $fs^2$. Note that commercial broadband dispersion compensating mirrors with a flat GDD curve generally provide only ~ -40 $fs^2$ of GDD per bounce, which is insufficient to provide the required negative dispersion.

## 2.3 Continuous-Wave and Modelocked Lasing Results

We have constructed Cr:LiSAF lasers with various cavity lengths. Continuous-wave lasing is achieved with a high reflector in one cavity arm. The two asymmetric arm lengths and pump mirror separation are chosen according to the cavity stability analysis using a standard ABCD matrices calculation. As an example, the cavity layout illustrated in Figure 2.6 is later used to build the 1-GHz repetition-rate modelocked Cr:LiSAF laser. The arm lengths and mirror separations are shown in the unit of millimeter. Output coupling ratios of 0.5% and 0.25% are used, and pump mirrors M1 and M2 have the same ROC of 50 mm.

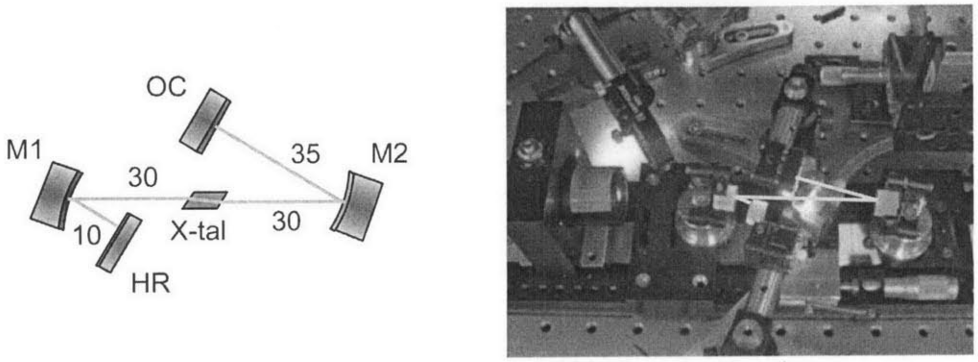

(a) (b)

Figure 2.6. Continuous-wave Cr:LiSAF laser cavity. (a) Cavity geometry. Numbers shown are in millimeters. (b) Picture of the experiment setup. Solid yellow line shows optical beam path in the cavity. X-tal, Cr:LiSAF laser crystal. Other symbols bear the same meanings as described in Figure 2.4.

Up to six laser diodes are used to pump the laser. When 5% output coupling is used, the output power as a function of absorbed pump power is shown in Figure 2-7. The lasing threshold is at 190 mW of pump power, and the maximum output power is 360 mW. The overall optical-to-optical slope efficiency is 40%, corresponding to ~10% electrical-to-optical efficiency. Linearity of the curve in Figure 2-7 suggests the pump diodes are well aligned, except a slight misalignment of LD5. Without a sign of pump saturation, more output power can be expected with stronger pump power. If the output coupler is changed to 0.25%, the maximum output power reduces to ~300 mW with a slightly increased optical-to-optical efficiency of 43%.

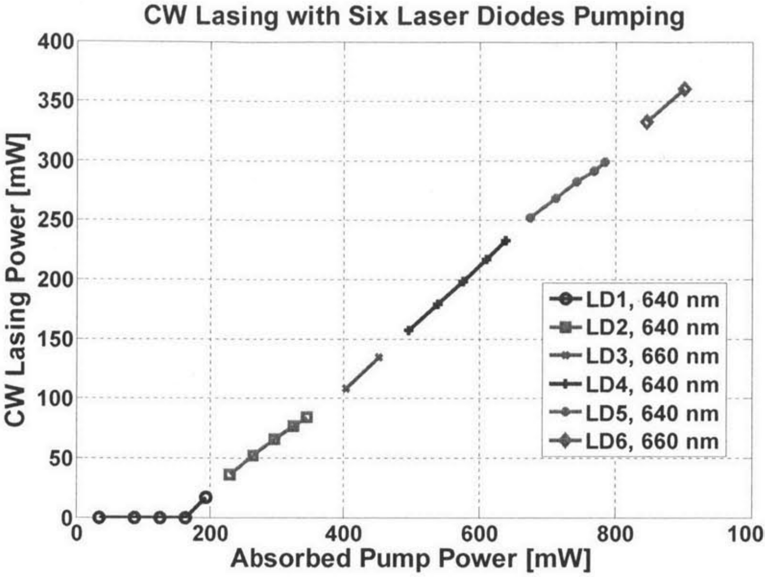

Figure 2-7. Optical-to-optical efficiency of the continuous-wave Cr:LiSAF laser (0.5% OC).

In building the modelocked Cr:LiSAF lasers, we start from a 3-m round-trip length, which corresponds to 100-MHz repetition rate, and then gradually reduce the cavity length down to 150 mm to achieve 1-GHz repetition rate. Modelocking performance at four repetition rates is summarized in Table 2.1. The results are all obtained with 0.5% output coupling ratio and four HL6385DG laser diodes. The maximum absorbed pump power is 700 mW. Thermal damage of the SAM, which is glued on an aluminum mirror, is observed when the pulse repetition rate is beyond 500 MHz. By using thermal conducting adhesive and a copper holder, stable modelocking at the 660-MHz repetition rate is achieved. Active cooling of the SAM is necessary when the repetition rate further increases. The cooling is achieved by mounting the SAM on a copper block attached to a water-cooled TEC that keeps the SAM temperature at 1 °C. Nitrogen purging is used to prevent water condensation. TEC cooling, however, is primarily necessary to prevent damage on the SAM during the alignment process when Q-switching instabilities are more likely to occur. Once the laser is running in the cw modelocked regime, water cooling is sufficient.

Table 2.1. Summary of modelocked lasing results.

| Repetition Rate (MHz) | Average Power (mW) | Pulse Width (fs) | Pulse Energy (nJ) | Spectrum Bandwidth (nm) |
|---|---|---|---|---|
| 266 | 123 | 80 | 0.4 | 8.7 @ 867 |
| 552 | 114 | 120 | 0.2 | 7 @ 867 |
| 660 | 126 | 140 | 0.2 | 4.2 @ 866 |
| 843 | 102 | 50 | 0.12 | 17 @ 859 |
| 1000 | 107 | 106 | 0.11 | 8.7 @ 865 |

The best modelocking results are obtained with a 0.25% output coupler and six pump-diodes. The cavity geometry is shown in Figure 2.8. Compared with the layout of continuous-wave lasing, the folding mirror M3 images the SAM to the original HR plane (shown as the dashed line), resulting in a ~25-μm beam waist on the SAM. Modelocking performance is summarized in Figure 2.9. Mode-locking self-starts and the laser is immune to environmental fluctuations. Stable cw modelocking is obtained when the pump power is above 500 mW, with a slope efficiency of ~14%. Below 500 mW of pump power. Q-switched modelocking is observed until the pump power is decreased below 350 mW. Pure cw output occurs down to the lasing threshold at ~230 mW, as shown in Figure 2.9 (a). The RF-spectrum was recorded with a photodiode and RF spectrum analyzer and shows a ~1-GHz peak, which is 80-dB above the background level (Figure 2.9 (b)). The optical spectrum has a bandwidth of ~17.3 nm centered around 863 nm (Figure 2.9 (c)). The autocorrelation has a full-width-at-half-maximum (FWHM) of ~88 fs (Figure 2.9 (d)), corresponding to 55-fs pulse width (assuming a sech$^2$ pulse shape). The corresponding time-bandwidth product is 0.38, close to the transform-limited value of 0.315 for sech$^2$ pulses. When pumped with six laser diodes at full power, the 110-mW average output power corresponds to a pulse energy of 110 pJ and peak power of 1.8 kW. This represents almost two orders of magnitude improvement in the output peak power over previous results. When pumped by four 640-nm laser diodes, the Cr:LiSAF laser generates 72-fs pulses with an average power of 84 mW, which corresponds to a pulse energy of 80 pJ and peak power of 1.0 kW.

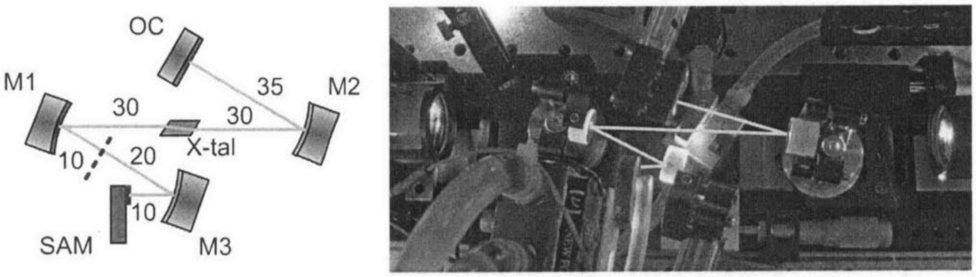

(a)

(b)

Figure 2.8. 1-GHz modelocked Cr:LiSAF laser cavity. (a) Cavity geometry. Numbers shown are in millimeters. (b) Picture of the experiment setup. Solid yellow line shows optical beam path in the cavity. Symbols bear the same meanings as described in Figure 2.4.

When the output coupling is increased to 0.5%, the Cr:LiSAF laser generates 85-fs pulses with 147 mW average power (1.45 kW peak power) when six laser diodes are used; when four 640-nm laser diodes are used, the laser produces 106-fs pulses with 107-mW average power (0.83 kW peak power). As expected, higher output coupling enables higher average power at the expense of increased pulse width, due to the decreased intracavity power levels.

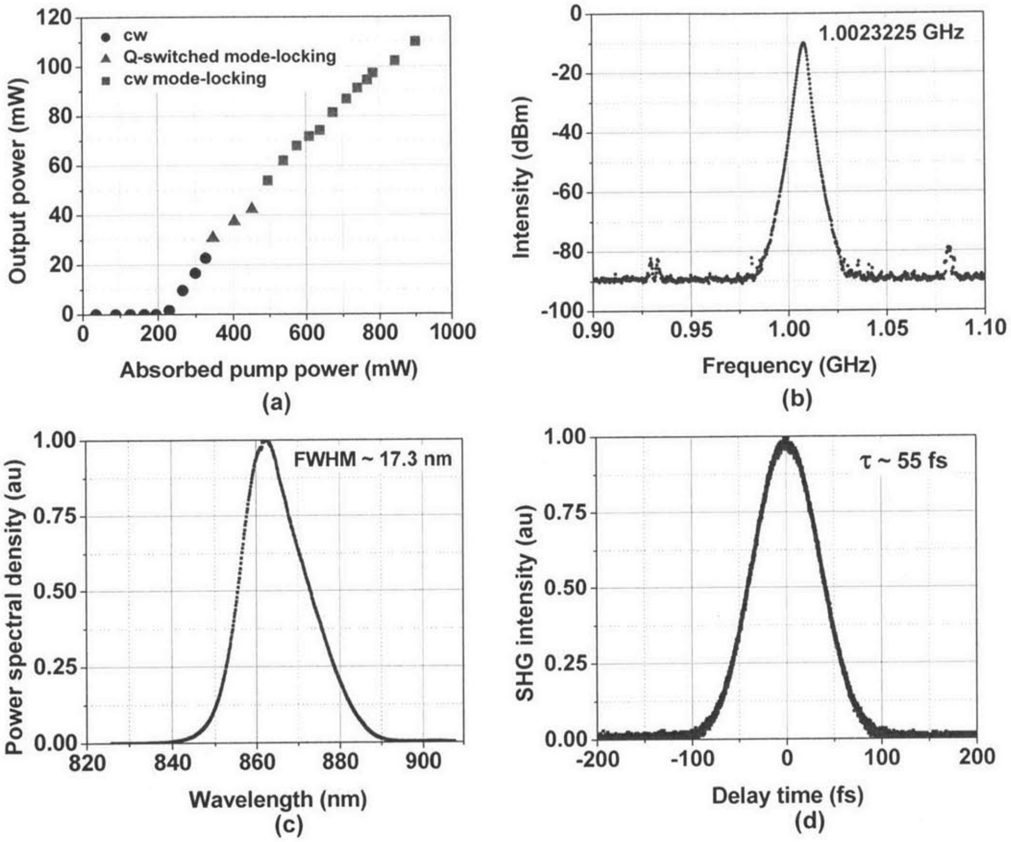

Figure 2.9. Measured modelocking results with 0.25% output coupling and six pump diodes. (a) Slope efficiency. (b) RF spectrum. (c) Optical spectrum. (d) Autocorrelation trace.

The pulse width of 50 fs obtained in this study appears to be limited by the cavity dispersion since the SAM bandwidth should support pulse widths of ~25 fs [12]. In the future, the use of oxidized broadband SAM [67], may enable the generation of pulses as short as 10-fs, or broadly tunable sub-100-fs pulses from ~800 nm to ~1000 nm. Moreover, improvements in diode output powers are expected to enable peak power scaling of these GHz lasers to the ~10 kW level. The heat sinking of the SBR can be improved by reducing the GaAs substrate thickness of the SBR (~220 um), such that only water-cooling near room temperature, or even passive cooling, should be adequate.

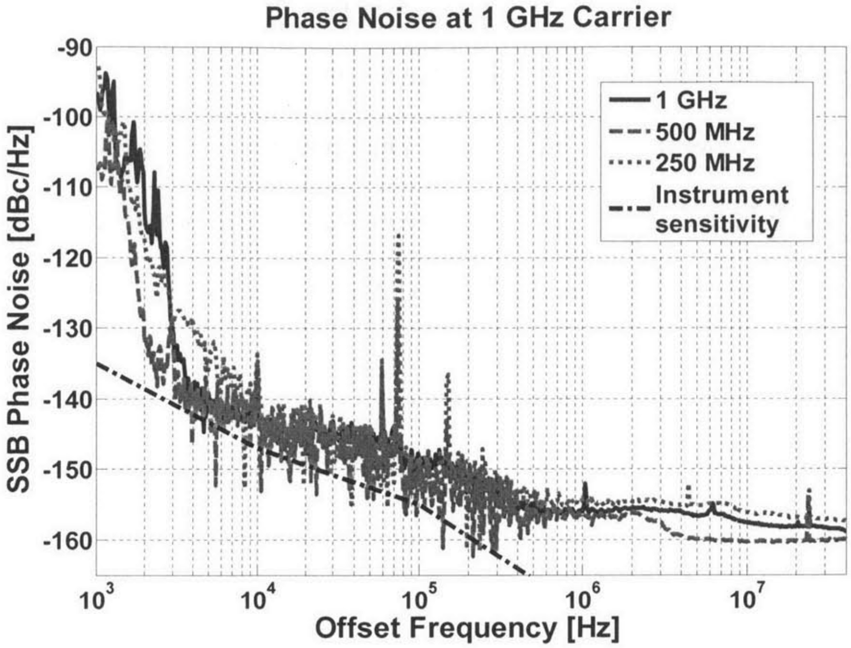

Figure 2.10. SSB phase noise of 250-MHz, 500-MHz and 1-GHz Cr:LiSAF lasers.

In addition to the laser parameters discussed above, timing jitter of the pulse repetition rate is of particular interest. This can be measured with a signal source analyzer (E5052 series from Agilent) which compares the fundamental pulse repetition rate (or its harmonics) detected by a photodetector with the built-in low-noise reference microwave oscillator. Phase noise and timing jitter of 250-MHz, 500-MHz and 1-GHz Cr:LiSAF lasers are characterized in this way. Laser parameters of the three lasers are close to those listed in Table 2.1. In each measurement, the pulse train is detected by a battery-powered biased Si detector (SV2-FC, Thorlabs), filtered by a 1-GHz bandpass filter, and amplified by a low noise amplifier (AM-3A-000110, MITEQ). The carrier power at 1 GHz detected by the signal source analyzer is ~10 dBm. The single-sideband (SSB) phase noise traces, all measured at 1 GHz carrier frequency, are plotted in Figure 2.10. Each trace is a result of 16 correlations of consecutive measurements.

It can be seen that phase noise beyond 10 kHz and 200 kHz are very close to the noise floor of the signal source analyzer. And the phase noise beyond 200 kHz is limited by the amount of microwave power into the instrument. The integrated timing jitter from 1 kHz to 40 MHz is ~70 fs, which is mainly limited by the precision of the internal reference microwave oscillator and the phase detection sensitivity of the Agilent instrument.

# Chapter 3

# Timing Jitter of Saturable Absorber Modelocked Cr:LiSAF Lasers

## 3.1 Motivation

The timing jitter measurements described in Chapter 2 suggest that the commercial signal source analyzer cannot characterize the phase noise of the modelocked Cr:LiSAF lasers beyond a few kHz offset frequency. The integrated timing jitter value mostly stems from phase noise of the internal reference microwave oscillator and measurement sensitivity of the instrument. Comparison of the increase rate of timing jitter variance from microwave oscillator signals and modelocked laser pulse trains reveal that the ultrashort pulse duration of femtosecond lasers offers an unrivaled advantage [68]. Using analytical soliton perturbation theory [69] and numerical techniques [70, 71] to study noise properties of modelocked lasers predicts that the timing jitter of typical modelocked solid-state lasers can easily reach the attosecond regime.

With an improved phase noise measurement sensitivity, balanced optical cross-correlation (BOC) measurement techniques [72] provide a direct optical domain method to measure timing jitter with high sensitivity and sufficient temporal detection range. This method has measured timing jitter up to the Nyquist frequency in passively modelocked fiber lasers [73, 74] and solid-state lasers [75, 76]. The measurement found that stretched-pulse fiber lasers operating at close-to-zero intracavity dispersion exhibit sub-100-as quantum-limited timing jitter [77], and pulse dynamics and different modelocked regimes influence the phase noise [78, 79]. The lowest timing jitter reported to date is 13 as from Kerr-Lens Mode-locked (KLM) Ti:sapphire lasers [76]. In passively modelocked solid-state lasers, however, excess phase noise due to AM-to-PM conversion has been observed in both Ti:sapphire and Cr:LiSAF lasers.

It is therefore important to investigate the AM-to-PM mechanisms and to understand the impact of the modelocking regimes on noise properties of ultrafast solid-state lasers. In particular, it is unclear whether temporal shifts of the pulses due to asymmetric pulse shaping by a slow saturable absorber significantly contribute to timing jitter. It has not been experimentally investigated if the operating point of the saturable absorber is critical with respect to timing jitter of optical pulse trains. Moreover, it is desirable to know to what extent the current timing jitter measurement on ultrafast solid-state lasers could be further improved, given that modelocked fiber lasers have already reached the quantum limit at the sub-100-as level.

## 3.2 Quantum-Limited Timing Jitter

The sources of modelocked laser timing jitter have been previously studied and summarized in Haus and Mecozzi's seminal paper [69]. Numerical simulations [70, 71] confirm the

Haus/Mecozzi analytical model and generalizes it to pulse shapes other than the $\mathrm{sech}^2$ shape. In the case of a semiconductor saturable absorber modelocked solid-state laser, the saturable absorber plays an important role on timing jitter of optical pulse trains. A slow saturable absorber shapes pulses asymmetrically and therefore shifts the pulse center in every round-trip [80]. The saturable absorber's relatively narrow bandwidth limits the pulse's spectral width, limiting eventual Gordon-Haus jitter [81]. Consequently, the timing shift per round-trip $\Delta t$ is described by the following equation of motion derived with soliton perturbation theory [69],

$$T_{\mathrm{rt}} \frac{\partial}{\partial T} \Delta t = -2|D|\Delta p + T_{\mathrm{rt}} S_{\mathrm{t}}(T) \tag{3.1}$$

where $T_{\mathrm{rt}}$ is the round-trip time and equals $f_{\mathrm{r}}^{-1}$ for fundamentally modelocked lasers. $T$ is time on the order of many round-trips, $D$ the intracavity dispersion, $\Delta p$ the center frequency shift per round-trip, and $S_{\mathrm{t}}(T)$ the direct noise source of timing fluctuation. The back coupling of continuum to solitary pulses is neglected. Moreover, it is assumed that the intracavity pulses are transform-limited, which is true for solitary pulses from saturable absorber modelocked Cr:LiSAF lasers.

Quantum-limited timing jitter assumes amplified spontaneous emission (ASE) as the sole noise source, which is approximately white noise with power per Hz $P_{\mathrm{ASE}} = n_{\mathrm{sp}}(2g)(hv)/T_{\mathrm{R}}$, where $n_{\mathrm{sp}}$ is the excess noise factor, $g$ the incremental field amplitude gain per round-trip, and $hv$ the photon energy. The ASE directly induces $(2\pi f)^{-2}$-form random walk of pulses, resulting in the phase noise [69]

$$\begin{aligned}\mathcal{L}(f) &= \frac{1}{2}\left(2\pi f_{\mathrm{r}}\right)^{2}\frac{1}{\left(2\pi f\right)^{2}}\left(\frac{\pi^{2}\tau^{2}}{6w}P_{\mathrm{ASE}}\right) \\ &= \left(2\pi f_{\mathrm{r}}\right)^{2}\frac{1}{12}\frac{f_{\mathrm{r}}}{f^{2}}g\frac{\tau^{2}}{N_{0}}n_{\mathrm{sp}}\end{aligned} \tag{3.2}$$

where $w$ is the intracavity pulse energy, $\tau = \tau_0 / 1.76$ with $\tau_0$ being the FWHM intracavity pulse duration, and $N_0 = w / h\nu$ the intracavity photon number.

In addition, the ASE-induced center frequency fluctuation $\Delta p$ also affects timing jitter according to Equation (3.1). This is a major factor when the optical spectral width of the pulse only fills part of the gain bandwidth. Such frequency fluctuations couple to timing error and are damped with relaxation time $\tau_{\mathrm{p}} = 3T_{\mathrm{rt}}\Omega_{\mathrm{g}}^{2}\tau^{2} / 4g$, leading to the phase noise [69]

$$\begin{aligned}\mathcal{L}(f) &= \frac{1}{2}\left(2\pi f_{\mathrm{r}}\right)^{2}\frac{4\left|D\right|^{2}}{T_{\mathrm{rt}}^{2}}\frac{1}{\left(2\pi f\right)^{2}\left[\left(2\pi f\right)^{2}+\tau_{\mathrm{p}}^{-2}\right]}\left(\frac{2}{3w\tau^{2}}P_{\mathrm{ASE}}\right) \\ &= \left(2\pi f_{\mathrm{r}}\right)^{2}\frac{3}{\pi^{2}}\left(\frac{f_{\mathrm{r}}^{3}\Omega_{g}^{4}}{\left(2g\right)^{2}f_{\mathrm{r}}^{2}+\left(3\pi\right)^{2}f^{2}\Omega_{\mathrm{g}}^{4}\tau^{4}}\right)\left|D\right|^{2}\frac{g}{f^{2}}\frac{\tau^{2}}{N_{0}}n_{\mathrm{sp}}\end{aligned} \tag{3.3}$$

where $\Omega_{\mathrm{g}}$ is the half-width-at-half-maximum (HWHM) gain bandwidth or cavity bandwidth, whichever is smaller. In the case of our Cr:LiSAF laser, the cavity bandwidth is limited by the saturable absorber, which supports femtosecond modelocking with pulse center wavelengths from ~840 nm to ~870 nm [82], whereas a 100-fs pulse corresponds to only ~8 nm bandwidth.

Moreover, shot noise of the pulse train indicates pulse position fluctuations, which leads to a white noise floor [71]

$$\mathcal{L}(f) = \left(2\pi f_{\mathrm{r}}\right)^{2} 0.82\frac{1}{f_{\mathrm{r}}}\frac{\tau^{2}}{N_{0}} \tag{3.4}$$

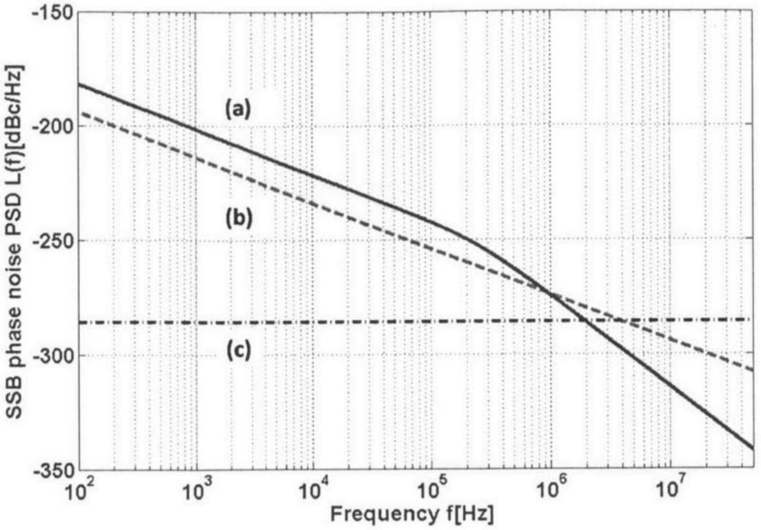

Figure 3.1. Quantum-limited SSB phase noise at 100-MHz carrier frequency. (a) Gordon-Haus jitter with HWHM gain bandwidth of ~25 THz. (b) Phase noise only due to direct phase noise from ASE. (c) Phase noise due to shot noise. Other parameters used: $n_{sp}=1$, intracavity power = 6 W, 2g = 0.03, D = -100 $fs^2$ and pulse width = 80 fs.

The dependence on $\tau^2/N_0$ of the results above clearly show that both short intracavity pulse duration and high intracavity photon number are important in order to achieve low timing jitter. Figure 3.1 illustrates the different contributions to quantum-limited timing jitter for a typical 100-MHz Cr:LiSAF laser. The Gordon-Haus jitter dominates for frequencies below ~1 MHz, and the relaxation time $\tau_p \approx 670$ ns leads to a corner frequency at ~237 kHz. At high frequencies, the shot-noise limited phase noise becomes dominant. This also implies that a measurement sensitivity better than -280 dBc/Hz at 100-MHz carrier is required to fully characterize the quantum-limited timing noise. The corresponding timing jitter integrated from 10 kHz to 50 MHz is only ~2 as.

## 3.3 Attosecond Timing Jitter Characterization

Phase noise and timing jitter of saturable absorber modelocked femtosecond Cr:LiSAF lasers are measured with the balanced optical cross-correlation technique. Timing of the optical pulse trains from two identically constructed Cr:LiSAF lasers are compared in the optical domain, with the help of a highly phase-sensitive single-crystal BOC, which yields phase noise and timing jitter with equal contribution from the two optical oscillators. This is analogues to the two-oscillator technique, which is used to measure reference and test oscillators of the same type [83].

### 3.3.1 Single-Crystal Balanced Optical Cross-Correlation

The single-crystal BOC utilizes the same nonlinear crystal to generate cross-correlation signals and to introduce a delay between the forward and backward passes. As shown in Figure 3.2 (a), the orthogonally linearly-polarized collinear beams of two lasers are the fundamental fields that generate a third sum-frequency field, which has the same polarization as the fast propagating fundamental field in the Beta Barium Borate (BBO) crystal, cut for type-II sum-frequency generation (SFG) process. In a forward or backward single-pass, a SFG signal is generated and the intensity is related to the temporal and spatial overlap of two fundamental pulses. The signal of both passes is detected by the photodiodes in an amplified balanced detector that outputs voltage difference of its two channels.

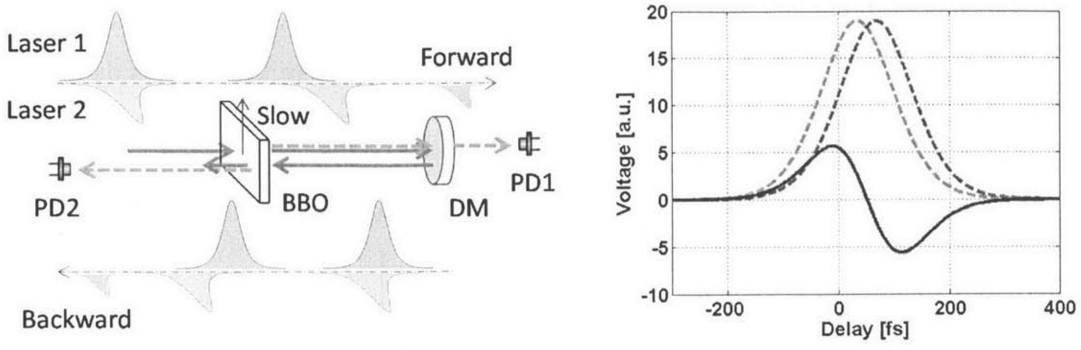

(a) (b)

Figure 3.2. Single-crystal balanced optical cross-correlation. (a) Illustration of the working principle. (b) Calculated cross-correlation traces for 100fs pulses and a 400-μm thick type-II BBO crystal, in which the green trace is for the forward pass, red for the backward, and the blue for the difference. DM, dichronic mirror; PD1, PD2, the two photodetectors in a balanced photodetector.

As derived in Appendix A, the voltage output $V_o(\Delta t)$ of the balanced detector is

$$\begin{aligned}
&V_o(\Delta t) = V_f(\Delta t) - V_b(\Delta t) \\
&V_f(\Delta t) = 4\tau G A L^2 I_{10} I_{20} \operatorname{csch}^2\left(\frac{t_1 - t_2 + \Delta t}{\tau}\right)\left[\left(\frac{t_1 - t_2 + \Delta t}{\tau}\right)\coth\left(\frac{t_1 - t_2 + \Delta t}{\tau}\right) - 1\right] \\
&V_b(\Delta t) = 4\tau G A L^2 I_{10} I_{20} \operatorname{csch}^2\left(\frac{2t_1 - 2t_2 + \Delta t}{\tau}\right)\left[\left(\frac{2t_1 - 2t_2 + \Delta t}{\tau}\right)\coth\left(\frac{2t_1 - 2t_2 + \Delta t}{\tau}\right) - 1\right]
\end{aligned} \tag{3.5}$$

where $A$ is a constant, $G$ the transimpedance gain including the photodetectors' response, $I_{10}$ and $I_{20}$ the peak intensities of the laser pulses, $L$ the BBO crystal thickness, and $t_1 - t_2 = \left(v_{g1,e}^{-1} - v_{g2,o}^{-1}\right)\frac{L}{2}$ with $v_{g1,e}$ and $v_{g2,o}$ the group velocities of two fundamental pulses. Figure 3.2 (b) shows the cross-correlation traces (dashed curves) and their difference for $\tau_0 = 1.76\tau = 100$ fs and $L = 400$ μm.

The linear range around zero crossing of the balanced signal can be used to measure instantaneous timing delay of the fundamental pulse pair. Temporal offset of the input pulse pair at the zero crossing is found by solving $V_\mathrm{o}(\Delta t) = V_\mathrm{f}(\Delta t) - V_\mathrm{b}(\Delta t) = 0$ for $\Delta t$. In the case of Figure 3.2 (b), $\Delta t = 51$ fs for 100-fs pulses. The measurement sensitivity $S_\mathrm{BOC}$ is determined by the slope at zero crossing, i.e.

$$S_\mathrm{BOC} = \left| \left| \frac{dV_\mathrm{o}(\Delta t)}{d\Delta t} \right|_{V_\mathrm{f}(\Delta t) = V_\mathrm{b}(\Delta t)} \right| \tag{3.6}$$

In terms of experiment parameters, the measurement sensitivity is determined by pulse duration $\tau_0$ and BBO crystal length $L$, because they define the widths of each cross-correlation trace and relative delay of the forward and backward passes. Their effects on the sensitivity are illustrated in Figure 3.3, where the sensitivity is plotted normalized to $4GAL^2 I_{10} I_{20}$. It should be noted that Equations (3.5) and (3.6) only consider the temporal overlap of the input pulses. In fact, spatial overlap is also important to maximize measurement sensitivity. The spatial analysis, however, would be more complex and can be modeled in the SNLO software [84], which is able to model diffraction and birefringent walk-off in addition to group velocity walk-off.

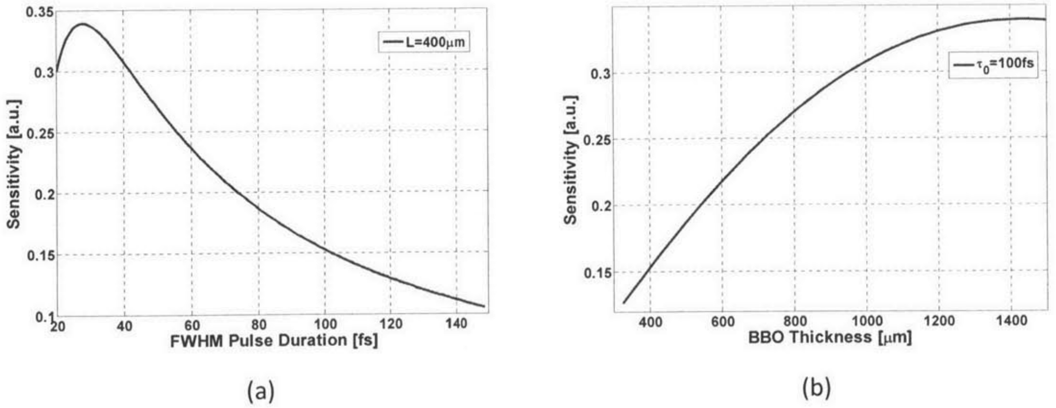

Figure 3.3. BOC measurement sensitivity. (a) As a function of pulse duration, for a 400-μm thick BBO crystal. (b) As a function of crystal thickness, for 100-fs pulses.

It can be seen from Figure 3.3 that the group delay from a BBO crystal of few hundred micrometer thickness is sub-optimal to achieve the maximum sensitivity. A remedy is to insert a piece of dispersive material to complement the additional delay. In terms of spatial overlap, birefringent walk-off is a limiting factor when tight focusing is preferred and the pulses are not well overlapped over their existence distance (30 μm for 100 fs pulses in air). For BBO crystal, the walk-off angle at 860 nm is 72 mrad. This means a 2-μm relative transverse shift after propagating 30 μm. In other words, the input beam waist should be large enough so that such a spatial walk-off is not significant. This leads to an optimum lens focal length $f = \pi w w_0 \lambda^{-1}$, where $w$ is the collimated beam waist before lens, $w_0$ the focused beam waist.

### 3.3.2 Phase Noise Measurement

Two 100-MHz Cr:LiSAF lasers, as illustrated in Figure 3.4, are built for phase noise characterization. Four HL6385DG laser diodes pump the folded four-mirror cavity from both sides. Multiple dispersion compensation mirrors (DCM) are used to generate short pulses, and to fold the cavity arms. Two piezoelectric transducers (PZT) are included to fine tune cavity length. The long-range PZT (P-820.10 from Physik Instrumente, 15 um/100 V), attached to the translation stage under the output coupler (OC), is used to manually change the repetition rate. The short-range PZT (PSt 150/7x7/2 from Piezomechanik, 2 um/150 V) has a fast modulation response and is used in synchronizing the repetition rates of two lasers with a phase locked loop (PLL). In order to alleviate ringing, the short-range PZT is mounted on a hollow copper holder filled with lead to dampen possible vibration modes [85]. The total round-trip cavity length of each laser is 3m, around which a 15-μm length change corresponds to 1 kHz of repetition rate change. Each laser outputs ~100 fs pulses centered around 860 nm with ~1.2 nJ pulse energy. Before the BOC is employed, phase noise of the two lasers is first examined with the signal source analyzer to ensure that the lasers are operating in a stable modelocking state.

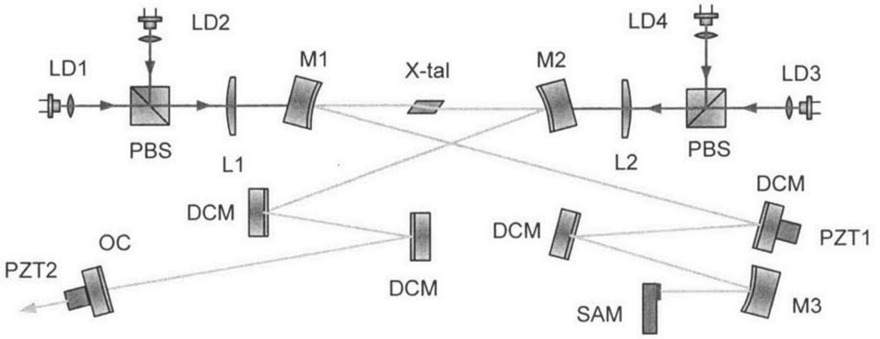
LD2
LD4
LD1
M1
X-tal
M2
LD3
PBS
L1
L2
PBS
DCM
DCM
DCM
PZT1
OC
PZT2
DCM
SAM
M3

Figure 3.4. Schematic of the 100-MHz Cr:LiSAF lasers for phase noise characterization. LD1-LD4, HL6385DG laser diodes; L1, L2, 65-mm focal length aspheric doublet; M1, M2, 75-mm ROC DCM mirrors; PBS, polarizing beam splitting cube; DCM, flat dispersion compensation mirrors; SAM, 850-nm semiconductor saturable absorber; PZT1, short-range piezoelectric transducer; PZT2, long-range piezoelectric transducer; X-tal, Cr:LiSAF crystal; OC, ~2% output coupler.

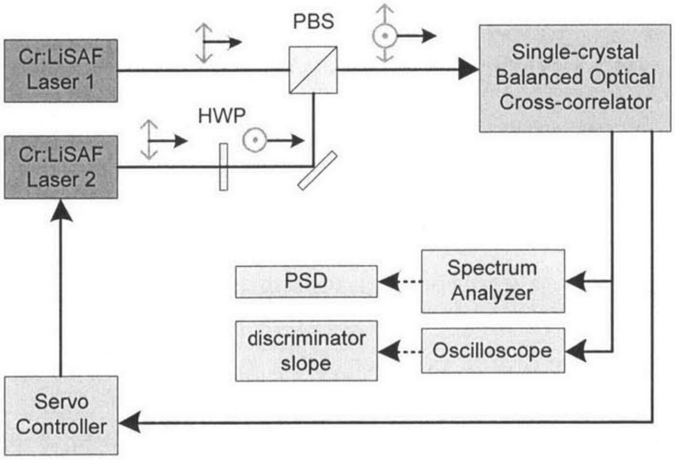
Cr:LiSAF Laser 1
PBS
Single-crystal Balanced Optical Cross-correlator
HWP
Cr:LiSAF Laser 2
PSD
Spectrum Analyzer
discriminator slope
Oscilloscope
Servo Controller

Figure 3.5. Schematic of the phase noise measurement system. PBS, polarizing beam splitting cube; HWP, half-wave plate.

The system for timing jitter characterization is shown in Figure 3.5. Laser beams from the two 100-MHz Cr:LiSAF lasers are polarization combined by a polarizing beam splitter

(PBS) cube and sent to the BOC. Output of the BOC are split in parts and used to synchronize the two lasers for calibrating the phase discriminator slope, and measuring phase noise, respectively.

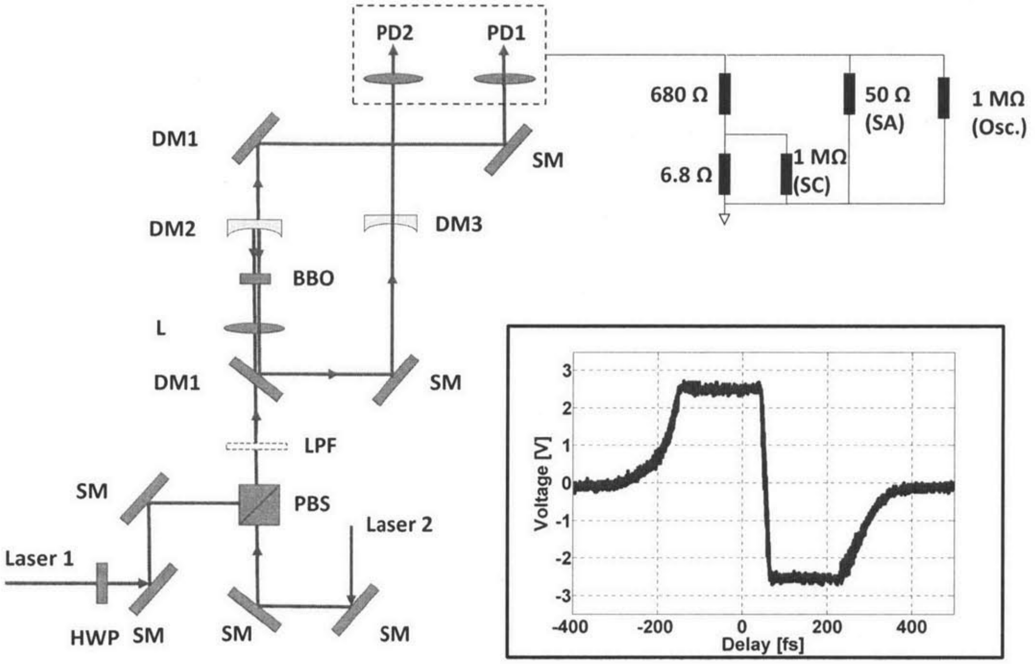

Figure 3.6. Schematic of the single-crystal BOC. Inset, balanced cross-correlation signal with a slope of 240 mV/fs. HWP, half-wave plate; SM, silver mirror; PBS, polarizing beam splitting cube; LPF, 800-nm long pass optical filter; DM1, dichronic mirror with 800-nm anti-reflection (AR) and 400-nm high-reflection (HR) coating; L, uncoated lens with 48-mm focal length; BBO, 400-µm type-II cut; DM2, 60-mm ROC dichronic mirror with 800-nm HR and 400-nm AR coatings; DM3, 100-mm ROC dichronic mirror with the same coatings as DM2; PD1, PD2, photodetectors of the balanced detector; SC, servo controller; SA, spectrum analyzer; Osc., oscilloscope.

The single-crystal BOC, sketched in Figure 3.6, is based on a 400-µm BBO crystal cut for type-II phase matching at 830 nm. The forward and backward SFG signal intensity is related to the temporal and spatial overlap of the two fundamental pulses. The signal from both passes is detected in an amplified balanced detector. To achieve low noise, high gain and large bandwidth, a Thorlabs PDB120A fixed-gain balanced detector was modified for this experiment with two Hamamatsu S5712 photodiodes and a trans-impedance gain of 36 kΩ up to ~20 MHz bandwidth; the noise floor is as low as ~1 μV/$\sqrt{\text{Hz}}$ [85]. The steering mirrors (DM1) also serve as spectral filters that separate the SFG signal from the fundamental input signal. The output of the balanced detector is split by a voltage divider. The low voltage output is connected to a servo controller (LB1005, New Focus), which drives the PZT in laser 2 and synchronizes the cavity length to that of laser 1. The high voltage output is sent to an RF spectrum analyzer (R3267, Advantest) and an oscilloscope. The measured power contains equal contributions from the two uncorrelated pulse trains. The corresponding voltage PSD is therefore divided by 2, and finally converted to SSB phase noise at 100-MHz carrier frequency using the measured phase error discriminator slope (240 mV/fs).

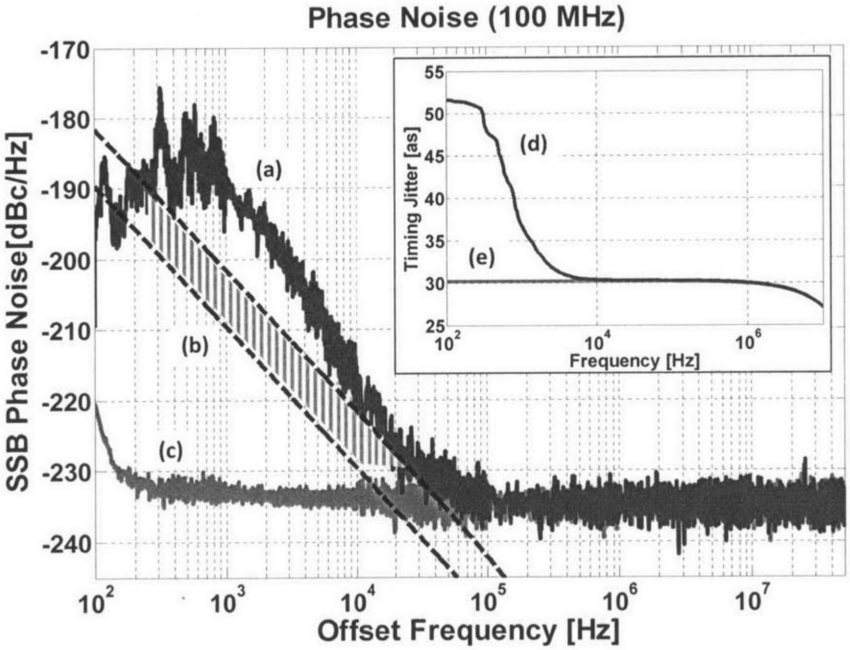

Figure 3.7. SSB phase noise PSD of a single laser at 100-MHz carrier. (a) Measured Cr:LiSAF phase noise (b) A range of quantum-limited phase noise estimation. (c) Balanced detector's noise floor. Inset: integrated timing jitter from 50 MHz (d) Cr:LiSAF (e) Balanced detector's noise floor.

Figure 3.7 summarizes timing jitter measurement expressed as SSB phase noise at 100-MHz carrier frequency. The low-frequency phase noise is suppressed by the feedback loop.

The detection sensitivity is -235 dBc/Hz, limited by the discriminator slope and the noise floor of the balanced detector. The balanced detector response has a light roll-off above 1 MHz offset frequency in the measured spectra. This is compensated in data processing, and cannot be seen in Figure 3.7. The integrated timing jitter from 10 kHz to 50 MHz (the Nyquist frequency) is 30 as, and mostly results from the detection noise floor, which is already reached beyond 100 kHz.

The measurement accuracy is determined by that of the RF spectrum analyzer and the discriminator slope. Most spectrum analyzers measure power within a certain resolution bandwidth (RBW), and the PSD is derived using $\mathrm{dBm/Hz} = \mathrm{dBm} - 10 \times \log_{10}\left(\alpha \cdot \overline{RBW}\right)$, where $\alpha$ is a factor that corrects for system error and filter shape. $\alpha$ can be determined using the built-in noise measurement function of the instrument, which displays a calibrated noise PSD within a given frequency range. The system error of PSD measurements in this experiment is ~1 dB. In addition, the relative error of sensitivity (mV/fs) is experimentally determined to be less than 20%. In total, the above system errors result in an uncertainty $< \pm 10$ as.

## 3.4 Intensity Noise and Timing Jitter

The measured phase noise shown in Figure 3.7 deviates from its quantum-limited prediction. This implies the existence of excess technical noise, possibly from the limited common-mode-rejection-ration (CMRR) and the intensity noise coupling to timing jitter.

### 3.4.1 AM-to-PM Conversion

In contrast to a conventional two-oscillator phase noise measurement using direct photodetection, the BOC method is immune to AM-to-PM conversion in the photo detection process. The excess phase noise usually originates from amplitude fluctuations of the input signal [86]. This is true in the BOC method, because that both timing error and intensity fluctuation of input pulses result in a change of SFG intensity, which cannot be differentiated by either photodiode in the balanced detector. The CMRR becomes a crucial factor, which is defined as the ratio of differential-mode gain and common-mode gain. Intensity noise is suppressed by strong common-mode rejection of the balanced detector. Although both timing error and intensity fluctuations of input pulses result in a change of SFG intensity, the intensity fluctuations in forward and backward passes are identical and therefore are eliminated in the differential output. Ideally, this assumes an infinite CMRR and balanced optical power on both photodiodes. Real CMRR is both finite and frequency-dependent.

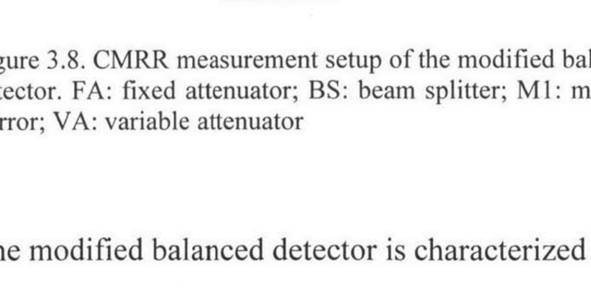

Figure 3.8. CMRR measurement setup of the modified balanced detector. FA: fixed attenuator; BS: beam splitter; M1: metallic mirror; VA: variable attenuator

The CMRR of the modified balanced detector is characterized with the setup shown in Figure 3.8. A 660-nm HL6545MG laser diode is driven by a low-noise diode driver (ILX-3620, ILX Lightwave) with 1-MHz modulation bandwidth. A fixed attenuator controls the input optical power on the photodiodes. The attenuated beam is then split into two paths, in one of which a continuously variable attenuator is used to balance the two channels or to introduce certain mismatch. The network analyzer (E4395A, Agilent) coherently measures the response of either an individual photodiode or the balanced output at various modulation frequencies. The laser diode is modulated from 100 Hz to 1 MHz with the driver's internal modulation circuit, and from 1 MHz to 10 MHz with a bias-T. The real CMRR is then the difference of the differential-mode gain and common-mode gain in logarithmic scale. The response of the diode driver and laser diode is cancelled out in the subtraction. In any measurement, the network analyzer response is calibrated to a thru.

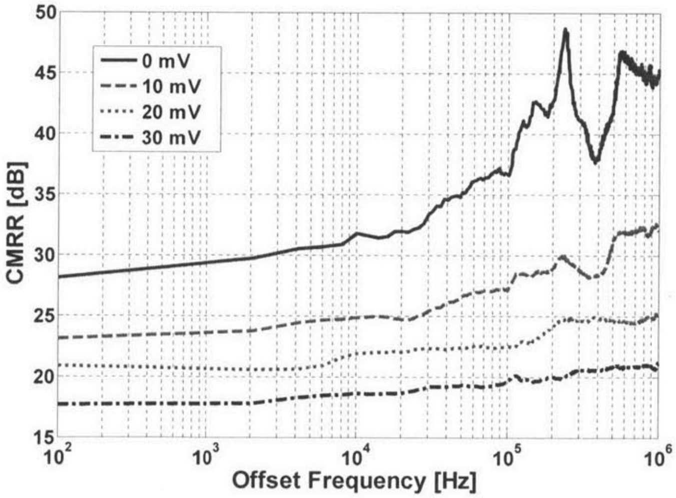

Figure 3.9. CMRR measurements of the modified balanced detector. From top to bottom: balanced, 5%, 10% and 15% mismatch.

The measured frequency-dependent CMRR is shown in Figure 3.9. The maximum CMRR is achieved when the two channels are balanced with each photodetector outputting 200 mV, and the balanced detector's output is -85 mV (the background noise of the modified balanced detector). The balanced signal in the inset of Figure 3.6 also exhibits a similar background noise level of -85 mV, which suggests that the detector is well balanced. With only a 10% mismatch (20 mV out of 200 mV), the CMRR degrades 10-15 dB. This emphasizes the importance to balance the incident power on both photodiodes. In this case, SFG intensity fluctuation due to the intensity noise of the fundamental pulses would dominate the detector's output. In general, power imbalance on the photodetectors results in inconsistent timing jitter phase noise measurements. When balanced, however, the modified balanced detector has a CMRR greater than 28 dB within the frequency range of interest.

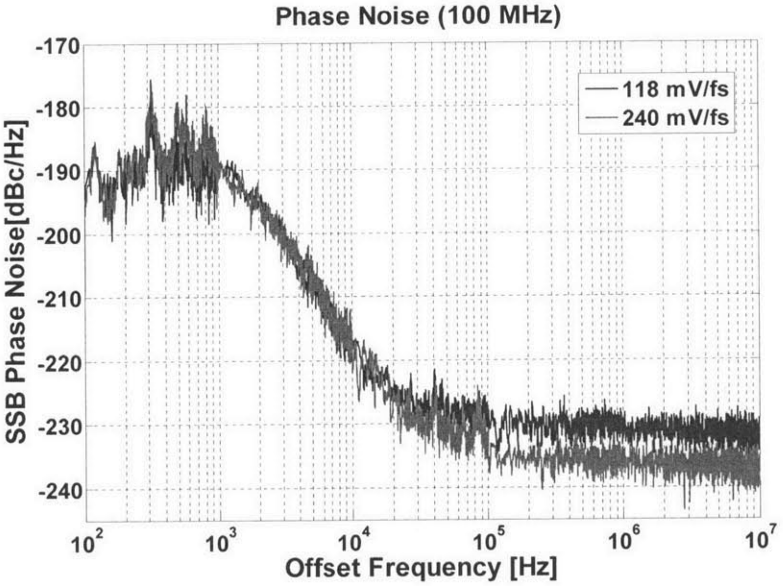

Figure 3.10. Phase noise of two values of phase detection sensitivity. The slight roll-off above 1 MHz is due to the detector frequency response.

The influence of CMRR can be tested by measuring timing noise at different SFG power and measurement sensitivity values. Strength of the common-mode power spectra will certainly change with the absolute SFG power in each channel, and will not scale proportionally as the phase discriminator slope. Figure 3.10 shows phase noise measured with identical experiment settings, the only difference being the phase discriminator slope. In one case, the BBO crystal is intentionally rotated, resulting in less efficient SFG and reduced sensitivity. It is clear that the measured timing phase noise spectral density plots overlap with each other until sensitivity-limited detectable upper frequency limit. Noise floors of the two measurements differ by ~3dB, which agrees with the ratio of the two phase discriminator slopes, 118 mV/fs and 240 mV/fs. This means that reducing the SFG power excludes insufficient CMRR from system error, at least within the currently detectable frequency range.

With a sufficiently large CMRR, the AM-to-PM coupling occurs through the self-steepening effect [87, 88], or pulse reshaping upon saturation on the slow saturable absorber [80], or both. These coupling mechanisms are formulated as follows for fundamentally modelocked lasers. First, the excess SSB phase noise due to the self-steepening effect is [71, 88]

$$\mathcal{L}(f)=\frac{1}{2}\left(\frac{f_{\mathrm{r}}^{2}\varphi_{\mathrm{NL}}}{\pi f \nu}\right)^{2} S_{\mathrm{I}}(f) \tag{3.7}$$

where $\varphi_{\mathrm{NL}}$ is the average nonlinear phase per round-trip introduced by the gain medium, $S_{\mathrm{I}}(f)$ intensity noise PSD of modelocked laser, and $\nu$ the center optical frequency. In addition, the AM-to-PM conversion due to the slow saturable absorber is characterized by phase noise [71]

$$\mathcal{L}(f)=\frac{1}{2}\left(\frac{f_{\mathrm{r}}^{2}}{f}\frac{\partial \tilde{t}_{\mathrm{s}}(S)}{\partial S}S\right)^{2} S_{\mathrm{I}}(f) \tag{3.8}$$

here $S = w / w_{\mathrm{sat,A}}$ is the saturation parameter, $w_{\mathrm{sat,A}}$ the saturation energy of saturable absorber, and $\tilde{t}_{\mathrm{s}}(S)$ the timing shift per round-trip which is thoroughly discussed in reference [80].

In order to quantify the impacts of the self-steepening effect and the temporal shift on a saturable absorber, it is needed to measure relative intensity noise (RIN) of the modelocked laser, and the saturation parameter.

### 3.4.2 Relative Intensity Noise

RIN of the pump laser diodes and the modelocked Cr:LiSAF laser are measured at baseband. This avoids technical difficulties of measuring intensity noise at carrier or harmonic frequencies [89]. Instead of a transimpedance amplifier, a 50-Ω resistor is used as the front-end. This has the advantage of simplicity and large bandwidth, though precautions must be paid to achieve reliable measurements. The photocurrent $i_\mathrm{p}$ has to be more than 1 mA, so that shot noise $i_\mathrm{s} = \left(2ei_\mathrm{p}\right)^{1/2}$ surpasses Johnson-Nyquist noise $i_\mathrm{j} = 2\left(kTR\right)^{1/2}$ for $R = 50\ \Omega$ at $T = 300$ K. On the other hand, the photocurrent must not exceed the linearity limit of the photodiode. In any case, localized saturation due to overly tight focusing should always be avoided. This suggests that a large-area photodiode should be used in order to achieve high dynamic range.

In this experiment, a Si photodiode (FFD040, EG&G) is reversely biased by a 22-V battery. The laser beam is loosely focused and fills the whole aperture of the built-in iris of the photodetector. The photocurrent is kept between 1 mA to 2 mA, and terminated by a 50Ω carbon film resistor. The voltage is then amplified by a home-built AC-coupled low-noise voltage amplifier[4] (34.2 dB gain up to 50 MHz bandwidth) and sent to an oscilloscope or spectrum analyzer. For a given laser, multiple measurements at different photocurrents are compared to ensure no localized saturation or nonlinear response of the photodiode. In addition, the shot-noise limited measurement floor is always calculated as a quick check of photocurrent saturation.

---

[4] Built by Andrew J. Benedick.

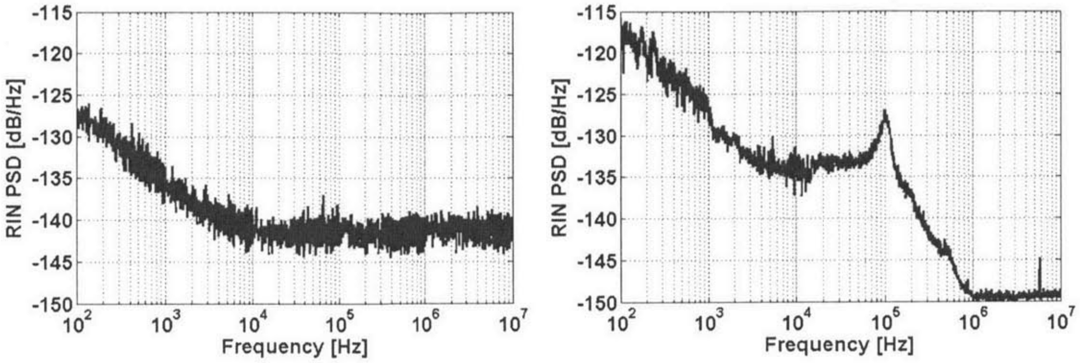

(a) (b)

Figure 3.11. Measured relative intensity noise of (a) HL6385DG laser diode. (b) 100-MHz modelocked Cr:LiSAF laser.

As shown in Figure 3.11(a), the pump laser diode exhibits $f^{-1}$-like frequency-dependent intensity noise up to ~10 kHz, which is typical for Fabry-Pérot cavity quantum-well semiconductor lasers due to material and manufacturing defects [90]. If mode-hopping exists when the laser diode outputs multiple longitudinal modes, the measured RIN shows strong noise peaks, especially at offset frequencies beyond 1 MHz. As the forward current increases from 150 mA to 350 mA, the lasing wavelength shifts 4 nm, shown in Figure 3.12(a). Because our spectrometer cannot resolve each longitudinal mode, RIN is measured at two forward current values. In Figure 3.12(b), a 10-mA increase from 320 mA drives the laser diode working in multiple longitudinal modes, and the spikes are the result of beating among the lasing modes. The mode-hopping noise can be avoided by operating the laser diode at a combination of forward current and case temperature that results in single longitudinal mode lasing, which is verified by a clean RIN PSD.

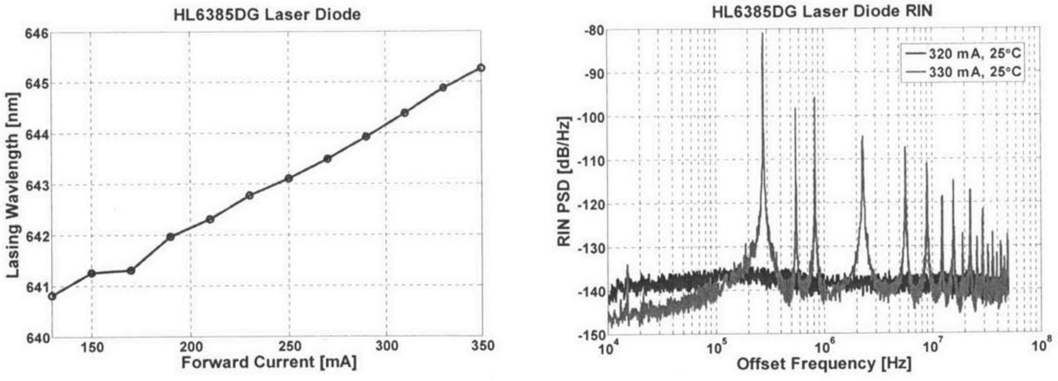

(a) (b)

Figure 3.12. Mode hopping and RIN of the HL6385DG laser diode. (a) Lasing wavelength as a function of the forward current[5]. (b) RIN PSD of the two forward current settings at 25°C.

The modelocked intensity noise of the Cr:LiSAF laser is shown in Figure 3.11 (b). At frequencies below ~10 kHz, a $f^{-1}$-like noise spectrum is observed, due to the corresponding intensity noise of the pump laser diodes. The relaxation oscillation peak is centered around 100 kHz. At high frequencies, the intensity noise rolls off quickly to the shot-noise limited detection floor.

The transfer function that couples pump RIN and timing jitter is experimentally characterized. The network analyzer in Figure 3.13 (a) modulates one of the pump laser diodes, and coherently detects the response of the BOC. The measured transfer function is then applied to the pump RIN PSD. Such calculated timing jitter due to intensity fluctuations is plotted as the dashed curve in Figure 3.13 (b). The solid curve in Figure 3.13 (b) is the same phase noise as shown in Figure 3.7 (a). For frequencies below ~10 kHz, the dashed curve is clipped by the PLL which is closed at a different state than that in the phase noise measurement due to pump modulations induced by the network analyzer; whereas the part beyond ~100 kHz is not real, due to strong filtering of the relaxation oscillation. The rest of the dashed curve closely tracks the measured phase noise PSD. This suggests that the timing jitter of the Cr:LiSAF laser is currently affected by the intensity noise of the diode pump source; that is, the pump RIN is transferred to the RIN of the modelocked laser and then converted into timing jitter.

---

[5] Measured by Jing Wang.

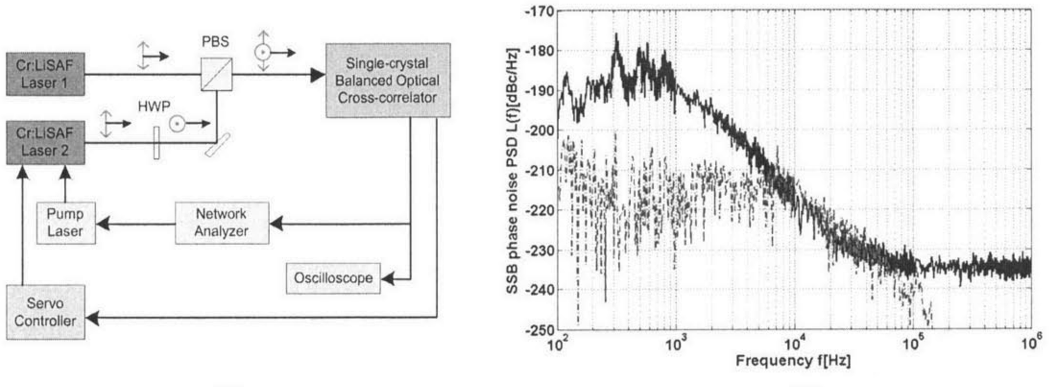

(a) (b)

Figure 3.13. Coupling between RIN and phase noise. (a) Measurement setup. (b) Pump RIN mapped to phase noise (dashed), compared with measured phase noise using BOC (solid, reproduced from curve (a) in Figure 3.7).

### 3.4.3 Saturable Absorber and Timing Jitter

The saturation parameter is one of the key factors to differentiate the above two mechanisms in terms of coupling strength. It can be identified by comparing intensity noise when the laser runs in continuous-wave and modelocked regimes, because the saturable and non-saturable loss in modelocked operation introduces additional cavity loss and therefore alters the laser dynamics [91].

The rate equations for four-level systems give the following coupled differential equations for the dynamics of the intracavity power $P$ and roundtrip amplitude gain $g$.

$$
\begin{aligned}
T_{\mathrm{rt}} \frac{\mathrm{d}P}{\mathrm{d}t} &= 2\left[g - l - q(P)\right]P \\
T_{\mathrm{rt}} \frac{\mathrm{d}g}{\mathrm{d}t} &= -\frac{g - g_0}{\tau_{\mathrm{L}} / T_{\mathrm{rt}}} - g\frac{P}{P_{\mathrm{sat,L}}}
\end{aligned}
\tag{3.9}
$$

where $\tau_{\mathrm{L}}$ is the upper-state lifetime of Cr:LiSAF, $l$ the loss, $P_{\mathrm{sat,L}}$ the gain saturation power, and $q(P)$ the saturable absorber's power-dependent loss. The small signal gain $g_0$ is related to pump power $P_{\mathrm{p}}$ by

$$
g_0 = \tau_{\mathrm{L}} \eta_{\mathrm{L}} \eta_{\mathrm{P}} \frac{P_{\mathrm{P}}}{w_{\mathrm{sat,L}}}
\tag{3.10}
$$

where $\eta_{\mathrm{L}}$ is the quantum efficiency, $\eta_{\mathrm{p}}$ the pump efficiency and $w_{\mathrm{sat,L}}$ the gain saturation energy. Equation (3.10) explicitly includes pump intensity in the rate equations. Rewriting the intracavity power, gain and pump power in terms of steady-state values, denoted by subscript $s$, and small perturbations, the dynamic equations for intracavity power and gain fluctuations are

$$
\begin{aligned}
\frac{\mathrm{d}\Delta P}{\mathrm{d}t} &= \frac{2P_{\mathrm{s}}}{T_{\mathrm{rt}}}\Delta g - \frac{2P_{\mathrm{s}}}{T_{\mathrm{rt}}}\frac{\mathrm{d}q(P)}{\mathrm{d}P_{\mathrm{s}}}\Delta P \\
\frac{\mathrm{d}\Delta g}{\mathrm{d}t} &= -\frac{1}{\tau_{\mathrm{stim}}}\Delta g - \frac{g_{\mathrm{s}}}{w_{\mathrm{sat,L}}}\Delta P + \frac{\eta_{\mathrm{p}}\eta_{\mathrm{L}}}{w_{\mathrm{sat,L}}}\Delta P_{\mathrm{P}}
\end{aligned}
\tag{3.11}
$$

where $\tau_{\mathrm{stim}}$ is the stimulated lifetime. By applying the Laplace transform to Equation (3.11), the following transfer function describes the fluctuations of the modelocked laser's average power $\widetilde{\Delta P}$ as a result of pump power variation $\widetilde{\Delta P_{\mathrm{p}}}$

$$\frac{\widetilde{\Delta P}}{\widetilde{\Delta P_\mathrm{P}}}=\frac{2\dfrac{r-1}{T_\mathrm{rt}}\dfrac{\eta_\mathrm{p}\eta_\mathrm{L}}{\tau_\mathrm{L}}}{s^2+\left(\dfrac{1}{\tau_\mathrm{stim}}+\dfrac{2P_\mathrm{s}}{T_\mathrm{rt}}\dfrac{\mathrm{d}q(P)}{\mathrm{d}P_\mathrm{s}}\right)s+\dfrac{2(r-1)}{T_\mathrm{rt}}\dfrac{l+q_\mathrm{s}}{\tau_\mathrm{L}}+\dfrac{2P_\mathrm{s}}{T_\mathrm{rt}}\dfrac{\mathrm{d}q(P)}{\mathrm{d}P_\mathrm{s}}\dfrac{1}{\tau_\mathrm{stim}}} \tag{3.12}$$

where $r=1+P_\mathrm{s}/P_\mathrm{sat,L}$ is the pump parameter. In the case of continuous-wave lasing, Equation (3.12) is reduced to

$$\frac{\widetilde{\Delta P}}{\widetilde{\Delta P_\mathrm{P}}}=\frac{2\dfrac{r-1}{T_\mathrm{rt}}\dfrac{\eta_\mathrm{p}\eta_\mathrm{L}}{\tau_\mathrm{L}}}{s^2+\dfrac{1}{\tau_\mathrm{stim}}s+\dfrac{2(r-1)}{T_\mathrm{rt}}\dfrac{l+q_\mathrm{s}}{\tau_\mathrm{L}}} \tag{3.13}$$

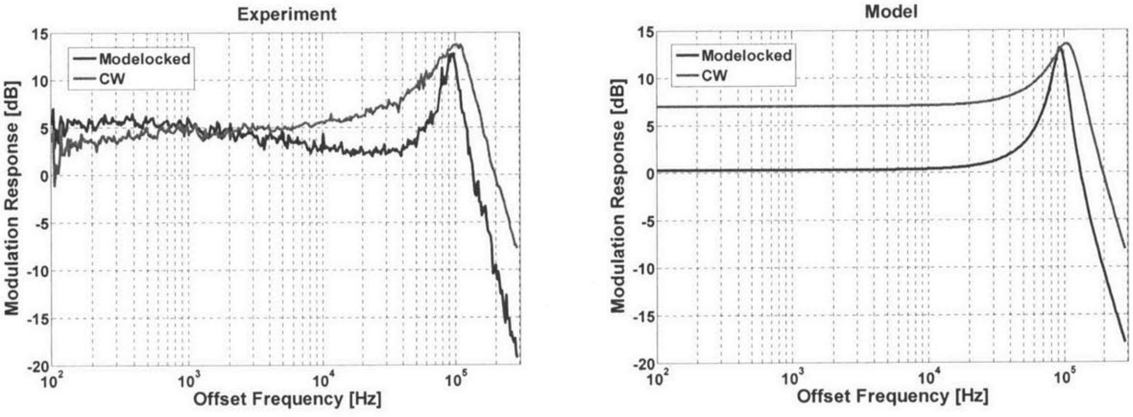

(a)

(b)

Figure 3.14. Transfer functions (magnitude) from pump RIN to Cr:LiSAF laser RIN. (a) Measured transfer functions. ML: modelocked, cw: continouse-wave (b) Modeled responses using Equations (3.12) and (3.13).

The transfer functions described in Equations (3.12) and (3.13) are experimentally measured using a network analyzer. The pump laser diode driving current is modulated from 100 Hz to 300 kHz, and the responses of both pump laser intensity and Cr:LiSAF laser intensity are coherently detected. Figure 3.14 (a) indicates that when the laser is modelocked, the saturable absorber's power-dependent loss $q(P)$, as well as its non-saturable loss $q_0$ included in loss $l$, changes the relaxation oscillation peak's height and width significantly. In order to quantify such a variation, the curves are fitted to the results obtained from Equations (3.12) and (3.13), which are plotted in Figure 3.14 (b). Although the model is incapable of predicting the full spectral shape, it effectively describes the relaxation oscillation behavior around 100 kHz.

To match the measured transfer function to equation (3.12), the parameter

$$\frac{2P_{\mathrm{s}}}{T_{\mathrm{rt}}}\frac{\mathrm{d}q(P)}{\mathrm{d}P_{\mathrm{s}}}=-0.6\frac{1}{\tau_{\mathrm{stim}}} \tag{3.14}$$

is used. Rewriting of equation (3.14) in terms of saturation parameter gives

$$\frac{\mathrm{d}q(S)}{\mathrm{d}S}=-0.6\frac{2rP_{\mathrm{s}}}{\tau_{\mathrm{L}}}\frac{w}{S} \tag{3.15}$$

The saturable absorber used in these studies has both a fast and a slow component in the temporal response [16]. When timing jitter is concerned, only the slow component is considered, because it results in asymmetric pulse shaping and therefore shifts the pulse center. Assuming that the saturable absorber is slow compared with the pulse duration, it fully recovers within the round-trip time, and the saturable loss is simply

$$q(S)=\frac{q_0}{S}\left(1-e^{-S}\right) \tag{3.16}$$

Equations (3.15) and (3.16) are sufficient to solve for $S$. In the case of Figure 3.14(b), $S=9.7$. In addition, the beam waist on the saturable absorber is calculated to be 45 μm using

ABCD-matrix analysis, and the saturation flux of the saturable absorber is estimated to be 130 $\mu J/cm^2$. This is a typical value for the saturable absorbers used in our experiments.

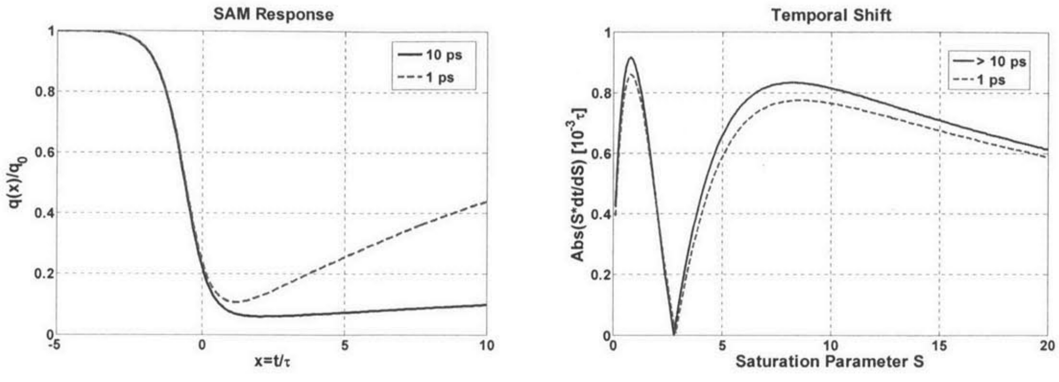

(a) (b)

Figure 3.15. AM-to-PM conversion factors. (a) Response of SAMs with 1-ps and 10-ps recovery times (b) Absolute value of S*dt/dS in units of one thousandth pulse width for 1ps and >10 ps recovery time. Modulation depth of 1% is assumed.

The saturable absorber response and the absolute value of parameter $S \cdot \left[ \partial \tilde{t}_s(S)/\partial S \right]$ in Equation (3.8) are plotted in Figure 3.15. Pulse's temporal shift increases with longer recovery time, but remains virtually constant when recovery time is sufficiently large (100 times longer than pulse duration). The absolute value of $S \cdot \left[ \partial \tilde{t}_s(S)/\partial S \right]$ is maximized at $S = 8.2$. The saturable absorber operating point ($S = 9.7$) in these studies is very close to the peak value. In addition, the parameter becomes zero when $S \approx 3$, at which the timing shift due to the saturable absorber vanishes.

The coupling strengths due to the self-steepening effect and temporal shift of the saturable absorber are both plotted in Figure 3.16. In these plots, 1% modulation depth is assumed. The self-steepening coupling factor is 7.6 dB stronger than that of the slow saturable absorber. In other words, the self-steepening effect dominates when $S \geq 3$ in the case of our modelocked Cr:LiSAF lasers.

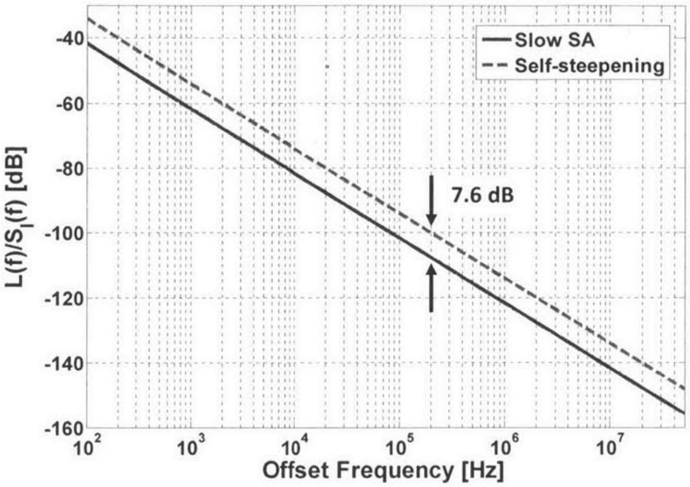

Figure 3.16. Coupling factors due to self-steepening and timing shift on slow saturable absorber (SA) with recovery time longer than 10 ps and S = 8.2.

The magnitude of the temporal shift due to the saturable absorber is sensitive to modulation depth. For a given pulse duration, the peak temporal shift scales linearly with modulation depth, and therefore the coupling factor in Equation (3.8) scales as square of the ratio change. For example, if the modulation depth doubles to 2%, there will be a 6-dB increase in the AM-to-PM coupling strength due to the saturable absorber. In this case, the effects of self-steepening and slow saturable absorption become comparable. However, large modulation depth usually leads to Q-switching instabilities. Our experiments with femtosecond Cr:Colquiriite lasers show that saturable absorbers with modulation depths below 1.5% can start and maintain stable continuous-wave modelocking, whereas modulation depths larger than 2% usually result in q-switched modelocking [12]. This implies that, for femtosecond

Cr:Colquiriite lasers, the contribution of saturable absorption to pulse temporal shift is often negligible as long as the laser is stably modelocked.

# Chapter 4

# Phase Noise of Erbium Silicon Photonic Integrated Oscillators

## 4.1 Motivation

One obstacle to practical application of optical frequency division (OFD)-based microwave oscillators is its large footprint and sensitivity to environmental perturbations. However, the rapid development in silicon photonics [92, 93] and integrated microwave photonics [94, 95] illuminates paths toward a fully-integrated photonic microwave oscillator architecture on a common silicon substrate platform [96]. Performance of key integrated components has been reported to approach or exceed that of the bulk elements typically employed in photonic microwave oscillators. For instance, silicon nitride (SiN) ring resonators with Q-factors of $10^6 \sim 10^7$ at 1550 nm have been reported recently [97-99]. The temperature sensitivity of silicon-based resonators can be reduced by a factor of $10^3$, if thermal-optic coefficients of the core and cladding materials are closely compensated [100, 101], showing that high-Q and thermal-insensitive microresonators may become on-chip optical frequency reference. In addition, initial results in integrated erbium-doped aluminum oxide ($Al_2O_3:Er^{3+}$) lasers with SiN waveguide cavities have shown continuous-wave (cw) lasing with 75-mW power and a slope efficiency of 7% [102, 103], and a linewidth of 501 kHz [104]. When actively stabilized to an integrated reference cavity by a high-bandwidth integrated optical phase-locked loop [105, 106], such type of $Al_2O_3:Er^{3+}$ lasers can serve as ultrastable cw lasers which are critical to reducing close-to-carrier phase noise of photonically generated microwaves. Moreover, integrated modelocked lasers with Er-doped silica waveguides have already been demonstrated. Dispersion engineering in SiN waveguides has also been reported [107]. As an example, femtosecond pulses are achieved with repetition rates of up to 10-GHz [47], which is a desired microwave carrier frequency. Research progress in other important areas also suggests component-level feasibility, including high-bandwidth silicon modulators [108-110], and fast and efficient germanium photodetectors with ~nA dark currents [111-113]. The most important wafer-scale three-dimensional integration technology [96, 114, 115] enables integrated photonic and electronic circuit fabrication, taking advantage of state-of-the-art complementary metal-oxide-semiconductor (CMOS) integrated processes.

While robust and manufacturable systems are highly desired, a number of challenges arise from current limitations of on-chip devices. One of them is the difficulty of implementing $f_{\text{CEO}}$ stabilization with the standard $f-2f$ interferometer [116]. Although supercontinuum generation [117] and second harmonic generation [118] in silicon photonics are implemented, integrated $f_{\text{CEO}}$ control schemes are not reported yet. It is unclear whether OFD is effective without $f_{\text{CEO}}$ stabilization. Experiments on ytterbium-erbium (Yb-Er) co-doped fiber lasers [26], as well as our experiments on Er-doped fiber lasers show that phase-locking a comb line of free-running modelocked lasers to a stable cw laser does not necessarily reduce timing jitter within the locking bandwidths, even though cavity length is modulated as the feedback control mechanism. This phenomenon cannot be explained by the elastic tape model with fixed points, and is attributed to frequency comb dynamics [27] and coupling among different modulation mechanisms [28, 29], which depends on individual laser cavity layout. Given that the conventional $f_{\mathrm{CEO}}$ stabilization scheme is not yet available, it is therefore important to investigate how to control it in order to effectively realize integrated OFD.

In addition, low power level of integrated modelocked lasers increases both quantum-limited timing jitter [69] and photodetection noise. When phase-locked to a reference cavity, a modelocked laser with high intrinsic frequency noise requires large loop gain and bandwidth, which is challenging but achievable on an integrated platform. Without sufficiently large photocurrent $i_{\mathrm{PD}}$, however, phase noise floor is limited by thermal noise, which rapidly increases with $1/i_{\mathrm{PD}}^2$. In order to reach shot-noise-limited phase noise, on-chip power amplification is necessary while energy efficiency needs to be maintained. One solution is to take advantage of power surplus of the ultrastable cw laser, and transfer comb-line frequency stability to cw laser lines with significant power increase compared with that of individual comb lines [119]. Microwaves are then extracted by photodetecting the optical beat between two cw laser lines. Because one comb line is always phase-locked to the ultrastable cw laser for OFD, only one additional optical phase locked loop (OPLL) is required. This microwave extraction scheme facilitates continuous frequency tuning [120] and potentially a ultra-broadband photonic microwave synthesizer. Despite advantages, it requires a voltage-controlled oscillator (VCO) that drives an optical frequency shifter to generate new frequency from the cw laser, if a second cw laser is not employed. In this case, OPLL bandwidth and VCO noise impact phase noise of the generated microwaves. It is essential to understand how various noise sources and OPLL parameters contribute to attainable phase noise at a system level.

## 4.2 Erbium Silicon Photonic Integrated Oscillator

The Erbium Silicon Photonic Integrated OscillatoR (ESPIOR), shown in Figure 4.1, includes a stable cw laser, a femtosecond modelocked laser and a microwave readout stage. The cw laser provides a narrow-linewidth optical single-frequency, which is the ultimate frequency reference of the ESPIOR. The modelocked laser is an optical frequency divider, whose equal-distance frequency comb lines divide the cw laser optical frequency down to microwave regime.

The cw laser in the ESPIOR is a C-band (1530 nm – 1565 nm) erbium-doped waveguide laser. The waveguide structure has a SiN ridge, an $Al_2O_3:Er^{3+}$ film and a $SiO_2$ gap layer in-between [103]. One advantage of such design is the tight confinement and high intensity overlap of the pump and signal modes. The laser resonator consists of a straight waveguide and two distributed Bragg reflectors (DBR). Alternatively, a distributed feedback (DFB) laser resonator can also be used [102]. The laser can be pumped at either 980 nm or 1480 nm. In addition, erbium-ytterbium co-doping can be employed to enhance the absorption at 980 nm and improve signal gain.

Semiconductor laser with the slab-coupled optical waveguide (SCOW) design [121] is a candidate for the on-chip pump laser. In addition to single transverse mode lasing at high power, it has the advantage of low intensity noise, below -155 dBc/Hz at a 2-MHz offset frequency [122]. As discussed in Chapter 3, relative intensity noise of the pump laser transfers to that of the laser being pumped in both cw and modelocked operation; and low-noise pump source is thus critical to reducing phase noise of the ESPIOR.

In order to reduce linewidth, the cw laser is locked to the high-Q SiN microring resonator through the standard Pound-Drever-Hall (PDH) technique [123]. Control of optical frequency of the cw laser is provided by an integrated heater and an intracavity phase modulator. The slow heater corrects long-term cavity length drift, and the fast phase modulator controls high-frequency frequency noise. Frequency modulation required for PDH locking is obtained by an out-of-cavity phase modulator. As an ultrastable reference optical cavity, thermal-optic coefficients of core and cladding materials of the microring are carefully chosen in order to significantly reduce thermal sensitivity of its frequency transmission.

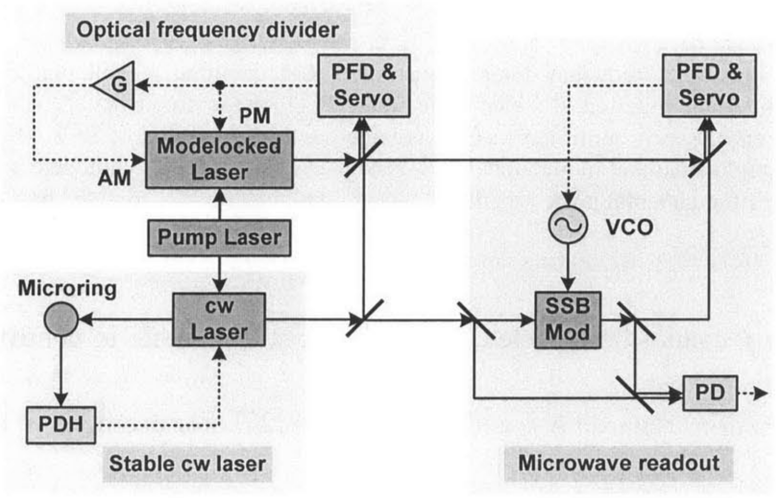
Optical frequency divider
G
PFD & Servo
PM
Modelocked Laser
AM
PFD & Servo
VCO
Pump Laser
Microring
cw Laser
SSB Mod
PD
PDH
Stable cw laser
Microwave readout

Figure 4.1. Integrated photonic microwave oscillator architecture. Solid lines are optical paths, and dashed lines are signal paths.

The modelocked laser has a similar waveguide structure as the cw laser. Modelocking is enabled by a nonlinear optical loop mirror (NOLM) [124] or a semiconductor saturable absorber mirror directly attached to one end facet of the laser waveguide or mounted on top of the waveguide with the help of a vertical coupler. Temperature modulation and pump power modulation can be employed to change the fundamental pulse repetition rate $f_r$ and the carrier-envelop-offset frequency $f_0$, respectively, up to modulation bandwidths below MHz. Faster modulation is made available by intracavity amplitude and phase modulators.

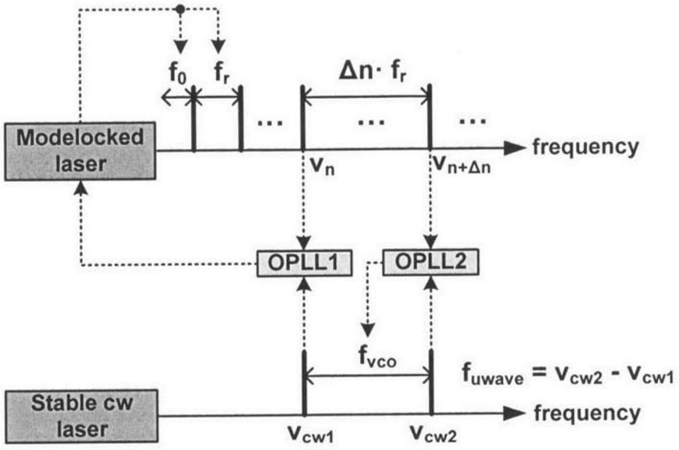

Figure 4.2. Frequency domain illustration. AM, amplitude modulation; PM, phase modulation; $G$, electronic gain; PFD, phase frequency detector; Servo, servo controller; VCO, voltage-controlled oscillator; SSB Mod, single-sideband modulator; PDH, Pound-Drever-Hall; PD, photodetector; $f_r$, fundamental pulse repetition rate; $f_0$, remainder of $f_{CEO}$ divided by $f_r$.

Although $f_0$ cannot be detected on chip, it is still possible to control $f_0$ fluctuation, if noise transfer functions regarding $f_r$ and $f_0$ are known [27]. For example, in Figure 4.2, optical beat notes of one optical comb line frequency $\nu_n$ and the cw laser frequency $\nu_{CW1}$ is detected using a photodetector followed by a digital phase frequency detector. Phase errors are sent to a proportional integral controller (PIC) that simultaneously drives an intracavity phase modulator changing cavity length and $f_r$, and an intracavity amplitude modulator changing cavity loss and $f_0$. The gain block $G$ is configured in such a way that $\Delta f_{0,AM} + \Delta f_{0,PM} = 0$. Ideally, $G$ should have amplitude and phase tailored at each frequency in order to compensate the complex transfer functions linking $\Delta f_0$ and different perturbations. However, experiments have shown that both amplitude and phase of the transfer functions are reasonably flat within their respective bandwidths [28], and therefore $G$ could be a common DC-coupled electronic amplifier with enough gain and bandwidth. In this way, the modelocked laser serves as an optical frequency divider that transfers frequency stability of the cw laser to that of its own comb spacing $f_\mathrm{r}$.

To extract microwaves, a second single-frequency $\nu_\mathrm{cw2}$ is generated by a single-sideband (SSB) phase modulator that shifts $\nu_\mathrm{cw1}$ by a multiple of $f_\mathrm{r}$. The newly generated $\nu_\mathrm{cw2}$ is then locked to the comb line of frequency $\nu_{n+\Delta n}$. When beating $\nu_\mathrm{cw1}$ and $\nu_\mathrm{cw2}$ on a photodetector, microwaves of frequencies $\Delta n \cdot f_\mathrm{r}$ and its harmonics can be extracted. This method is power efficient, in that only power of the two comb lines are amplified instead of average power of the entire optical spectrum. Additionally, because X-band and K-band VCOs are available, GHz microwaves can be extracted from the first harmonic of the photocurrent. This alleviates photodetector saturation, since the repetition-rate multiplication factor $\Delta n$ effectively reduces the harmonic number of photocurrent required to reach beyond a 10 GHz microwave carrier frequency. As a result, the high average power level necessary to reduce phase noise floor is also relaxed. Phase noise of the VCO, however, impacts that of the regenerated microwaves.

## 4.3 Phase Noise of the Integrated Oscillator

### 4.3.1 Noise Model in Phase Domain

A phase-domain noise model is built to investigate phase noise attainable from the photonic integrated oscillator. The ESPIOR system illustrated in Figure 4.2 is translated to the phase noise model diagram in Figure 4.3.

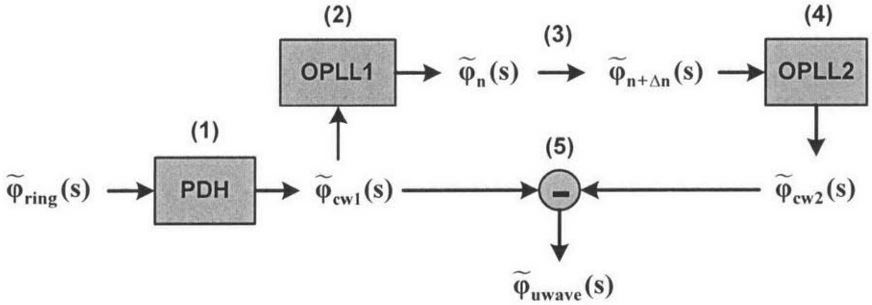

(2)
OPLL1
$\tilde{\varphi}_n(s)$
(3)
$\tilde{\varphi}_{n+\Delta n}(s)$
(4)
OPLL2
(1)
$\tilde{\varphi}_{ring}(s)$
PDH
$\tilde{\varphi}_{cw1}(s)$
(5)
$\tilde{\varphi}_{cw2}(s)$
$\tilde{\varphi}_{uwave}(s)$

Figure 4.3. Phase noise model of the ESPIOR, including five successive steps marked with the numbers (1) to (5). $\tilde{\varphi}_{\mathrm{ring}}(s)$, phase noise of the microring. Other symbols represents phase noise of the quantities in Figure 4.2.

### 4.3.2 Stable Continuous-Wave Laser

Frequency noise of the microring resonator stems from thermal fluctuation which alters optical length of the microring, including the contribution of the effective index change and the physical length change. In terms of length $L_{\mathrm{ring}}$, effective index $n_{\mathrm{eff}}$ and temperature $T$, frequency variation is $\left(\Delta\nu_{\mathrm{ring}}\right)^2=\left(-\frac{\nu_{\mathrm{ring}}}{n_{\mathrm{eff}}L_{\mathrm{ring}}}\frac{d(n_{\mathrm{eff}}L_{\mathrm{ring}})}{dT}\right)^2\left(\Delta T\right)^2$. The $d(n_{\mathrm{eff}}L_{\mathrm{ring}})/dT$ term includes contribution from the thermal-optic coefficient $dn_{\mathrm{eff}}/dT$ and the thermal expansion coefficient $\alpha_{\mathrm{sub}}$ of the substrate material [125]. The temperature variation is estimated as

$(\Delta T)^2 = T^2 4k_B / G$, where $k_B$ is the Boltzmann constant and $G$ the thermal conductance of the substrate material. In terms of single sideband (SSB) phase noise,

$$\mathcal{L}_{\text{ring}}(f) = \frac{1}{f^2} \frac{4k_B T^2}{G} \left( \alpha_{\text{sub}} n_{\text{eff}} + \frac{dn_{\text{eff}}}{n_{\text{eff}} dT} \right)^2 \nu_{\text{ring}}^2 \tag{4.1}$$

In the PDH loop, the microring serves as an optical frequency discriminator. A quantitative model of the frequency detection sensitivity of a Fabry-Pérot cavity has been derived [126], and is directly applicable to the case of a microring. In terms of optical power in the carrier ($P_c$) and one of the sideband ($P_s$), the frequency discriminant is given by $k_{\text{PDH}} = -8\sqrt{P_c P_s}\rho G_{\text{TIA}} / \Delta\nu$, where $\Delta\nu$ is linewidth of the microring, and $\rho$, $G_{\text{TIA}}$ are sensitivity and transimpedance amplifier gain of the photodetector, respectively. The linewidth is sometimes included in the cavity optical quality factor $Q_{\text{ring}} = \nu_{\text{ring}} / \Delta\nu$, or the cavity finesse $F_{\text{ring}} = Q_{\text{ring}} \cdot \overline{FSR} / \nu_{\text{ring}}$, where $\overline{FSR} = c / (2\pi R_{\text{ring}} n_g)$ is the free spectral range, with $R_{\text{ring}}$ being radius of the microring and $n_g$ the group refractive index. Both the linewidth and free spectral range can be measured from the transmission spectrum of the microring under a wavelength sweep. Phase noise of the stabilized cw laser is fundamentally limited by the frequency discriminant and shot noise, which give the best resolvable frequency error. The corresponding phase noise is equivalent to the Schawlow-Townes linewidth of a passive cavity, as derived in Appendix B.

According to Equation (4.1), the thermal-optic coefficient and thermal expansion of the SiN microring must be engineered so that the thermal sensitivity $d(n_{\text{eff}} L_{\text{ring}}) / dT$ is as close to zero as possible. One feasible method is to deposit a polymer top cladding on top of the microring, and manipulate the cladding refractive index and thermal-optic coefficient by controlling the photo-bleaching time. For example, the temperature-dependent wavelength shift of a SiN ring resonator with DR1/PMMA cladding has been reduced to -0.018 pm/°C around 1600 nm [101], which suggests a relative wavelength shift on the order of $10^{-8}$. Regarding the ring resonator of the ESPIOR, if assuming a thermal conductance of 0.1 $\mathrm{WK}^{-1}$ and $\alpha_{\text{sub}} n_{\text{eff}} + \frac{dn_{\text{eff}}}{n_{\text{eff}} dT} \approx 2 \times 10^{-8}$, Equation (4.1) yields an optical phase noise of -31 dBc/Hz at 1-Hz offset. An OFD divides the 1-Hz-offset phase noise down to -111 dBc/Hz at 20-GHz microwave carrier frequency, if an ideal OFD factor of $20 \times \log_{10}(192 \text{ THz}/20 \text{ GHz}) = 80$ dB is realized.

Table 4.1. Parameters of the PDH loop.

| Parameter | Value | Parameter | Value |
|---|---|---|---|
| Incident power | $P_0 = 5$ mW | PD responsivity | $\rho = 1$ A/W |
| Carrier power | $P_c = 2.7$ mW | Q factor | $Q_{\text{ring}} = 5 \times 10^7$ |
| Sideband power | $P_s = 1.1$ mW | Frequency | $\nu_{\text{ring}} = 192$ THz (1560 nm) |
| Transimpedance | $G_{\text{TIA}} = 60$ dB | | |

When the microring is used as the optical frequency discriminator in the PDH loop, the frequency detection sensitivity is $k_{\text{PDH}} = -8\sqrt{P_c P_s}\rho G_{\text{TIA}} Q_{\text{ring}} / \nu_{\text{ring}}$. For a given microring, $k_{\text{PDH}}$

the frequency discriminant is maximized when the power ratio $P_s/P_c = 0.42$ [126]. With the parameters of the PDH loop in Table 4.1, the frequency discriminant $k_{\mathrm{PDH}} \approx -0.7\,\mathrm{mV/Hz}$.

Frequency noise of the cw laser is fundamentally limited by its total cavity loss $l_{\mathrm{tot}}$, which results in the Schawlow-Townes linewidth $\Delta\nu_{\mathrm{cwl}}^{\mathrm{ST}}$. As derived in Appendix B, cw laser phase noise due to the Schawlow-Townes linewidth is given by

$$\mathcal{L}_{\mathrm{cwl}}^{\mathrm{ST}}(f) = \frac{1}{f^2}\frac{1}{2}\frac{\Delta\nu_{\mathrm{cwl}}^{\mathrm{ST}}}{\pi} = \frac{1}{f^2}\frac{h\nu_{\mathrm{cwl}}}{8\pi^2}\frac{l_{\mathrm{tot}}}{T_{\mathrm{rt}}^2}\frac{T_{\mathrm{oc}}}{P_{\mathrm{out}}}n_{\mathrm{sp}} \tag{4.2}$$

where $h$ is the Planck's constant, $T_{\mathrm{rt}}$ the round-trip time, $T_{\mathrm{oc}}$ the output coupling ratio, $n_{\mathrm{sp}}$ the spontaneous emission factor and $P_{\mathrm{out}}$ the output power of the cw laser. The linewidth of the free-running cw laser usually exceeds the Schawlow-Townes linewidth because of environmental perturbation and technical noise. The thermal fluctuation induced phase noise can be estimated using Equation (4.1).

Table 4.2. Parameters of the cw laser.

| Parameter | Value | Parameter | Value |
|---|---|---|---|
| Frequency | $\nu_{\mathrm{cwl}} = 192$ THz (1560 nm) | Round-trip time | $T_{\mathrm{rt}} = 0.25$ ns |
| Output power | $P_{\mathrm{out}} = 100$ mW | Q factor | $Q = 10^6$ |
| Output coupling | $T_{\mathrm{oc}} = 0.05$ | Total loss | $l_{\mathrm{tot}} = 2\pi\nu_{\mathrm{cwl}}T_{\mathrm{rt}}/Q = 0.3$ |
| Spontaneous emission factor | $n_{\mathrm{sp}} = 1.2$ | Frequency tuning sensitivity | $k_{\mathrm{VCO}} = 100$ MHz/V |

Parameters of the cw laser in this model is listed in Table 4.2. The Schawlow-Townes linewidth, according to Equation (4.2), is $\Delta\nu_{\text{cwl}}^{\text{ST}} \approx 0.03\,\text{Hz}$, which corresponds to optical phase noise of -15 dBc/Hz at 1-Hz offset. Thermal fluctuation, however, significantly broadens the linewidth. If assume that $\alpha_{\text{sub}} n_{\text{eff}} + \frac{dn_{\text{eff}}}{n_{\text{eff}} dT} \approx 2\times 10^{-6}$ and the thermal conductance is 0.1 $\text{WK}^{-1}$, Equation (4.1) yields optical phase noise of ~9 dBc/Hz at 1-Hz offset, corresponding to a linewidth of 64 Hz at T = 300 K. This estimation only considers the white frequency noise due to temperature fluctuation, and does not include the impacts of other technical noise sources such as mechanical vibration and pump power fluctuation. As a comparison, the linewidth of an $\text{Al}_2\text{O}_3\text{:Er}^{3+}$ on silicon laser has been measured to be 1.7 kHz [127], whereas Equation (4.1) predicts a linewidth of 1.2 kHz for the laser.

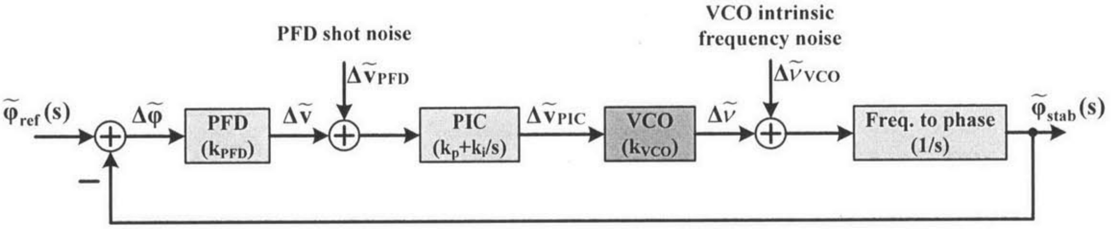
PFD shot noise
$\Delta\tilde{\nu}_{\text{PFD}}$
VCO intrinsic frequency noise
$\Delta\tilde{\nu}_{\text{VCO}}$
$\tilde{\varphi}_{\text{ref}}(s)$
$\Delta\tilde{\varphi}$
PFD
($k_{\text{PFD}}$)
$\Delta\tilde{\nu}$
PIC
($k_p+k_i/s$)
$\Delta\tilde{\nu}_{\text{PIC}}$
VCO
($k_{\text{VCO}}$)
$\Delta\tilde{\nu}$
Freq. to phase
(1/s)
$\tilde{\varphi}_{\text{stab}}(s)$
–

Figure 4.4. Block diagram of the phase-domain LTI noise model of an OPLL. $k_{\text{PFD}}$, phase frequency detector

From a linear and time-invariant (LTI) system perspective, standard loop analysis is applicable to the PDH loop, which can be represented by the block diagram of Figure 4.4, where quantities with tildes are the Laplace transforms of their respective time-domain quantities, and $s = \alpha + j\omega$ is the Laplace variable. Transfer function of each block is shown in parentheses. Phase detection sensitivity is $k_{\text{PFD}} = s \cdot k_{\text{PDH}}$. A time-domain integrator is explicitly included to convert frequency into phase. Parameters of the PIC are chosen according to the loop stability criteria and loop bandwidth requirement. The VCO frequency tuning sensitivity $k_{\mathrm{VCO}}$ is considered a constant value.

The PIC proportion gain and integral gain of the PDH loop are optimized using the MATLAB SISO Design Tool, which finds the optimum PIC parameters of a single-input-single-output (SISO) control loop for a given bandwidth and phase margin requirement. Appendix C gives more detail about the simulation in MATLAB. Although an external modulator enables high-speed frequency modulation of the cw laser, speed of the control loop will be limited by the gain and bandwidth of the electronics. Bench-top control electronics, for instance the FALC 110 from Toptica Photonics, have a signal delay of less than 15 ns (67 MHz), a proportional gain of 15dB – 80dB, and an integrator DC gain of 110 dB.

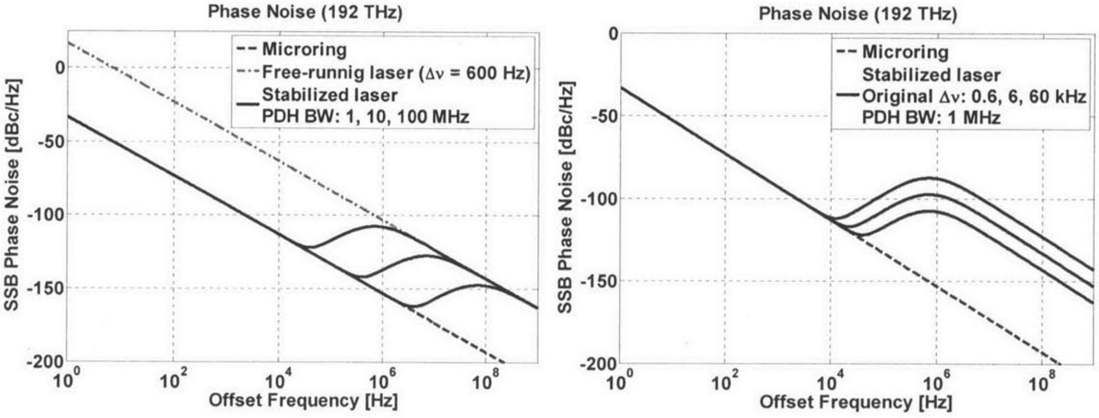

(a)

(b)

Figure 4.5. PDH loop parameters and attainable phase noise of the stabilized cw laser. (a) 600-Hz linewidth cw laser, and loop bandwidths of 1 MHz, 10 MHz and 100 MHz. (b) Loop bandwidth 1 MHz, and pre-stabilized cw laser linewidth of 600 Hz, 6 kHz and 60 kHz.

Figure 4.5 summarizes the phase noise of the stabilized cw laser at different PDH loop parameters and pre-stabilization cw laser linewidth. Phase noise of the microring resonator is chosen as -33dBc/Hz at 1-Hz offset frequency. In Figure 4.5 (a), the gain settings for the 1-

MHz, 10-MHz and 100-MHz loop are $(k_{\mathrm{i}}, k_{\mathrm{p}})$ = (85 dB, 20 dB), (105 dB, 30 dB) and (125 dB, 40 dB), respectively. If the loop bandwidth is fixed at 1 MHz, and the pre-stabilization cw laser linewidth increases from 600 Hz to 6 kHz and 60 kHz, the attainable phase noise is shown in Figure 4.5 (b).

The phase noise model of the PDH loop indicates that an enormous integrator gain is required to well suppress the phase noise of a free-running cw laser. This is mainly because that the low Q-factor of the microring (~$10^7$) reduces the frequency discriminant. As a comparison, the Q-factor of a bulk Fabry-Pérot ultrastable cavity is on the order of $10^{11}$. In addition, a 100-MHz/Hz frequency tunability of the cw laser is used in the simulation, assuming that an external modulator of high bandwidth is necessary. Thermal-optic tuning with an integrated heater is much more efficient in terms of frequency tuning, though its bandwidth is ~MHz [109]. In the following analysis, the phase noise of the 600-Hz per-stabilization cw laser linewidth and the 10-MHz PDH loop is chosen as the optical phase reference of the modelocked laser.

### 4.3.3 Optical Frequency Division

The PFD of the OPLL1 in Figure 4.3 includes a frequency divider and a phase detector, which is either a microwave mixer or a digital phase detector. A digital phase detector has a broad phase detection range, but requires its own frequency reference [128].

The VCO model of the optical comb line of frequency $\nu_n$ has a complex transfer function. Comb-line dynamics are expressed in a transfer matrix whose elements account for dependence of $\Delta f_{\mathrm{r}}$, $\Delta f_0$, and $\Delta \nu_n$ on each type of perturbation, respectively. Because frequency combs have two degrees of freedom, two separate controllers are required to fully stabilize all of the comb lines, and a $2\times2$ matrix is sufficient to describe comb dynamics. However, additional dimensions can always be included if, for example, complementary fast and slow controllers are used to reduce residual linewidth of optical frequency locking [29].

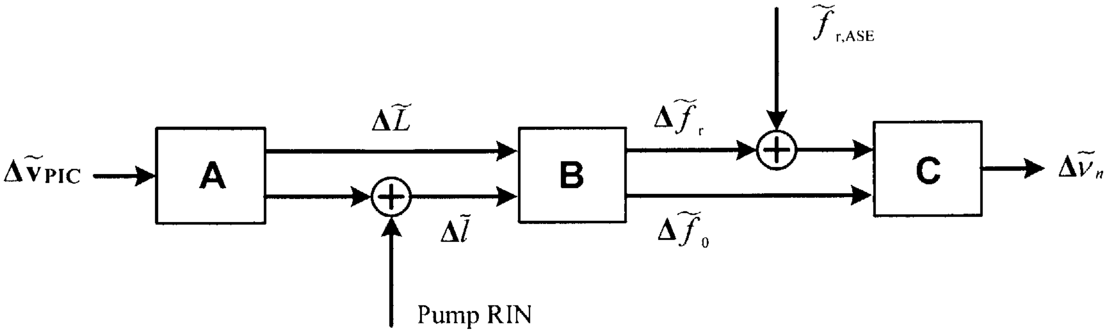

$\tilde{f}_{\mathrm{r,ASE}}$
$\Delta\tilde{L}$
$\Delta\tilde{f}_{\mathrm{r}}$
$\Delta\tilde{\nu}_{\mathrm{PIC}}$
A
B
C
$\Delta\tilde{\nu}_n$
$\Delta\tilde{l}$
$\Delta\tilde{f}_0$
Pump RIN

Figure 4.6. Block diagram of the VCO model for the $n^{\mathrm{th}}$ optical comb line.

A detailed VCO model of comb line $\nu_n$ is shown in Figure 4.6, in which cavity optical path length $L$ and cavity loss $l$ are chosen as the two controllers. Matrix $A=\begin{bmatrix}H_{L,V}(s) & H_{l,V}(s)\end{bmatrix}^{\mathrm{T}}=H_{L,V}(s)\begin{bmatrix}1 & G\end{bmatrix}^{\mathrm{T}}$ describes how $L$ and $l$ respond to the control voltage $V$ from the PIC. The elements $H_{L,V}(s)$ and $H_{l,V}(s)$ are related by a tunable gain $G$, which shapes frequency response of the VCO. Matrix $B=\begin{bmatrix}H_{r,L}(s) & H_{r,l}(s)\\ H_{0,L}(s) & H_{0,l}(s)\end{bmatrix}$ represents the responses of $f_{\mathrm{r}}$ and $f_0$ with respect to cavity length and cavity loss modulations. Crosstalk and orthogonality of the two modulations are included as the off-diagonal elements [27]. Elements of matrices $A$ and $B$ can be estimated from the analytical results [27], or experimentally measured in a particular frequency comb system [28]. Modulation bandwidth $\omega_{3\mathrm{dB}}$ can be explicitly included by stating that $H(s)=H\cdot\left(\frac{\omega_{3\mathrm{dB}}}{s+\omega_{3\mathrm{dB}}}\right)^{n}$, which imposes a -20$n$ dB/decade roll-off for the frequencies beyond $\omega_{3\mathrm{dB}}$. Matrix $C=\begin{bmatrix} n & 1 \end{bmatrix}^{\mathrm{T}}$ is essentially the comb equation $\nu_n = f_0 + n\cdot f_r$. Noise due to amplified spontaneous emission (ASE) [69, 71, 129] and relative intensity noise (RIN) [27, 69, 129] are also included in this model as the $f_0$ and $f_{\mathrm{r}}$ noise of the free-running modelocked laser.

As an example, if cavity length and loss modulations have 3-dB bandwidths of $\omega_L$ and $\omega_l$ with a single pole, respectively, the VCO transfer function is

$$k_{\mathrm{VCO},\nu_n}(s) = H_{L,\nu}\left(\omega_L H_{\nu_n,L} + \omega_l G H_{\nu_n,l}\right)\frac{s-s_0}{\left(s+\omega_L\right)\left(s+\omega_l\right)} \tag{4.3}$$

where $H_{\nu_n,L} = H_{0,L} + nH_{r,L}$ and $H_{\nu_n,l} = H_{0,l} + nH_{r,l}$ are the comb line response to cavity length modulation and loss modulation, respectively, and $s_0$ is

$$s_0 = -\frac{\omega_L \omega_l\left(H_{\nu_n,L} + GH_{\nu_n,l}\right)}{\omega_L H_{\nu_n,L} + \omega_l G H_{\nu_n,l}} \tag{4.4}$$

An important case is that when $\omega_L = \omega_l = \omega$ and $G = -H_{0,L}/H_{0,l}$, Equation (4.3) is reduced to

$$k_{\mathrm{VCO},\nu_n}(s) = \omega H_{L,\nu} n\left(H_{r,L} + GH_{r,l}\right)\frac{1}{s+\omega} \tag{4.5}$$

In this case, the modulation responses of $f_0$, i.e. $H_{0,L}(s)$ and $H_{0,l}(s)$, are absent. And frequency tuning of the optical frequency $\nu_n$ only comes from the change in comb spacing, because the proportional gain $G$ is chosen in such a way that $\Delta f_0/\Delta V = \left(H_{0,L} + GH_{0,l}\right)H_{L,V} \equiv 0$. This is equivalent to $f_{\mathrm{CEO}}$ stabilization, but does not require detecting $f_0$ with an $f-2f$ interferometer. The $GH_{r,l}$ term in Equation (4.5) accounts for the cross-influence of loss modulation on $f_{\mathrm{r}}$.

Table 4.3. Parameters of the modelocked laser.

| Parameter | Value | Parameter | Value |
|---|---|---|---|
| Average power | $P_{\mathrm{ave}} = 5$ mW | Pulse duration | $\tau_0 = 500$ fs |
| Repetition rate | $f_{\mathrm{r}} = 2$ GHz | Total loss | $l_{\mathrm{tot}} = 0.3$ |
| Output coupling | $T_{\mathrm{oc}} = 0.01$ | Pump RIN | -130 dB/Hz |
| Dispersion | $D =$ -500 fs$^2$ | Pump power | $P_{\mathrm{p}} = 500$ mW |
| Spontaneous emission factor | $n_{\mathrm{sp}} = 1.3$ | Quantum-limited Timing jitter | $\Delta\tau_0 = 84$ fs<br>integrated in [1Hz, 1GHz] |

In a closed loop, this cross-talk becomes important regarding loop stability. In other words, a stable loop may exert an upper limit on the magnitude of $G$ that is insufficient to fully suppress $f_0$ fluctuation. This reduces the optical frequency division ratio. In this light, the most important quantity derived from the stabilized phase of comb line $\nu_n$ is $\Delta\tilde{f}_{\mathrm{r}}(s)$, because it implies noise reduction of the comb spacing and effectiveness of OFD. As a result, the phase model of OPLL1 consists of two step: First, the phase noise of $\nu_n$ is modelled, including contributions from the pump RIN and the ASE-induced timing jitter of the free-running modelocked laser; second, phase noise of the stabilized repetition rate is calculated from the transfer function from $\Delta\tilde{f}_{\mathrm{r}}$ to $\tilde{\varphi}_{\mathrm{stab}}$.

The parameters of the modelocked laser are listed in Table 4.3. In modeling the phase noise of $\nu_n$, the single-input-single-output MATLAB toolbox is applicable to the OPLL without external noise sources. In this case, the modelocked laser is regarded a black-box VCO. When the impact of pump RIN and ASE-induced timing jitter needs to be considered, the MATLAB multiple-input-multiple-output (MIMO) tools offer a means to compute the transfer function between any input port and output port. Appendix C gives more detail about the simulation in MATLAB. In this way, the transfer functions of $\Delta\tilde{l}$ to $\tilde{\varphi}_{\mathrm{stab}}$, and $\Delta\tilde{f}_{\mathrm{r}}$ to $\tilde{\varphi}_{\mathrm{stab}}$, account for the contributions from pump RIN and timing jitter, respectively.

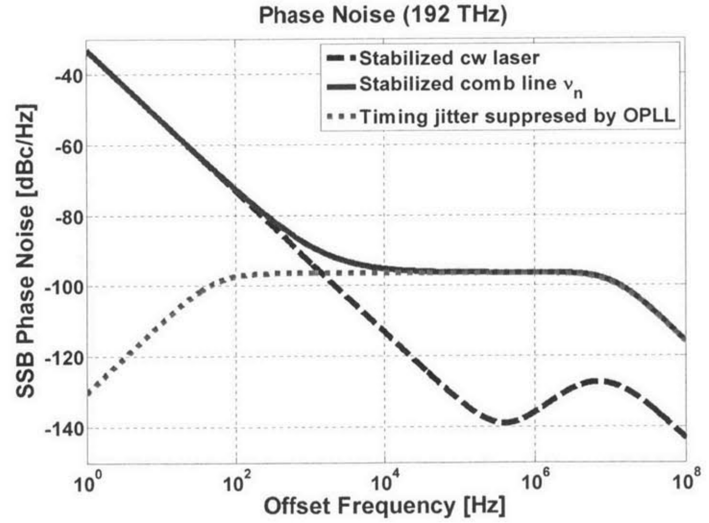

Figure 4.7. Phase noise of the stabilized $n^{\text{th}}$ optical comb line. Loop bandwidth is 10 MHz.

Phase noise of the comb line $\nu_n$ is plotted in Figure 4.7. It is assumed that the loop bandwidth is 10 MHz, the same as the PDH loop. The loop gains are $\left(k_{\mathrm{i}}, k_{\mathrm{p}}\right) =$ (40 dB, 15 dB). Values of the elements of matrices $A$ and $B$ are $H_{L,V}$ = 100 nm/V, $H_{r,L}$ = -$10^{10}$ Hz/m, $H_{0,L}$ = $10^{13}$ Hz/m, $H_{r,l}$ = -$10^{4}$ Hz/W and $H_{0,l} = 10^{9}$ Hz/W. In addition, a single-pole at 100 MHz is added to the elements of matrix $B$, so that the modulation bandwidth is $\omega_L = \omega_l = \omega = 2\pi \cdot 100$ MHz. These values are only for an order-of-magnitude estimation, and true values can be experimentally quantified for a real laser. Magnitude of the gain $G$ is chosen as $\left|H_{0,L}/H_{0,l}\right| =$ $10^{4}$. It can be seen in Figure 4.7 that the loop can suppressed the timing jitter up to the loop bandwidth 10 MHz, and comb-line phase noise follows the stable cw laser up to ~10 kHz.

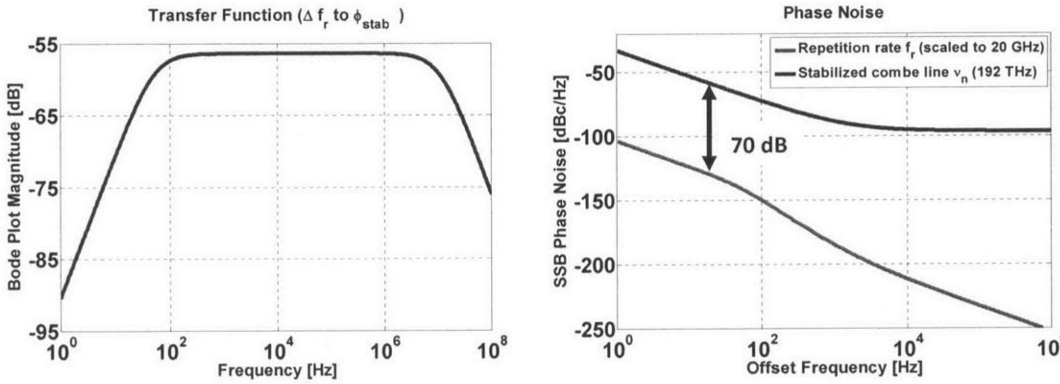

(a) (b)

Figure 4.8. Phase noise of the repetition rate. (a) Transfer function from the repetition rate to the comb line. (b) Phase noise of the repetition rate; the optical frequency division ratio is >70 dB.

The phase noise of the stabilized comb line $\nu_n$ comprises of the phase noise of both $f_{\mathrm{r}}$ and $f_0$. The transfer function from $\Delta\tilde{f}_{\mathrm{r}}$ to $\tilde{\varphi}_{\mathrm{stab}}$, shown in Figure 4.8 (a), implies the portion of repetition-rate frequency noise to the stabilized come line phase noise. By applying the transfer function to the $\tilde{\varphi}_{\mathrm{stab}}$ and converting to phase noise, the stabilized repetition-rate phase noise is plotted in Figure 4.8 (b), in which the microwave carrier frequency is scaled to 20 GHz. The effective ratio of OFD is 70 dB at low frequencies. Although the division ratio is less than the carrier conversion ratio of 80 dB, the phase noise at 1-Hz offset frequency is -103dBc/Hz, the same performance as the Ti:sapphire-based system with the $f_{\text{CEO}}$ stabilized by a $f-2f$ interferometer [6].

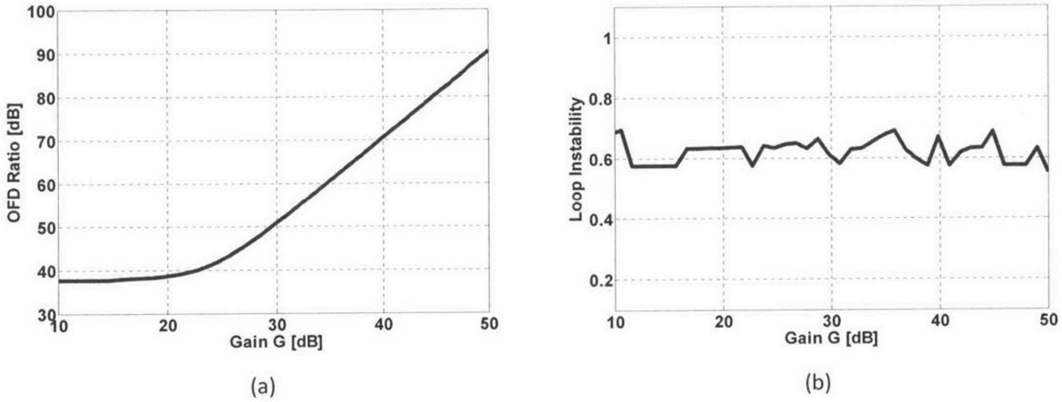

Figure 4.9. Optical frequency division at different gain values. (a) Effective OFD ratio, 192 THz to 20 GHz. (b) Loop instability. Loop is unstable if the instability exceeds unity.

To investigate the impact of the gain $G$ on the attainable OFD factor, the noise modelling process is repeated for a range of gain settings. At each given gain, the OFD ratio at 1-Hz offset frequency and the loop instability are recorded, and plotted in Figure 4.9. The loop instability indicates if the requirements on gain margin, phase margin and bandwidth are all realized. A loop instability value exceeding unity means at least one of the requirements is not satisfied. In the simulation, 45° phase margin, 7.6 dB gain margin and 10 MHz bandwidth are used to evaluate loop stability.

In addition to the gain $G$, the modulation bandwidths $\omega_L$ and $\omega_l$ also affect the OFD factor, because they shape the frequency response of the VCO and the noise transfer functions.

Figure 4.10 shows the situation when the gain $G$ is set at 30 dB, and the modulation bandwidth is varied. It would require more than 1 GHz modulation bandwidth to suppress the 1-Hz offset phase noise below -100 dBc/Hz. This is feasible if high-speed intracavity phase and amplitude modulators are used.

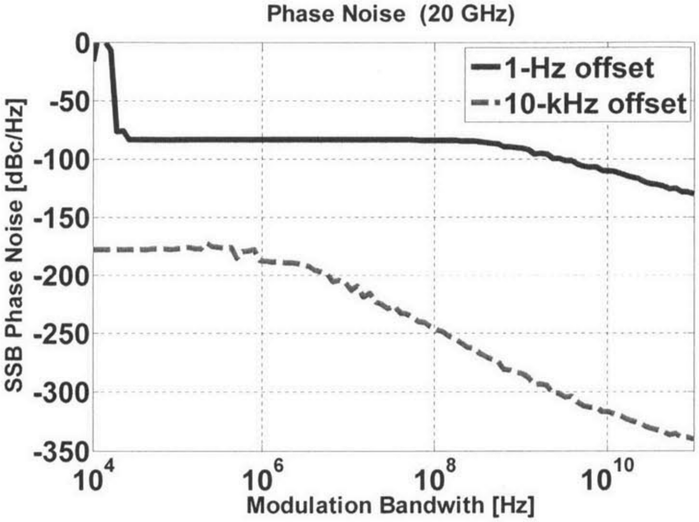

Figure 4.10. Phase noise at 1-Hz and 10-kHz for different modulation bandwidths.

### 4.3.4 Microwave Readout

The generated optical single frequency $\nu_{\mathrm{cw2}}$ can be modelled in a similar fashion as the PDH loop, and the VCO in this case is the SSB phase modulator and a constant $k_{\mathrm{VCO}}$ is justified. As the phase reference, frequency of the $(n+\Delta n)^{\mathrm{th}}$ comb line is $\nu_{n+\Delta n} = \nu_n + \Delta n(f_{\mathrm{r}} + \Delta f_{\mathrm{r}})$, assuming that $\Delta f_0$ has been sufficiently suppressed and $\Delta n$ is a small number. Phase noise of the extracted microwave signal is given by $\tilde{\varphi}_{\mathrm{uwave}}(s) = \tilde{\varphi}_{\mathrm{cw2}}(s) - \tilde{\varphi}_{\mathrm{cw1}}(s)$.

At large off-set frequencies, the phase noise $\tilde{\varphi}_{\mathrm{uwave}}(s)$ is limited by the photodetector noise, including shot noise, thermal noise and dark current. With sufficient optical power and

50Ω load resistance, shot noise becomes significant. The corresponding phase noise is $\mathcal{L}_{\text{shot}} = \dfrac{e}{4\rho P}$, where $e$ is the electric charge, $\rho$ the photodetector responsivity and $P$ the incident optical power. For $\rho$=1 A/W, and $P$=20 mW, $\mathcal{L}_{\text{shot}}$ = -164 dBc/Hz.

An electronic VCO is needed to drive the SSB phase modulator to generate the single frequency $\nu_{\text{cw2}}$. Although the OPLL locks $\nu_{\text{cw2}}$ to the comb line $\nu_{n+\Delta n}$, out-of-bandwidth phase noise of the electronic VCO directly transfers to the microwave phase noise. As a result, enough bandwidth is required to suppress the high-frequency phase noise below the shot noise level; and a low-noise electronic VCO is preferred. For instance, the low-noise K-band VCO with room-temperature ferroelectric varactors has a phase noise ~160 dBc/Hz at 10-MHz offset frequency and 19.6 GHz carrier frequency [130]. Consequently, a loop bandwidth of 10 MHz – 100 MHz will be needed.

## 4.4 Fiber-Optic Demonstration

A bench-top version of the ESPIOR is constructed using off-the-shelf fiber-optic components and erbium fiber lasers. In addition to demonstrating the photonic microwave oscillator approach, the demonstration system offers a testbed to investigate system performance at a component level. In particular, the testbed assists to understand the impact of carrier-envelope offset (CEO) frequency and feasible means to keep it under control.

### 4.4.1 Stable Continuous-Wave Laser

The stable cw laser employed in the demonstration is an Ethernal SlowLight laser from Orbits Lightwave [131]. Frequency noise (provided by the vendor) and phase noise of the laser is shown in Figure 4.11. The linewidth of 1 ms observation time is ~400 Hz. The laser outputs up to 40 mW optical power at $\nu_{\mathrm{cwl}} = 192.1$ THz (1560.6 nm).

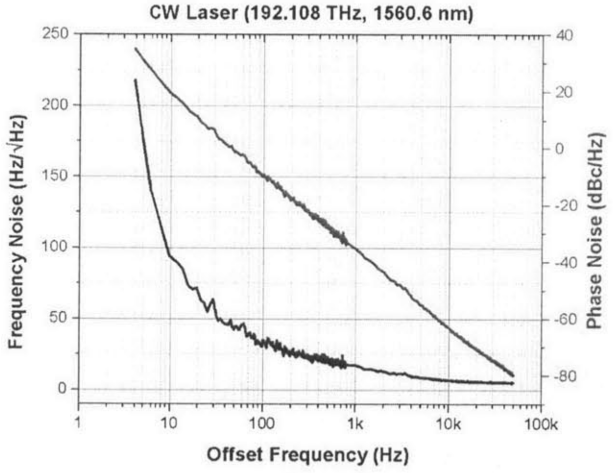

Figure 4.11. Frequency noise and phase noise of the Ethernal SlowLight laser.

The laser is currently thermally stabilized by the athermal package and built-in temperature controller. Though not yet locked to a reference cavity, the laser has frequency tunability enabled by a fast PZT (~10 kHz bandwidth) and current modulation (~ 100 kHz bandwidth). Ultrastable rigid Fabry-Pérot cavities and control electronics are now commercially available. Laser linewidth < 3Hz of 1 s observation time can be expected.

### 4.4.2 Optical Frequency Division

The modelocked laser is the M-Fiber series erbium fiber frequency comb from Menlo Systems. The 250-MHz oscillator is modelocked by nonlinear polarization rotation, and can be modulated by the built-in PZT and pump power. The erbium-doped amplifier provides more than 1 nJ pulse energy for supercontinuum generation and $f_0$ detection. Frequency comb dynamics of the same type of system has been previously reported [28]. Modulation bandwidths of the PZT and pump power are ~10 kHz and ~50 kHz, respectively.

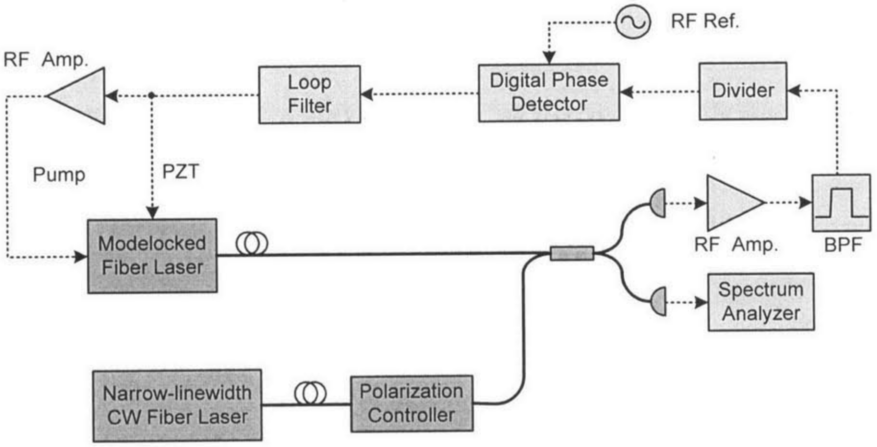
RF Ref.
RF Amp.
Loop Filter
Digital Phase Detector
Divider
Pump
PZT
Modelocked Fiber Laser
RF Amp.
BPF
Spectrum Analyzer
Narrow-linewidth CW Fiber Laser
Polarization Controller

Figure 4.12. Optical phase locked loop for modelocked laser stabilization.

The OPLL in Figure 4.12 is used to lock the comb line $\nu_n$ to the cw laser frequency $\nu_{\mathrm{cw1}}$, and to investigate the OFD scheme described in this chapter. The frequencies $\nu_n$ and $\nu_{\mathrm{cw1}}$ are mixed by the $2\times2$ coupler and the frequency difference is detected by the photodetector. Beat signals resulting from the comb lines other than $\nu_n$ are removed by the bandpass filter. The combination of the $25\times$ frequency divider (FPS-25-8, RF Bay) and the digital phase detector (DXD200, Menlo Systems) provides a large linear phase detection range. Frequency reference of the digital phase detector is provided by an external microwave reference. The loop filter (LB1005, New Focus) drives the PZT in the modelocked laser and modulates comb line frequency. Error signal of the PZT loop is amplified by an adjustable proportional gain $G$ and then modulates the pump power of the modelocked laser.

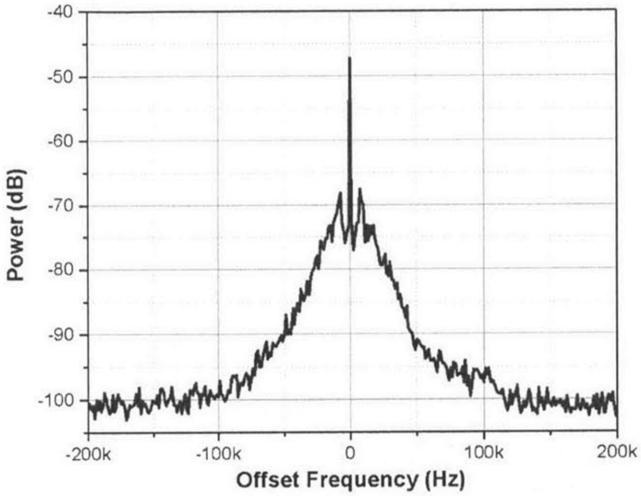

Figure 4.13. Beat signal of $\nu_n$ and $\nu_{cwl}$ . Resolution bandwidth 30 Hz. Center frequency 325 MHz. Power reference is 0 dBm.

Figure 4.13 shows the beat signal when the PZT loop is closed. The residual jitter is ~4 fs for offset frequencies < 100 kHz. The proportional gain $G$ is then applied. Phase noise of the pulse repetition rate is monitored by the signal source analyzer, at 1-GHz carrier frequency while the gain $G$ is gradually increased. The lowest phase noise, shown as the red curve in Figure 4.14, is achieved at $G$ = ~15 dB, whereas further increasing the gain breaks the PZT loop. The resulting OFD ratio is ~ 80 dB for 1-GHz carrier frequency, corresponding to 54 dB for 20-GHz carrier frequency. As a comparison, if $f_0$ is actually detected by the $f-2f$

interferometer and locked to an RF oscillator with pump power modulation (the gain $G$ is off), the OFD ratio is ~ 100 dB for 1-GHz carrier frequency.

The limited OFD ratio is due to the PZT and pump modulation bandwidth, and the cross-talk of the two modulation mechanisms. To further reduce the phase noise, a home-built modelocked laser with intracavity modulators can be employed. An intracavity electro-optic modulator can extend the cavity optical path length modulation speed to 100 MHz. An intracavity acousto-optic modulator can be used as a fast loss modulator of > 5MHz bandwidth [132].

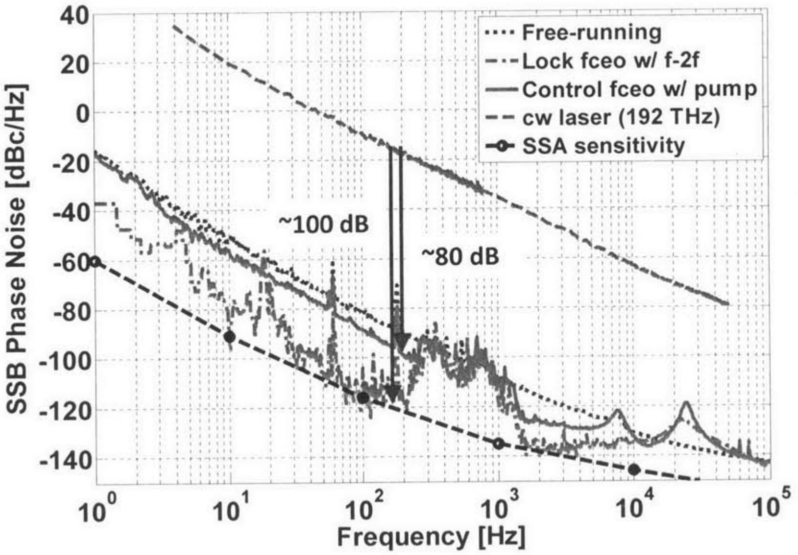

Figure 4.14. Phase noise of the pulse repetition rate, with and without the proportional gain applied.

### 4.4.3 Microwave Readout

Since fast intracavity modulation mechanism is not readily available in the commercial M-Fiber modelocked laser, an external acousto-optic frequency shifter (AOFS) is used instead, as shown in Figure 4.15. The external AOFS shifts the whole frequency comb and therefore does not contribute to repetition rate stabilization or OFD. That said, it is an effective means to modulation comb lines and can future reduce the residual timing jitter of the optical beat in Figure 4.13. Moreover, the tight locking that reduces the timing jitter of $\nu_{n+\Delta n}$ relative to $\nu_{\mathrm{cw1}}$ is important to demonstrate the microwave readout. The AOFS (Gooch & Housego) has a center modulation frequency of 80 MHz, and a modulation bandwidth of ~ 5MHz. The VCO modulation signal is boosted by a low-noise RF power amplifier. Optical power in the +1st order is ~70% of the total incident power.

The fiber-coupled lithium niobate SSB phase modulator (PM-0K5-20-PFU-PFU, EOSPACE) is used to generate the single frequency $\nu_{\mathrm{cw2}}$. The phase modulator is driven by a low-noise VCO (E8257D, Agilent) and is temperature-stabilized to reduce slow drift of the bias voltages. With 5-GHz RF signal of +15dBm power, the sideband suppression ratio is ~ 25 dB.

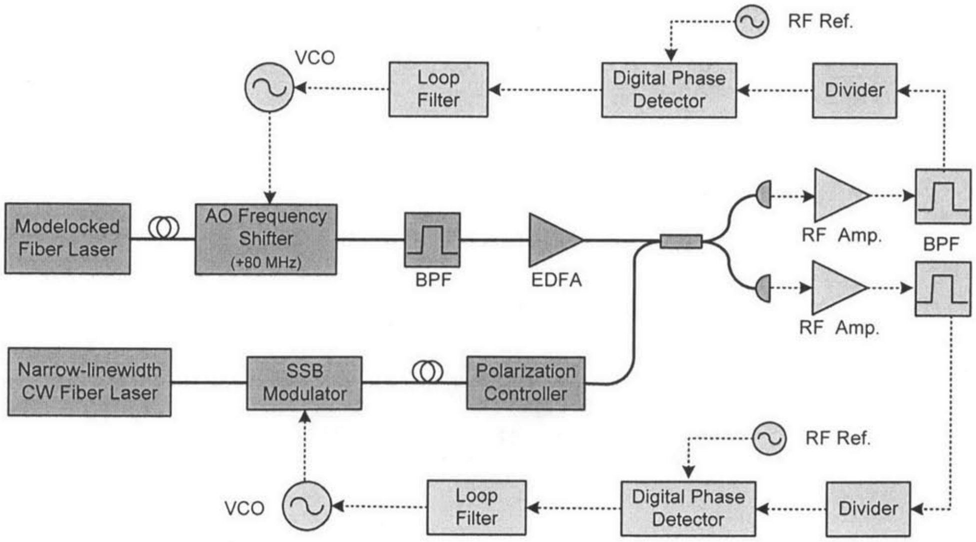
RF Ref.
VCO
Loop Filter
Digital Phase Detector
Divider
Modelocked Fiber Laser
AO Frequency Shifter (+80 MHz)
BPF
EDFA
RF Amp.
BPF
RF Amp.
Narrow-linewidth CW Fiber Laser
SSB Modulator
Polarization Controller
RF Ref.
VCO
Loop Filter
Digital Phase Detector
Divider

Figure 4.15. Optical phase locked loops for microwave readout. The PZT loop is not shown.

The OPLLs used to lock the VCOs of the AOFS and the SSB phase modulator are similar to the OPLL in Figure 4.12, except that the frequency divider ratios and RF reference frequencies are different. The RF references to the digital phase detectors are all derived from the same 1-GHz signal of the Agilent E8257D. The optical beat signals are shown in Figure 4.16. The AOFS reduces the residual jitter of the optical beat to 0.2 fs and the coherent carrier is clearly seen in Figure 4.16. The gains of the SSB phase modulator loop are chosen to match the bandwidth of the other loop.

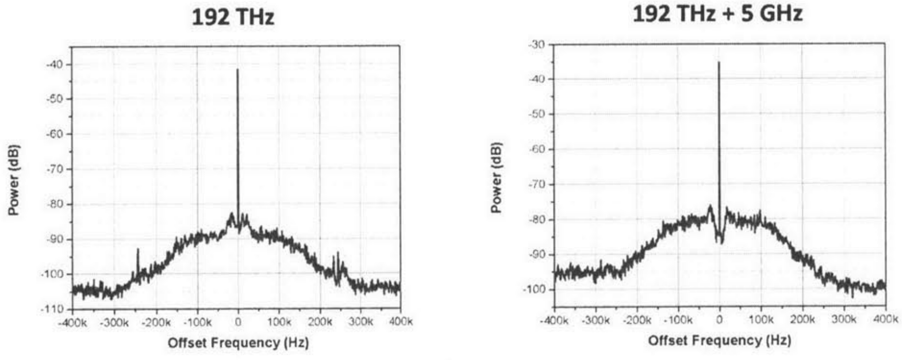

(a) (b)

Figure 4.16. Optical beat signals of the OPLLs in microwave readout. (a) The AOFS loop. (b) The SSB phase modulator loop. Both, resolution bandwidths 30 Hz, residual timing jitter 0.2 fs (<100 kHz). Power reference is 0 dBm.

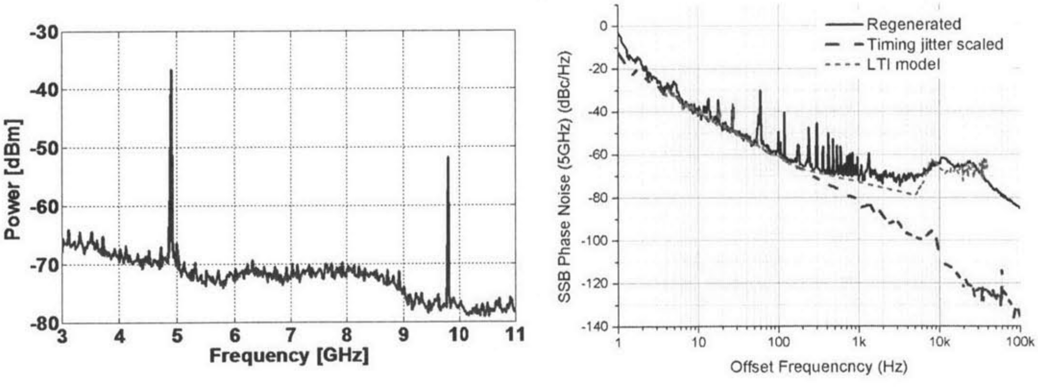

(a) (b)

Figure 4.17. Extracted microwave signals. (a) RF spectrum. (b) Phase noise at 5-GHz carrier frequency.

Once all of the three OPLLs (PZT loop, AOFS loop, and SSB phase modulator loop) are all closed, the single frequency $\nu_{cw2}$ is beat against the cw laser frequency $\nu_{cw1}$ in a $2\times 2$ fiber coupler, and the beat note is detected by a fast photodetector (ET-3500F, EOTech). The RF spectrum of the photodetected optical beat is shown in Figure 4.17 (a). The 5-GHz microwave signal is regenerated from the 250-MHz repetition rate, which is equivalent to repetition-rate multiplication.

The 5-GHz tone is filtered out and amplified. Its phase noise is measured by the signal source analyzer. In Figure 4.17 (b), phase noise of the regenerated 5-GHz signal follows the phase noise obtained by direct photodetection of the laser pulse train. The dotted red curve shows the predicted phase noise from the LTI model previously discussed in this chapter. The results prove that the readout scheme is capable of extracting microwaves from beating two optical single frequencies. The phase noise is currently limited by the PZT loop bandwidth around 10 kHz.

# Chapter 5

# Conclusion and Future Work

## 5.1 Femtosecond Cr:LiSAF Lasers

Diode-pumped femtosecond Cr:LiSAF lasers modelocked by semiconductor saturable absorbers are low cost, highly efficient and compact. With the optimized saturable absorber and dispersion compensating mirrors, sub-100-fs pulses with kW peak power is achieved in the 1-GHz repetition-rate Cr:LiSAF laser. The demonstrated peak power represents a two order of magnitude improvement compared with the earlier reported performance, and is sufficient to enable a wide range of experiments. Higher repetition rates, higher peak powers, shorter pulsewidths and wavelength tunability can be expected with improvements in pump diode and saturable absorber technology. Low-cost, compact and efficient GHz Cr:Colquiriite lasers can be an ideal source for several important application areas in ultrafast science and technology.

The recent advancement in high brightness tapered laser diode enables power scaling. Single-mode diode laser source of 1-W power and nearly transform-limited ($M^2 \sim 1.3$) beam profile at 650 nm is already available [61, 133]. While pumping with the high-power diode lasers, regenerative amplifiers based on Cr:LiSAF gain medium are expected to amplify the femtosecond seed pulses to hundreds of $\mu$J pulse energy level at a few kHz repetition rate. With the high pulse energy, harmonic and sum frequency generation and optical parametric amplification will extend the wavelength tuning range of Cr:LiSAF lasers into the visible and infrared regions. The broad tunability is important to a range of applications, such as nonlinear optical microscopy and pump probe spectroscopy. In addition, the amplified pulses facilitates carrier-envelop-offset frequency stabilization, and enables a fully stabilized Cr:LiSAF optical frequency comb.

## 5.2 Photonic Microwave Oscillators

Optical frequency division of an ultrastable optical single-frequency produces microwave signals with ultralow phase noise that rivals the state-of-the-art microwave oscillators. Currently, rigid Fabry-Pérot cavity and Ti:sapphire modelocked laser employed in photonic microwave oscillators limit the wide use of this technology, due to their large footprint and high energy consumption. The ESPIOR architecture and the phase noise model presented in this thesis suggest that it is feasible to design a chip-scale photonic microwave oscillator whose noise performance approaches that of the bench-top system. Both the phase noise model and the fiber-optic demonstration indicate that effective frequency division is attainable without carrier-envelope-offset frequency detection, and microwave signals can be read out by beating the two stabilized optical single frequencies. The ESPIOR architecture circumvents the usual needs of supercontinuum generation, second harmonic generation and photodetection power requirement, which are quite challenging to implement on chip. The demonstration is an important step towards on-chip OFD.

The phase noise model developed in this thesis does not include noise of the electronics used in the phase locked loops. A feasible and necessary complement to the feedback loop analysis is a hybrid optics-electronics model that contains noise contribution from the electronic components. The hybrid model can be implemented in the standard Verilog-A language, which simulates the system in time domain.

Demonstration of silicon photonics components of the ESPIOR and system-level performance is currently being studied and tested. In addition, an ultrastable reference optical cavity is being implemented in the fiber-optic testbed, in order to further reduce the linewidth of the continuous-wave fiber laser and to achieve improved phase noise. Once succeeded, a second ESPIOR demonstration system will also be built for low-noise microwaves characterization. A balanced optical cross-correlator can be utilized to measure the stabilized timing jitter in optical domain.

# Appendix A

# Balanced Cross-Correlation of sech$^2$-Shaped Laser Pulses

For lasers pulses longer than a quarter of the group velocity walk-off after a single pass, the assumption is valid that overlapping of the two fundamental pulses varies slowly inside the BBO crystal [134]. By adapting Equation (9) in reference [134] to sum-frequency generation, the intensity of sum-frequency field at distance $L$ for temporally overlapped (relative delay $\Delta t = 0$) fundamental fields is

$$I_3(t,L) = \frac{2(\omega_1+\omega_2)^2 d_{eff}^2 L^2}{\varepsilon_0 c^3 n_1^e n_2^o n_3^e} I_1(t-t_1) I_2(t-t_2) \equiv A L^2 I_1(t-t_1) I_2(t-t_2) \qquad \text{(A.1)}$$

where $t_1 = \left(v_{g1,e}^{-1} + v_{g3,e}^{-1}\right)\frac{L}{2}$, $t_2 = \left(v_{g1,o}^{-1} + v_{g3,e}^{-1}\right)\frac{L}{2}$, $v_{g3,e} = c / n_3^e = c / 1.699$, $d_{eff}$ the effective SFG coefficient and $\varepsilon_0$ the vacuum dielectric constant. This shows that the intensity of sum-frequency field at the end of crystal is proportional to the product of time-shifted intensities of the fundamental fields. The temporal shift is approximated as that in the middle of the crystal.

When there is timing jitter or repetition rates of the two lasers are different, a relative delay $\Delta t$ of the fundamental pulse pair is introduced. In this case, the sum-frequency intensities of forward and backward passes are

$$\begin{aligned} I_{\mathrm{f}}(t) &= AL^2 I_1\left(t-t_1-\Delta t\right) I_2\left(t-t_2\right) \\ I_{\mathrm{b}}(t) &= AL^2 I_1\left(t-2t_1-\Delta t\right) I_2\left(t-2t_2\right) \end{aligned} \tag{A.2}$$

The photodetectors voltage outputs are amplified time average of the ultrafast pulse envelop intensities, which is a function of the instantaneous timing jitter $\Delta t$. This can be expressed as

$$\begin{aligned} V_{\mathrm{f}}(\Delta t) &= GAL^2 \int_{-\infty}^{+\infty} I_1\left(t-t_1-\Delta t\right) I_2\left(t-t_2\right) dt \\ V_{\mathrm{b}}(\Delta t) &= GAL^2 \int_{-\infty}^{+\infty} I_1\left(t-2t_1-\Delta t\right) I_2\left(t-2t_2\right) dt \end{aligned} \tag{A.3}$$

where $G$ [W/V] is the transimpedance gain including the photodetectors' response. The ultrashort pulse from saturable absorber modelocked Cr:LiSAF lasers has a shape close to sech$^2$, i.e. $I_j = I_{j0} \sec h^2\left(t/\tau_0\right), j = 1,2$, where FWHM pulse duration $\tau_{\mathrm{p}} = 1.76\tau_0$.

Equation (A.3) can be evaluated analytically for sech$^2$-shape pulses. For simplicity, assume the fundamental pulse pair has identical pulse duration. The integral has a general form of

$$\begin{aligned} V(\Delta t) &= C \int_{-\infty}^{+\infty} \sec h^2\left(\frac{t}{\tau_0} - a\right) \sec h^2\left(\frac{t}{\tau_0} - b\right) dt \\ &= 16C\tau_0 \int_{-\infty}^{+\infty} \left(\frac{e^{x-a}}{e^{2(x-a)}+1}\right)^2 \left(\frac{e^{a-b}e^{x-a}}{e^{2(a-b)}e^{2(x-a)}+1}\right)^2 dx \end{aligned} \tag{A.4}$$

Let $y=e^{2(x-a)}$ and $B=e^{2(a-b)}$, then $dy=2ydx$ with $x\in[-\infty,+\infty]$ and $y\in[0,+\infty]$. Equation (A.4) becomes

$$\begin{aligned}
V(\Delta t) &= 8B^{-1}C\tau_0\int_0^{+\infty}\frac{y}{\left[y+1\right]^2}\frac{y}{\left[y+B^{-1}\right]^2}dy \\
&= \frac{8C\tau_0}{\left(B-1\right)^3}\int_0^{+\infty}\frac{\left(B+B^2\right)y+2}{\left[y+B^{-1}\right]^2}-\frac{\left(B+B^2\right)y+2B^2}{\left[y+1\right]^2}dy \\
&= 8C\tau_0\frac{B}{\left(B-1\right)^3}\left[2-2B+(1+B)\ln B\right]
\end{aligned} \tag{A.5}$$

With $B=e^{2(a-b)}\geq 0$, the integral can be evaluated as

$$V(\Delta t)=4C\tau_0\csc h^2\left(a-b\right)\left[(a-b)\cot h(a-b)-1\right] \tag{A.6}$$

For both passes in the cross-correlator, $C=GAL^2I_{10}I_{20}$. In the forward pass, $a=\left(t_1+\Delta t\right)\tau_0^{-1}$, $b=t_2\tau_0^{-1}$. In the backward pass, $a=\left(2t_1+\Delta t\right)\tau_0^{-1}$, $b=2t_2\tau_0^{-1}$.

# Appendix B

# Schawlow-Townes Linewidth of Single-Frequency Laser

The general form of the quantum-limited laser linewidth, the Schawlow-Townes linewidth, is given in [135]. With an additional spontaneous emission factor $n_{\mathrm{sp}}$, the full-width-at-half-maximum (FWHM) linewidth is

$$\Delta\nu = \frac{h\nu}{4\pi}\frac{l_{\mathrm{tot}}}{T_{\mathrm{rt}}^2}\frac{T_{\mathrm{oc}}}{P_{\mathrm{out}}}n_{\mathrm{sp}} \tag{B.1}$$

where $h$ is the Planck's constant, $T_{\mathrm{rt}}$ the round-trip time, $T_{\mathrm{oc}}$ the output coupling ratio, $l_{\mathrm{tot}}$ the total cavity loss, and $P_{\mathrm{out}}$ the output power of the cw laser.

In terms of optical quality factor (Q-factor) $Q = 2\pi\nu T_{\mathrm{rt}}/l_{\mathrm{tot}}$, the linewidth becomes

$$\Delta\nu = \pi h\nu\left(\frac{\nu}{Q}\right)^2\frac{T_{\mathrm{oc}}}{l_{\mathrm{tot}}P_{\mathrm{out}}}n_{\mathrm{sp}} \tag{B.2}$$

The white frequency noise corresponding to the linewidth is

$$S_f = \frac{\Delta \nu}{\pi} = h\nu \left(\frac{\nu}{Q}\right)^2 \frac{T_{\text{oc}}}{l_{\text{tot}} P_{\text{out}}} n_{\text{sp}} \tag{B.3}$$

The single sideband phase noise is

$$\mathcal{L}(f) = \frac{S_f}{2}\frac{1}{f^2} = \frac{h\nu}{2}\left(\frac{\nu}{Q \cdot f}\right)^2 \frac{1}{P_{\text{out}}}\frac{T_{\text{oc}}}{l_{\text{tot}}} n_{\text{sp}} \tag{B.4}$$

Alternatively, since $Q = 2\pi\nu T_{\text{rt}} / l_{\text{tot}}$,

$$\mathcal{L}(f) = \frac{h\nu}{8\pi^2}\frac{l_{\text{tot}} T_{\text{oc}}}{T_{\text{rt}}^2 P_{\text{out}}} n_{\text{sp}} f^{-2} \tag{B.5}$$

As an example, assume a hypothetical laser with $Q = 10^6$, $P_{\text{out}} = 10$ mW, $T_{\text{oc}} = 0.1$, $T_{\text{rt}} = 0.5$ ns, $n_{\text{sp}} = 1$, and $l_{\text{tot}} = 0.61$. The Schawlow-Townes linewidth is $\Delta\nu = 0.25$ Hz. The frequency noise according to Equation (B.3) is $S_f = 0.08$ Hz$^2$/Hz. The phase noise at 1-Hz offset frequency, according to Equation (B.4) is $\mathcal{L}(1) = -14$ dBc/Hz.

A special case is that when the parasitic losses are negligible and the output coupling is the only loss, so that $l_{\text{tot}} = T_{\text{oc}}$ and $Q = 2\pi\nu T_{\text{rt}} / T_{\text{oc}}$. In this case, the phase noise is

$$\begin{aligned} \mathcal{L}(f) &= \frac{h\nu}{2}\left(\frac{\nu}{Q \cdot f}\right)^2 \frac{1}{P_{\text{out}}} n_{\text{sp}} \\ &= \frac{h\nu}{8\pi^2 P_{\text{out}}}\left(\frac{T_{\text{oc}}}{T_{\text{rt}}}\right)^2 n_{\text{sp}} f^{-2} \end{aligned} \tag{B.6}$$

Equation (B.6) can be used to model shot-noise limited phase noise of a passive cavity, with $P_{\text{out}}$ being the optical power in the PDH loop.

# Appendix C

# Phase Locked Loop Analysis Using MATLAB Toolboxes

MATLAB offers a number of toolboxes suitable for phase locked loop analysis. In developing the phase noise model in Chapter 4, the Control System Toolbox and the Robust Control Toolbox are used to model the single-input-single-output (SISO) loop and the multiple-input-multiple-output (MIMO) loop, respectively.

In SISO loops, each component is given by `tf(num,den)`, where `num` and `den` are the numerator and denominator of the transfer function in Laplace space. The loop gain and bandwidth are optimized by the interactive `sisotool` command, which finds the optimal loop compensator parameters with given criteria. In the case of the PDH loop, the criteria is specified as the minimum closed-loop bandwidth and phase margin (60°). Then the loop compensator is updated with the optimal proportional and integral gains. Finally, the components are linked together using the `feedback(sys1,sys2)` command, in which `sys1` is the multiplication of the forward-path components and `sys2` represents the backward path. And `freqresp(sys)` is a convenient command to retrieve magnitude and phase response of the close-loop transfer function `sys`.

Although the Control System Toolbox is capable of modeling MIMO loops, the Robust Control Toolbox offers additional functionality with more flexibility. In particular, it offers the `looptune` command, which tunes fixed-structure feedback loop with customized options. Loop components are specified with `ltiblock.pid` and `ltiblock.gain` for proportional-integral-derivative (PID) controllers and gain blocks, respectively. Loop instability `gam` is given as a single value which includes the loop bandwidth, performance and robustness. If `gam` is larger than unity, the loop is considered unstable. The default gain margin is 7.6 dB, and the default phase margin is 45°. The other options, specified with the `looptuneOptions` command, used in the simulation are as follows. `RandomStart` is set to be 4, which means `looptune` performs 4 additional optimizations starting from randomly generated parameters. `UseParallel` is set to be `true`, so that a parallel pool is enabled to run concurrent processes. `TargetGain` is set to be 0.7, which forces the optimization to continue until the loop instability `gam` is close to 0.7. Transfer functions of the external noise sources are accessed with the `loopswitch` and `getIOTransfer` commands.

# Bibliography

[1] IEEE, "IEEE standard definitions of physical quantities for fundamental frequency and time metrology-random instabilities," in *IEEE Standards Coordinating Committee 27* vol. IEEE STD 1139-2008, ed, 2009, pp. c1-35.

[2] M. I. Skolnik, *Introduction to Radar Systems*: Tata McGraw Hill, 2003.

[3] J. R. Vig, "Quartz Crystal Resonators and Oscillators for Frequency Control and Timing Applications-A Tutorial," in *IEEE Ultrasonics, Ferroelectrics, and Freqeuncy Control Society*, 2013, pp. 4-82.

[4] E. N. Ivanov and M. E. Tobar, "Low phase-noise sapphire crystal microwave oscillators: current status," *IEEE Transactions on Ultrasonics Ferroelectrics and Frequency Control,* vol. 56, pp. 263-269, 2009.

[5] S. Grop, P. Y. Bourgeois, R. Boudot, Y. Kersale, E. Rubiola, and V. Giordano, "10 GHz cryocooled sapphire oscillator with extremely low phase noise," *Electronics Letters,* vol. 46, pp. 420-422, 2010.

[6] T. M. Fortier, M. S. Kirchner, F. Quinlan, J. Taylor, J. C. Bergquist, T. Rosenband, *et al.*, "Generation of ultrastable microwaves via optical frequency division," *Nature Photonics,* vol. 5, pp. 425-429, 2011.

[7] D. B. Leeson, "A simple model of feedback oscillator noise spectrum," *Proceedings of the IEEE,* vol. 54, pp. 329-330, 1966.

[8] V. B. Braginsky, V. S. Ilchenko, and K. S. Bagdassarov, "Experimental observation of fundamental microwave absorption in high-quality dielectric crystals," *Physics Letters A,* vol. 120, pp. 300-305, 1987.

[9] D. L. Creedon, Y. Reshitnyk, W. Farr, J. M. Martinis, T. L. Duty, and M. E. Tobar, "High Q-factor sapphire whispering gallery mode microwave resonator at single photon energies and millikelvin temperatures," *Applied Physics Letters,* vol. 98, p. 222903, 2011.

[10] K. Numata, A. Kemery, and J. Camp, "Thermal-noise limit in the frequency stabilization of lasers with rigid cavities," *Physical Review Letters,* vol. 93, pp. 250602-250602, 2004.

[11] T. Kessler, C. Hagemann, C. Grebing, T. Legero, U. Sterr, F. Riehle, *et al.*, "A sub-40-mHz-linewidth laser based on a silicon single-crystal optical cavity," *Nature Photonics,* vol. 6, pp. 687-692, 2012.

[12] Ü. Demirbaş, "Low-cost, highly efficient, and tunable ultrafast laser technology based on directly diode-pumped Cr:Colquiriites," Ph.D., Electrical Engineering and Computer Science, Massachusetts Institute of Technology, 2010.

[13] S. Uemura and K. Torizuka, "Generation of 10 fs pulses from a diode-pumped Kerr-lens mode-locked Cr : LiSAF laser," *Japanese Journal of Applied Physics Part 1-Regular Papers Short Notes & Review Papers,* vol. 39, pp. 3472-3473, 2000.

[14] Ü. Demirbaş, A. Sennaroğlu, F. X. Kärtner, and J. G. Fujimoto, "Highly efficient, low-cost femtosecond $Cr^{3+}$:LiCAF laser pumped by single-mode diodes," *Optics Letters,* vol. 33, pp. 590-592, 2008.

[15] Ü. Demirbaş, D. Li, J. R. Birge, A. Sennaroğlu, G. S. Petrich, L. A. Kolodziejski, *et al.*, "Low-cost, single-mode diode-pumped Cr:Colquiriite lasers," *Optics Express,* vol. 17, pp. 14374-14388, 2009.

[16] S. Tsuda, W. H. Knox, S. T. Cundiff, W. Y. Jan, and J. E. Cunningham, "Mode-locking ultrafast solid-state lasers with saturable Bragg reflectors," *IEEE Journal of Selected Topics in Quantum Electronics,* vol. 2, pp. 454-464, 1996.

[17] U. Keller, K. J. Weingarten, F. X. Kärtner, D. Kopf, B. Braun, I. D. Jung, *et al.*, "Semiconductor saturable absorber mirrors (SESAM's) for femtosecond to nanosecond pulse generation in solid-state lasers," *IEEE Journal of Selected Topics in Quantum Electronics,* vol. 2, pp. 435-453, Sep 1996.

[18] Ü. Demirbaş, A. Sennaroğlu, A. Benedick, A. Siddiqui, F. X. Kärtner, and J. G. Fujimoto, "Diode-pumped, high-average-power femtosecond $Cr^{3+}$:LiCAF laser," *Optics Letters,* vol. 32, pp. 3309-3311, 2007.

[19] Ü. Demirbaş, A. Sennaroğlu, F. X. Kärtner, and J. G. Fujimoto, "Generation of 15 nJ pulses from a highly efficient, low-cost multipass-cavity $Cr^{3+}$:LiCAF laser," *Optics Letters,* vol. 34, pp. 497-499, 2009.

[20] Ü. Demirbaş, K.-H. Hong, J. G. Fujimoto, A. Sennaroğlu, and F. X. Kärtner, "Low-cost cavity-dumped femtosecond Cr:LiSAF laser producing >100 nJ pulses," *Optics Letters,* vol. 35, pp. 607-609, 2010.

[21] Ü. Demirbaş, G. S. Petrich, S. Nabanja, J. R. Birge, L. A. Kolodziejski, F. X. Kärtner, *et al.*, "Widely-tunable femtosecond operation of Cr:LiSAF lasers using broadband saturable bragg reflectors," in *Conference on Lasers and Electro-Optics (CLEO) and Quantum Electronics and Laser Science Conference (QELS)*, 2010, p. CThI3.

[22] J. M. Hopkins, G. J. Valentine, B. Agate, A. J. Kemp, U. Keller, and W. Sibbett, "Highly compact and efficient femtosecond Cr:LiSAF lasers," *IEEE Journal of Quantum Electronics,* vol. 38, pp. 360-368, 2002.

[23] A. J. Kemp, B. Stormont, B. Agate, C. T. A. Brown, U. Keller, and W. Sibbett, "Gigahertz repetition-rate from directly diode-pumped femtosecond Cr:LiSAF laser," *Electronics Letters,* vol. 37, pp. 1457-1458, 2001.

[24] T. Udem, J. Reichert, R. Holzwarth, and T. W. Hänsch, "Accurate measurement of large optical frequency differences with a mode-locked laser," *Optics Letters,* vol. 24, pp. 881-883, 1999.

[25] R. Holzwarth, T. Udem, T. Hänsch, J. C. Knight, W. J. Wadsworth, P. S. J. Russell, *et al.*, "Optical frequency synthesizer for precision spectroscopy," *Physical Review Letters,* vol. 85, pp. 2264-2267, 2000.

[26] J. J. McFerran, L. Nenadovic, W. C. Swann, J. B. Schlager, and N. R. Newbury, "A passively mode-locked fiber laser at 1.54 μm with a fundamental repetition frequency reaching 2 GHz," *Optics Express,* vol. 15, p. 13155, 2007.

[27] N. R. Newbury and B. R. Washburn, "Theory of the frequency comb output from a femtosecond fiber laser," *IEEE Journal of Quantum Electronics,* vol. 41, pp. 1388-1402, 2005.

[28] V. Dolgovskiy, N. Bucalovic, P. Thomann, C. Schori, G. Di Domenico, and S. Schilt, "Cross-influence between the two servo loops of a fully stabilized Er:fiber optical

frequency comb," *Journal of the Optical Society of America B,* vol. 29, pp. 2944-2957, 2012.

[29] W. Zhang, M. Lours, M. Fischer, R. Holzwarth, G. Santarelli, and Y. Coq, "Characterizing a fiber-based frequency comb with electro-optic modulator," *IEEE Transactions on Ultrasonics Ferroelectrics and Frequency Control,* vol. 59, pp. 432-8, 2012.

[30] D. Li, Ü. Demirbaş, J. R. Birge, G. S. Petrich, L. A. Kolodziejski, A. Sennaroğlu, *et al.*, "Diode-pumped gigahertz repetition rate femtosecond Cr:LiSAF laser," in *Conference on Lasers and Electro-Optics (CLEO) and Quantum Electronics and Laser Science Conference (QELS)*, 2010, pp. 1-2.

[31] D. Li, Ü. Demirbaş, J. R. Birge, G. S. Petrich, L. A. Kolodziejski, A. Sennaroğlu, *et al.*, "Diode-pumped passively mode-locked GHz femtosecond Cr:LiSAF laser with kW peak power," *Optics Letters,* vol. 35, pp. 1446-1448, 2010.

[32] D. Li, A. J. Benedick, Ü. Demirbaş, A. Sennaroğlu, J. G. Fujimoto, and F. X. Kärtner, "Attosecond Timing Jitter Pulse Trains from Semiconductor Saturable Absorber Mode-locked Cr:LiSAF Lasers," in *Conference on Lasers and Electro-Optics (CLEO) and Quantum Electronics and Laser Science Conference (QELS)*, 2012, p. CTh4A.7.

[33] D. Li, Ü. Demirbaş, A. Benedick, A. Sennaroğlu, J. G. Fujimoto, and F. X. Kärtner, "Attosecond timing jitter pulse trains from semiconductor saturable absorber mode-locked Cr:LiSAF lasers," *Optics Express,* vol. 20, pp. 23422-23435, 2012.

[34] D. Li, M. Y. Peng, H.-W. Chen, J. Lim, M. R. Watts, and F. X. Kärtner, "Fiber-optic demonstration of optical frequency division for erbium silicon photonics integrated oscillator," in *Conference on Lasers and Electro-Optics (CLEO) and Quantum Electronics and Laser Science Conference (QELS)*, 2014, p. Submitted.

[35] M. T. Murphy, T. Udem, R. Holzwarth, A. Sizmann, L. Pasquini, C. Araujo-Hauck, *et al.*, "High-precision wavelength calibration of astronomical spectrographs with laser frequency combs," *Monthly Notices of the Royal Astronomical Society,* vol. 380, pp. 839-847, 2007.

[36] C.-H. Li, A. J. Benedick, P. Fendel, A. G. Glenday, F. X. Kärtner, D. F. Phillips, *et al.*, "A laser frequency comb that enables radial velocity measurements with a precision of 1 cm $s^{-1}$," *Nature,* vol. 452, pp. 610-612, 2008.

[37] A. Bartels, S. A. Diddams, C. W. Oates, G. Wilpers, J. C. Bergquist, W. H. Oskay, *et al.*, "Femtosecond-laser-based synthesis of ultrastable microwave signals from optical frequency references," *Optics Letters,* vol. 30, pp. 667-667, 2005.

[38] J. Millo, M. Abgrall, M. Lours, E. M. L. English, H. Jiang, J. Guéna, *et al.*, "Ultralow noise microwave generation with fiber-based optical frequency comb and application to atomic fountain clock," *Applied Physics Letters,* vol. 94, pp. 141105-141105, 2009.

[39] F. Quinlan, T. M. Fortier, M. S. Kirchner, J. A. Taylor, M. J. Thorpe, N. Lemke, *et al.*, "Ultralow phase noise microwave generation with an Er:fiber-based optical frequency divider," *Optics Letters,* vol. 36, pp. 3260-3260, 2011.

[40] J. Kim, M. J. Park, M. H. Perrott, and F. X. Kärtner, "Photonic subsampling analog-to-digital conversion of microwave signals at 40-GHz with higher than 7-ENOB resolution," *Optics Express,* vol. 16, pp. 16509-16515, 2008.

[41] A. Khilo, S. J. Spector, M. E. Grein, A. H. Nejadmalayeri, C. W. Holzwarth, M. Y. Sander, *et al.*, "Photonic ADC: overcoming the bottleneck of electronic jitter," *Optics Express,* vol. 20, pp. 4454-4469, 2012.

[42] A. Devor, S. Sakadzic, V. J. Srinivasan, M. A. Yaseen, K. Nizar, P. A. Saisan, *et al.*, "Frontiers in optical imaging of cerebral blood flow and metabolism," *Journal of Cerebral Blood Flow & Metabolism,* vol. 32, pp. 1259-1276, 2012.

[43] U. Keller, "Recent developments in compact ultrafast lasers," *Nature,* vol. 424, pp. 831-8, 2003.

[44] A. J. Benedick, G. Chang, J. R. Birge, L.-J. Chen, A. G. Glenday, C.-H. Li, *et al.*, "Visible wavelength astro-comb," *Optics Express,* vol. 18, pp. 19175-19184, 2010.

[45] S. A. Diddams, M. Kirchner, T. Fortier, D. Braje, A. M. Weiner, and L. Hollberg, "Improved signal-to-noise ratio of 10 GHz microwave signals generated with a mode-filtered femtosecond laser frequency comb," *Optics Express,* vol. 17, pp. 3331-3340, 2009.

[46] A. Haboucha, W. Zhang, T. Li, M. Lours, A. N. Luiten, Y. Le Coq, *et al.*, "Optical-fiber pulse rate multiplier for ultralow phase-noise signal generation," *Optics Letters,* vol. 36, pp. 3654-3654, 2011.

[47] M. Y. Sander, S. Frolov, J. Shmulovich, E. P. Ippen, and F. X. Kärtner, "10 GHz femtosecond pulse interleaver in planar waveguide technology," *Optics Express,* vol. 20, pp. 4102-4113, 2012.

[48] R. A. Probst, T. Steinmetz, T. Wilken, H. Hundertmark, S. P. Stark, G. K. L. Wong, *et al.*, "Nonlinear amplification of side-modes in frequency combs," *Optics Express,* vol. 21, pp. 11670-11687, 2013.

[49] G. Chang, C.-H. Li, D. F. Phillips, A. Szentgyorgyi, R. L. Walsworth, and F. X. Kärtner, "Optimization of filtering schemes for broadband astro-combs," *Optics Express,* vol. 20, pp. 24987-25013, 2012.

[50] F. Quinlan, F. N. Baynes, T. M. Fortier, Q. Zhou, A. Cross, J. C. Campbell, *et al.*, "Optical amplification and pulse interleaving for low noise photonic microwave generation," *arXiv:1312.1997 [physics.optics],* 2013.

[51] A. Bartels and H. Kurz, "Generation of a broadband continuum by a Ti:sapphire femtosecond oscillator with a 1-GHz repetition rate," *Optics Letters,* vol. 27, pp. 1839-1841, 2002.

[52] T. M. Fortier, A. Bartels, and S. A. Diddams, "Octave-spanning Ti:sapphire laser with a repetition rate >1 GHz for optical frequency measurements and comparisons," *Optics Letters,* vol. 31, pp. 1011-1013, 2006.

[53] A. Bartels, T. Dekorsy, and H. Kurz, "Femtosecond Ti:sapphire ring laser with a 2-GHz repetition rate and its application in time-resolved spectroscopy," *Optics Letters,* vol. 24, pp. 996-998, 1999.

[54] G. T. Nogueira, B. Xu, Y. Coello, M. Dantus, and F. C. Cruz, "Broadband 2.12 GHz Ti:sapphire laser compressed to 5.9 femtoseconds using MIIPS," *Optics Express,* vol. 16, pp. 10033-10038, 2008.

[55] A. Bartels, R. Gebs, M. S. Kirchner, and S. A. Diddams, "Spectrally resolved optical frequency comb from a self-referenced 5 GHz femtosecond laser," *Optics Letters,* vol. 32, pp. 2553-2555, 2007.

[56] A. Bartels, D. Heinecke, and S. A. Diddams, "10-Ghz self-referenced optical frequency comb," *Science,* vol. 326, p. 681, 2009.

[57] A. Bartels, D. Heinecke, and S. A. Diddams, "Passively mode-locked 10 GHz femtosecond Ti:sapphire laser," *Optics Letters,* vol. 33, pp. 1905-1907, 2008.

[58] L. Krainer, R. Paschotta, S. Lecomte, M. Moser, K. J. Weingarten, and U. Keller, "Compact Nd:YVO4 lasers with pulse repetition rates up to 160 GHz," *IEEE Journal of Quantum Electronics,* vol. 38, pp. 1331-1338, 2002.

[59] A. E. Oehler, T. Südmeyer, K. J. Weingarten, and U. Keller, "100 GHz passively mode-locked Er:Yb:glass laser at 1.5 um with 1.6-ps pulses," *Optics Express,* vol. 16, pp. 21930-21935, 2008.

[60] S. A. Payne, L. L. Chase, L. K. Smith, W. L. Kway, and H. W. Newkirk, "Laser performance of $LiSrAlF_6$-$Cr^{3+}$," *Journal of Applied Physics,* vol. 66, pp. 1051-1056, 1989.

[61] P. Adamiec, B. Sumpf, I. Rüdiger, J. Fricke, K.-H. Hasler, P. Ressel, *et al.*, "Tapered lasers emitting at 650 nm with 1 W output power with nearly diffraction-limited beam quality," *Optics Letters,* vol. 34, pp. 2456-2458, 2009.

[62] H. Kogelnik and T. Li, "Laser Beams and Resonators," *Applied Optics,* vol. 5, pp. 1550-1567, 1966.

[63] C. Hooninger, R. Paschotta, F. Morier-Genoud, M. Moser, and U. Keller, "Q-switching stability limits of continuous-wave passive mode locking," *Journal of the Optical Society of America B,* vol. 16, pp. 46-56, 1999.

[64] S. Tsuda, W. H. Knox, E. A. de Souza, W. Y. Jan, and J. E. Cunningham, "Low-loss intracavity AlAs/AlGaAs saturable Bragg reflector for femtosecond mode locking in solid-state lasers," *Optics Letters,* vol. 20, pp. 1406-1408, 1995.

[65] J. R. Birge and F. X. Kärtner, "Efficient analytic computation of dispersion from multilayer structures," *Applied Optics,* vol. 45, pp. 1478-1483, 2006.

[66] J. R. Birge and F. X. Kärtner, "Efficient optimization of multilayer coatings for ultrafast optics using analytic gradients of dispersion," *Applied Optics,* vol. 46, pp. 2656-2662, 2007.

[67] S. N. Tandon, J. T. Gopinath, H. M. Shen, G. S. Petrich, L. A. Kolodziejski, F. X. Kärtner, *et al.*, "Large-area broadband saturable Bragg reflectors by use of oxidized AlAs," *Optics Letters,* vol. 29, pp. 2551-2553, 2004.

[68] J. Kim and F. X. Kärtner, "Attosecond-precision ultrafast photonics," *Laser & Photonics Reviews,* vol. 4, pp. 432-456, 2010.

[69] H. A. Haus and A. Mecozzi, "Noise of mode-locked lasers," *IEEE Journal of Quantum Electronics,* vol. 29, pp. 983-996, 1993.

[70] R. Paschotta, "Noise of mode-locked lasers (Part I): numerical model," *Applied Physics B: Lasers and Optics,* vol. 79, pp. 153-162, 2004.

[71] R. Paschotta, "Noise of mode-locked lasers (Part II): timing jitter and other fluctuations," *Applied Physics B: Lasers and Optics,* vol. 79, pp. 163-173, 2004.

[72] T. R. Schibli, J. Kim, O. Kuzucu, J. T. Gopinath, S. N. Tandon, G. S. Petrich, *et al.*, "Attosecond active synchronization of passively mode-locked lasers by balanced cross correlation," *Optics Letters,* vol. 28, pp. 947-949, 2003.

[73] J. A. Cox, A. H. Nejadmalayeri, J. Kim, and F. X. Kärtner, "Complete characterization of quantum-limited timing jitter in passively mode-locked fiber lasers," *Optics Letters,* vol. 35, pp. 3522-3524, 2010.

[74] Y. Song, C. Kim, K. Jung, H. Kim, and J. Kim, "Timing jitter optimization of mode-locked Yb-fiber lasers toward the attosecond regime," *Optics Express,* vol. 19, pp. 14518-14525, 2011.

[75] Ü. Demirbaş, A. Benedick, A. Sennaroğlu, D. Li, J. Kim, J. G. Fujimoto, *et al.*, "Attosecond resolution timing jitter characterization of diode pumped femtosecond Cr:LiSAF lasers," in *Conference on Lasers and Electro-Optics (CLEO) and Quantum Electronics and Laser Science Conference (QELS)*, 2010, p. CTuDD6.

[76] A. J. Benedick, J. G. Fujimoto, and F. X. Kärtner, "Optical flywheels with attosecond jitter," *Nature Photonics,* vol. 6, pp. 97-100, 2012.

[77] T. K. Kim, Y. Song, K. Jung, C. Kim, H. Kim, C. H. Nam, *et al.*, "Sub-100-as timing jitter optical pulse trains from mode-locked Er-fiber lasers," *Optics Letters,* vol. 36, pp. 4443-4445, 2011.

[78] Y. Song, K. Jung, and J. Kim, "Impact of pulse dynamics on timing jitter in mode-locked fiber lasers," *Optics Letters,* vol. 36, pp. 1761-1763, 2011.

[79] R. Paschotta, "Timing jitter and phase noise of mode-locked fiber lasers," *Optics Express,* vol. 18, pp. 5041-5054, 2010.

[80] F. X. Kärtner, I. D. Jung, and U. Keller, "Soliton mode-locking with saturable absorbers," *IEEE Journal of Selected Topics in Quantum Electronics,* vol. 2, pp. 540-556, 1996.

[81] J. P. Gordon and H. A. Haus, "Random walk of coherently amplified solitons in optical fiber transmission," *Optics Letters,* vol. 11, pp. 665-667, 1986.

[82] Ü. Demirbaş, G. S. Petrich, D. Li, A. Sennaroğlu, L. A. Kolodziejski, F. X. Kärtner, *et al.*, "Femtosecond tuning of Cr:colquiriite lasers with AlGaAs-based saturable Bragg reflectors," *Journal of the Optical Society of America B-Optical Physics,* vol. 28, pp. 986-993, 2011.

[83] A. L. Lance, W. D. Seal, and F. Labaar, "Phase Nosie and AM Noise Measurements in the Frequency Domain," in *Infrared and Millimeter Waves.* vol. 11, K. J. Button, Ed., ed, 1984, pp. 239-289.

[84] "SNLO nonlinear optics code available from A.V.Smith, AS-Photonics, Albuquerque, NM."

[85] A. J. Benedick, "Applications and noise properties of high repetition rate TiSapphire frequency combs," Ph.D., Electrical Engineering and Computer Science, Massachusetts Institute of Technology, 2011.

[86] E. N. Ivanov, J. J. McFerran, S. A. Diddams, and L. Hollberg, "Noise properties of microwave signals synthesized with femtosecond lasers," *Ultrasonics, Ferroelectrics and Frequency Control, IEEE Transactions on,* vol. 54, pp. 736-745, 2007.

[87] F. DeMartini, C. H. Townes, T. K. Gustafson, and P. L. Kelley, "Self-steepening of light pulses," *Physical Review,* vol. 164, pp. 312-323, 1967.

[88] H. A. Haus and E. P. Ippen, "Group velocity of solitons," *Optics Letters,* vol. 26, pp. 1654-1656, 2001.

[89] R. P. Scott, C. Langrock, and B. H. Kolner, "High-dynamic-range laser amplitude and phase noise measurement techniques," *IEEE Jouranl of Selected Topics in Quantum Electronics,* vol. 7, pp. 641-655, 2001.

[90] K. Petermann, *Laser diode modulation and noise.* Norwell, MA: Kluwer Academic Publishers, 1988.

[91] L. Matos, O. D. Mücke, J. Chen, and F. X. Kärtner, "Carrier-envelope phase dynamics and noise analysis in octave-spanning Ti:sapphire lasers," *Optics Express,* vol. 14, pp. 2497-2511, 2006.

[92] W. A. Zortman, D. C. Trotter, and M. R. Watts, "Silicon photonics manufacturing," *Optics Express,* vol. 18, pp. 23598-607, 2010.

[93] M. Hochberg and T. Baehr-Jones, "Towards fabless silicon photonics," *Nature Photonics,* vol. 4, pp. 492-494, 2010.

[94] D. Marpaung, C. Roeloffzen, R. Heideman, A. Leinse, S. Sales, and J. Capmany, "Integrated microwave photonics," *Laser & Photonics Reviews,* vol. 7, pp. 506-538, 2013.

[95] J. Capmany and D. Novak, "Microwave photonics combines two worlds," *Nature Photonics,* vol. 1, pp. 319-330, 2007.

[96] J. A. Burns, B. F. Aull, C. K. Chen, C. L. Keast, J. M. Knecht, V. Suntharalingam, *et al.*, "A wafer-scale 3-D circuit integration technology," *IEEE Transactions on Electron Devices,* vol. 53, pp. 2507-2516, 2006.

[97] M.-C. Tien, J. F. Bauters, M. J. R. Heck, D. T. Spencer, D. J. Blumenthal, and J. E. Bowers, "Ultra-high quality factor planar $Si_3N_4$ ring resonators on Si substrates," *Optics Express,* vol. 19, pp. 13551-13556, 2011.

[98] Q. Li, A. A. Eftekhar, M. Sodagar, Z. Xia, A. H. Atabaki, and A. Adibi, "Vertical integration of high-Q silicon nitride microresonators into silicon-on-insulator platform," *Optics Express,* vol. 21, pp. 18236-18248, 2013.

[99] K. Luke, A. Dutt, C. B. Poitras, and M. Lipson, "Overcoming $Si_3N_4$ film stress limitations for high quality factor ring resonators," *Optics Express,* vol. 21, pp. 22829-22833, 2013.

[100] P. Alipour, A. H. Atabaki, A. A. Eftekhar, and A. Adibi, "Athermal performance in titania-clad microring resonators on SOI," in *Integrated Photonics Research, Silicon and Nanophotonics and Photonics in Switching*, Monterey, California, 2010, p. IMC6.

[101] F. Qiu, F. Yu, A. M. Spring, and S. Yokoyama, "Athermal silicon nitride ring resonator by photobleaching of Disperse Red 1-doped poly(methyl methacrylate) polymer," *Optics Letters,* vol. 37, pp. 4086-4088, 2012.

[102] E. S. Hosseini, J. Bradley, J. Sun, G. Leake, T. N. Adam, D. D. Coolbaugh, *et al.*, "CMOS compatible high power erbium doped distributed feedback lasers," in *Advanced Photonics*, 2013, p. IM2A.4.

[103] Purnawirman, J. Sun, T. N. Adam, G. Leake, D. Coolbaugh, J. D. B. Bradley, *et al.*, "C- and L-band erbium-doped waveguide lasers with wafer-scale silicon nitride cavities," *Optics Letters,* vol. 38, p. 1760, 2013.

[104] M. Belt, T. Huffman, M. L. Davenport, W. Li, J. S. Barton, and D. J. Blumenthal, "Arrayed narrow linewidth erbium-doped waveguide-distributed feedback lasers on an ultra-low-loss silicon-nitride platform," *Optics Letters,* vol. 38, pp. 4825-4828, 2013.

[105] A. H. Nejadmalayeri, H. Byun, J. Kim, D. C. Trotter, C. DeRose, A. L. Lentine, *et al.*, "Integrated optical phase locked loop," in *Conference on Lasers and Electro-Optics/Quantum Electronics and Laser Science and Photonic Applications Systems Technologies*, 2011, p. CThY7.

[106] M. Lu, H. Park, E. Bloch, A. Sivananthan, A. Bhardwaj, Z. Griffith, *et al.*, "Highly integrated optical heterodyne phase-locked loop with phase/frequency detection," *Optics Express,* vol. 20, p. 9736, 2012.

[107] D. T. H. Tan, K. Ikeda, P. C. Sun, and Y. Fainman, "Group velocity dispersion and self phase modulation in silicon nitride waveguides," *Applied Physics Letters,* vol. 96, p. 061101, 2010.

[108] M. R. Watts, W. A. Zortman, D. C. Trotter, R. W. Young, and A. L. Lentine, "Low-voltage, compact, depletion-mode, silicon Mach–Zehnder modulator," *IEEE Journal of Selected Topics in Quantum Electronics,* vol. 16, pp. 159-164, 2010.

[109] F. Gan, T. Barwicz, M. A. Popovic, M. S. Dahlem, C. W. Holzwarth, P. T. Rakich, *et al.*, "Maximizing the thermo-optic tuning range of silicon photonic structures," in *Photonics in Switching*, San Francisco, CA, 2007, pp. 67-68.

[110] M. R. Watts, W. A. Zortman, D. C. Trotter, G. N. Nielson, D. L. Luck, and R. W. Young, "Adiabatic Resonant Microrings (ARMs) with directly integrated thermal microphotonics," in *Conference on Lasers and Electro-Optics/Quantum Electronics and Laser Science and Photonic Applications Systems Technologies*, 2009, pp. 1-2.

[111] D. Ahn, C.-Y. Hong, J. Liu, W. Giziewicz, M. Beals, L. C. Kimerling, *et al.*, "High performance, waveguide integrated Ge photodetectors," *Optics Express,* vol. 15, p. 3916, 2007.

[112] C. T. DeRose, D. C. Trotter, W. A. Zortman, A. L. Starbuck, M. Fisher, M. R. Watts, *et al.*, "Ultra compact 45 GHz CMOS compatible Germanium waveguide photodiode with low dark current.," *Optics Express,* vol. 19, pp. 24897-904, 2011.

[113] A. Ramaswamy, M. Piels, N. Nunoya, T. Yin, and J. E. Bowers, "High power silicon-germanium photodiodes for microwave photonic applications," *IEEE Transactions on Microwave Theory and Techniques,* vol. 58, pp. 3336-3343, 2010.

[114] C. L. Chen, D.-R. Yost, J. M. Knecht, D. C. Chapman, D. C. Oakley, L. J. Mahoney, *et al.*, "Wafer-scale 3D integration of InGaAs image sensors with Si readout circuits," in *International Conference on 3D System Integration*, 2009, pp. 1-4.

[115] J. Sun, E. Timurdogan, A. Yaacobi, E. S. Hosseini, and M. R. Watts, "Large-scale nanophotonic phased array," *Nature,* vol. 493, pp. 195-199, 2013.

[116] D. J. Jones, S. A. Diddams, J. K. Ranka, A. Stentz, R. S. Windeler, J. L. Hall, *et al.*, "Carrier-envelope phase control of femtosecond mode-locked lasers and direct optical frequency synthesis," *Science,* vol. 288, pp. 635-639, 2000.

[117] J. Leuthold, C. Koos, and W. Freude, "Nonlinear silicon photonics," *Nature Photonics,* vol. 4, pp. 535-544, 2010.

[118] M. Cazzanelli, F. Bianco, E. Borga, G. Pucker, M. Ghulinyan, E. Degoli, *et al.*, "Second-harmonic generation in silicon waveguides strained by silicon nitride," *Nature Materials,* vol. 11, pp. 148-54, 2012.

[119] H. Inaba, T. Ikegami, H. Feng-Lei, A. Onae, Y. Koga, T. R. Schibli, *et al.*, "Phase locking of a continuous-wave optical parametric oscillator to an optical frequency comb for optical frequency synthesis," *IEEE Journal of Quantum Electronics,* vol. 40, pp. 929-936, 2004.

[120] T. R. Schibli, K. Minoshima, F. L. Hong, H. Inaba, Y. Bitou, A. Onae, *et al.*, "Phase-locked widely tunable optical single-frequency generator based on a femtosecond comb," *Optics Letters,* vol. 30, pp. 2323-2325, 2005.

[121] P. W. Juodawlkis, J. J. Plant, R. K. Huang, L. J. Missaggia, and J. P. Donnelly, "High-power 1.5-um InGaAsP-InP slab-coupled optical waveguide amplifier," *IEEE Photonics Technology Letters,* vol. 17, pp. 279-281, 2005.

[122] P. W. Juodawlkis, W. Loh, F. J. O'Donnell, M. A. Brattain, and J. J. Plant, "High-power ultralow-noise semiconductor external cavity lasers based on low-confinement optical waveguide gain media," in *Novel In-Plane Semiconductor Lasers IX*, San Francisco, California, 2010, p. 76160X.

[123] R. W. P. Drever, J. L. Hall, F. V. Kowalski, J. Hough, G. M. Ford, A. J. Munley, *et al.*, "Laser phase and frequency stabilization using an optical resonator," *Applied Physics B Photophysics and Laser Chemistry,* vol. 31, pp. 97-105, 1983.

[124] N. J. Doran and D. Wood, "Nonlinear-optical loop mirror," *Optics Letters,* vol. 13, pp. 56-58, 1988.

[125] Y. Kokubun, N. Funato, and M. Takizawa, "Athermal waveguides for temperature-independent lightwave devices," *IEEE Photonics Technology Letters,* vol. 5, pp. 1297-1300, 1993.

[126] E. D. Black, "An introduction to Pound-Drever-Hall laser frequency stabilization," *American Journal of Physics,* vol. 69, pp. 79-87, 2001.

[127] E. H. Bernhardi, H. A. G. M. van Wolferen, L. Agazzi, M. R. H. Khan, C. G. H. Roeloffzen, K. Wörhoff, *et al.*, "Ultra-narrow-linewidth, single-frequency distributed feedback waveguide laser in $Al_2O_3:Er^{3+}$ on silicon," *Optics Letters,* vol. 35, pp. 2394-2396, 2010.

[128] M. Prevedelli, T. Freegarde, and T. W. Hänsch, "Phase locking of grating-tuned diode lasers," *Applied Physics B,* vol. 60, pp. S241-S248, 1995.

[129] S. Namiki and H. A. Haus, "Noise of the stretched pulse fiber laser. 1. Theory," *IEEE Journal of Quantum Electronics,* vol. 33, pp. 649-659, 1997.

[130] M. Norling, A. Vorobiev, H. Jacobsson, and S. Gevorgian, "A low-noise K-band VCO based on room-temperature ferroelectric varactors," *IEEE Transactions on Microwave Theory and Techniques,* vol. 55, pp. 361-369, 2007.

[131] Y. Shevy, D. Shevy, R. Lee, and D. Provenzano, "Slow light laser oscillator," in *Conference on Optical Fiber Communication (OFC), collocated National Fiber Optic Engineers(NFOEC)*, 2010, pp. 1-3.

[132] F. J. Grawert, F. Ö. Ilday, D. F. Kielpinski, J. T. Gopinath, G. S. Petrich, L. A. Kolodziejski, *et al.*, "Automatic feedback control of an Er-doped fiber laser with an intracavity loss modulator," *Optics Letters,* vol. 30, pp. 1066-1068, 2005.

[133] B. Sumpf, P. Adamiec, M. Zorn, H. Wenzel, and G. Erbert, "Nearly diffraction-limited tapered lasers at 675 nm with 1-W output power and conversion efficiencies above 30%," *IEEE Photonics Technology Letters,* vol. 23, pp. 266-268, 2011.

[134] X. Ma, L. Liu, and J. Tang, "Timing jitter measurement of transmitted laser pulse relative to the reference using type II second harmonic generation in two nonlinear crystals," *Optics Express,* vol. 17, pp. 19102-19112, 2009.

[135] R. Paschotta, H. R. Telle, and U. Keller, "Noise of solid state lasers," in *Solid-State Lasers and Applications*, A. Sennaroğlu, Ed., ed: CRC Press, 2007, pp. 473-510.